Developing a Spectral Radiance Model to Enable Radiometric Analysis for HCPV

by

Oliver Menken

in partial fulfilment of the requirements for the degree of

Master of Science
in Electrical Engineering,
Electrical Power Engineering track, Solar Energy specialisation

at the Delft University of Technology,
Faculty of Electrical Engineering, Mathematics and Computer Science
to be defended publicly on Wednesday February 24, 2021 at 02:00 PM.

Student number:	4568729	
Project duration:	August 1, 2018 – February 1, 2021	
Thesis committee:	Prof. dr. ir. A.H.M. Smets,	TU Delft, supervisor
	Dr. ir. R. Santbergen,	TU Delft, supervisor
	Dr. ir. J. Dong,	TU Delft

TU Delft Delft University of Technology

CONTENTS

SUMMARY

The world is in a renewable energy transition, and accelerating it requires solar energy to assume an even more competitive position. The subfield of Concentrator Photovoltaics (CPV) employs optical elements such as mirrors to focus solar flux to a small target area with a PV receiver, making more efficient yet expensive cells appealing. Additionally, the more intense irradiance due to concentration inherently improves energy conversion efficiency. CPV therefore boasts significantly higher energy conversion efficiency compared to conventional photovoltaic technologies, and could potentially have a role to play in the transition. The viability of CPV hinges upon whether the extra incurred costs can be justified, and it is understood in the industry that innovative system design is an absolute requirement.

CPV system designers are immediately presented with a significant problem, which is that there no standardised workhorse model to accurately evaluate CPV topologies. The spectral irradiance standards - the backbone of representative photovoltaic system analysis - could be used, but lose in validity the higher the concentration. The Sun is not a point source, and neither does it appear as a uniform disk. A different source model - the so-called sunshape - is used in the related field of Concentrated Solar Power (CSP), which also utilises concentrating optics but relies on thermal energy generation instead of the photovoltaic effect. The sunshape considers - without considering spectral information - the distribution of intensity over the extended source that is the Sun, because even these small angles matter for a concentrating application. It follows that CPV system analysis requires a spectral radiance model of the Sun that contains both spectral and directional information.

Simply combining the sunshape and the spectral irradiance standards is the most straightforward solution, but in doing so the assumption is made that the spectral and directional distribution of solar flux are independent. Observations with solar telescopes from the field of astronomy demonstrate that the two are not independent. In this thesis, a model from the astronomical literature is combined with the spectral irradiance standards to establish the spectral sunshape, a spectral radiance model of the Sun. This spectral sunshape is compared to the spectral radiance profile resulting from simply combining the sunshape and spectral irradiance standards. Additionally, a model in this framework for the most relevant optical element - the heliostat, a tracking mirror - is introduced. The spectral sunshape is combined with the heliostat model to arrive at the so-called effective spectral sunshape, which in turn is a representation of the spectral radiance post-reflection. With the (effective) spectral sunshape, the field of CPV can hopefully work towards realising its potential.

ACKNOWLEDGEMENTS

First and foremost, I would like to thank prof. dr. ir. Arno Smets for his enthusiasm from the very moment I stepped into his office to discuss Concentrator Photovoltaics as a thesis proposal. I will also fondly remember his enthusiasm and exchange of ideas during our meetings, which were often like brainstorming sessions. Secondly, I also want to extend my gratitude to dr. ir. Rudi Santbergen for sharing his extensive material knowledge with me, and for his supervision that applied structure to the research project. Your guidance and keen interest were very important to me and this project.

I would also like to thank my parents Bernard and Emely for their unwavering support throughout my entire life thus far, of course including this research project. I am also indebted to my sister Loes, who I can relate to on almost every level and to whom I strive to remain an example. Finally, I would like to thank the many friends I have made over the years for being a crucial part of my life and for enduring my frequent ramblings about solar energy and the future.

1

INTRODUCTION

Fossil fuels' finite supply and environmental impact have resulted in a strong societal desire to shift towards a renewable energy economy. Increased public awareness - as well as the strategic importance of energy autonomy - have encouraged governments to commit political resources towards making this wish a reality, and currently the renewable energy transition is in full swing. It is extremely likely that photovoltaic (PV) energy conversion will play a prominent role in the future energy supply, because of its abundant potential to meet societal demand and because of the competitive price level of PV systems.

The theoretical potential is evident from a back-of-the-envelope calculation, detailed in Appendix A.1, which demonstrates that it takes only 110 minutes for an amount of solar radiation equal to the annual global energy consumption to arrive at the Earth's surface. In case of an average conversion rate of 20% from irradiation to useful energy, and an average 90% loss from the location of generation to the location of useful consumption, dedicating just 1.0% of the Earth's surface to energy generation would be necessary to meet the aggregate demand.

Secondly, solar energy is already economically competitive as an energy source. The conventional metric used to compare economical performance of electricity generating technologies is the Levelised Cost of Electricity (LCOE). It is defined as the sum of the net present value of total expenditures of a system divided by the net present value of total generated electricity. That is, for technology i,

$$LCOE_i := \frac{\sum_{t=1}^{T} (\beta_C)^t * C_{i,t}}{\sum_{t=1}^{T} (\beta_E)^t * E_{i,t}} \tag{1.1}$$

β_C and β_E respectively denote the appropriate discount factors for money and electricity. They reflect the time value of money and electricity, and typically assume a value of about 0.9 to 0.95 depending on the investment climate. $C_{i,t}$ denotes the total net cost of technology i in year t, and $E_{i,t}$ the electricity generated by technology i in year t. T

is the economical lifetime of the system. Figure 1.1 below shows the unsubsidised levelised costs of electricity for various technologies, according to financial advisory and asset management firm Lazard (2019):

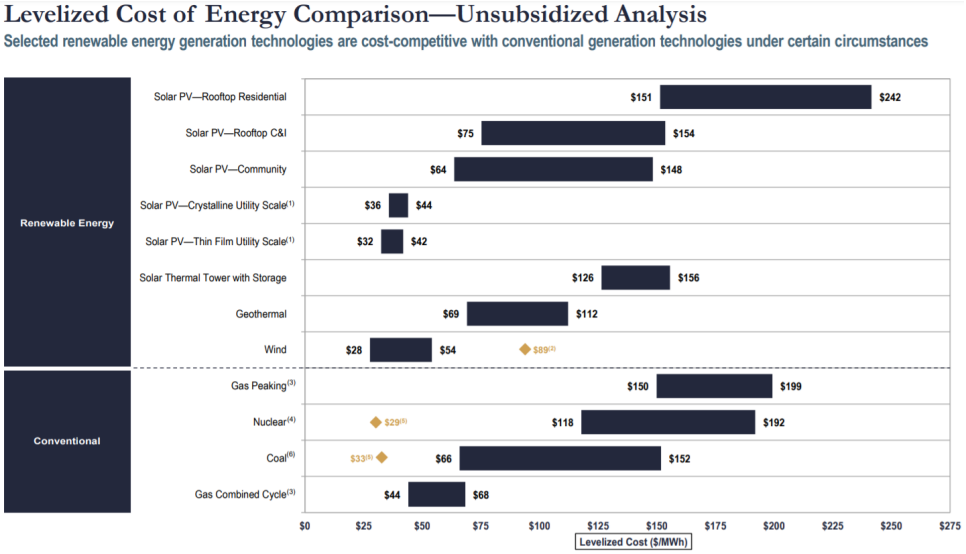

Figure 1.1: Low- and high-end LCOE estimates for various renewable and nonrenewable electricity sources, as estimated by Lazard [1].

It is apparent that utility-scale solar is already competing with the cheapest sources of electricity. However, an important caveat to the LCOE comparison is the intermittent nature of solar and wind energy, a fundamental drawback versus e.g. fossil fuel power plants that can deliver variable, controllable power. The golden diamond points represent the mean price points of intermittent sources including an electricity storage system (ESS), and therefore allow for a more appropriate comparison. In that case the gas combined cycle technology still reigns supreme, but utility-scale PV is close.

Besides the LCOE snapshot depicted in Figure 1.1, the rates of change are even more important to gauge economical performance in the near future. The historical means are presented in Figure 1.2. It is clearly visible that solar energy has been exhibiting an impressive LCOE decrease of 89% over ten years, or a compound annual growth rate (CAGR) of about -20%. Similar to wind energy, this rapid decrease is associated with increasing technological maturity and installed capacity. Since the installed solar energy capacity is expected to continue its increase, it is very likely that the downward trend will persist. Furthermore, it is estimated that ESS prices will fall by between 50% and 66% by 2030 [2].

The competitive present price level, the rapidly dwindling historical price levels, and the increasing cumulative deployment jointly suggest that utility-scale PV will be amongst the most competitive electricity sources in the near future. It should be stressed though that this future viability is conditional on continuing the downward trend in the LCOE.

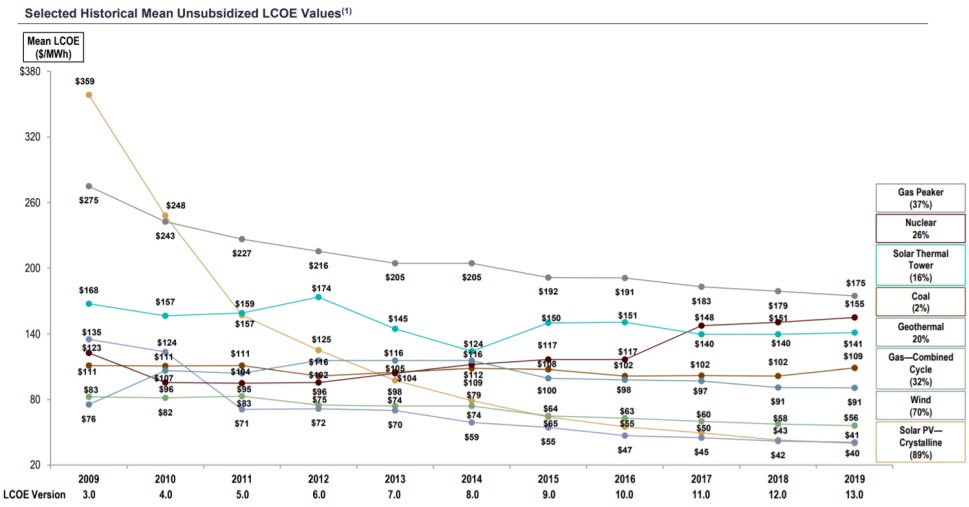

Figure 1.2: Evolution of the average LCOE of selected electricity generation technologies. [1]

From Equation (1.1) it follows that decreasing costs - the numerator - and increasing electricity output - the denominator - are both means to this end. In recent history the LCOE CAGR has been largely attributable to the numerator. The cumulative installed PV capacity grew from 70.4 GW in 2011 to 623.2 GW in 2019, and the accompanied economies of scale - translating into factors such as easier access to finance, mass manufacturing, and more efficient supply chains - have driven rapid cost decreases of PV. As for the denominator in the LCOE equation, the efficiency of average commercial Si modules increased from 12% to 17% over ten years [3], exhibiting a CAGR of 3.5%. Whilst sizeable, the figure pales in comparison to the exhibited LCOE CAGR of -20%. Furthermore - as the following Section 1.1 will elucidate - even the 3.5 % CAGR of efficiency will be difficult to maintain in the short term, and impossible to maintain in the long term.

1.1. PHOTOVOLTAIC ENERGY CONVERSION AND THE SHOCKLEY-QUEISSER LIMIT

This section evaluates the current PV industry from a technological point of view, and considers the fundamental efficiency limitations that arise due to inherent properties of PV cells and the nature of solar irradiance. Semiconductor physics and working principles underlying PV energy conversion are not covered in this section, but are well documented in the literature, e.g..

Currently, the global annual PV module supply is dominated by two crystalline silicon technologies: mono-Si and multi-Si [3]. The other category depicted in Figure 1.3, of thin-film technologies, is in turn dominated by three technologies: CdTe, CI(G)S and a-Si. As such, just three semiconductor materials - Si, CdTe and CI(G)S - constitute the backbone of the current PV landscape. All technologies are single-junction technologies,

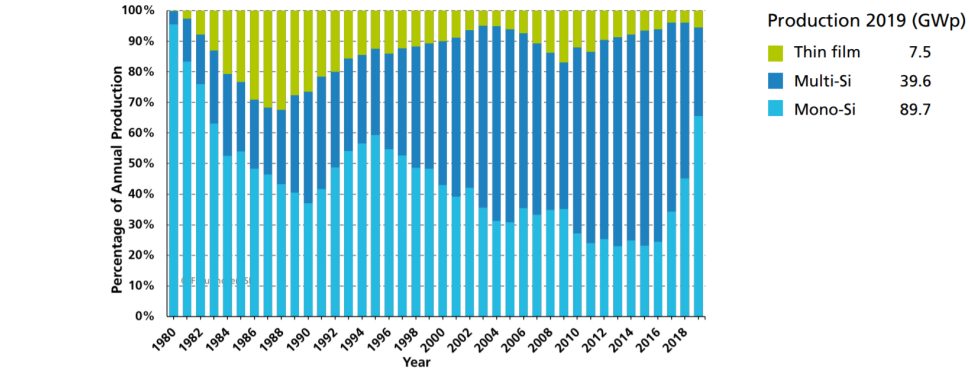

Figure 1.3: Global annual PV module production, subdivided into multi-Si, mono-Si and thin-film technologies. The category of thin film modules is almost entirely comprised of three technologies: CdTe, CI(G)S and a-Si [3].

which is an important factor in estimating the room for efficiency improvement.

1.1.1. THE SHOCKLEY-QUEISSER LIMIT

In 1960, William Shockley and Hans Queisser formulated the theoretical maximum efficiency limit for a single-junction PV cell [4]. The PV cell is devoid of practical imperfections, and only limited by fundamental physical phenomena. Examples of fundamental limitations are the principle of detailed balance, i.e. the creation of an electron-hole pair is possible if and only if the reverse process is also possible, and the inevitable blackbody radiation of the PV cell itself due to its temperature of 300 K. The eponymous Shockley-Queisser (SQ) limit follows from the following set of assumptions:

SQ1) There is a single junction, with a corresponding band gap energy level E_G.

SQ2) The incident spectral irradiance profile is the standard $AM1.5G$ spectrum.

SQ3) The PV cell operates at a temperature of 300 K

SQ4) Every incident photon possessing less energy than the junction's characteristic band gap will not be absorbed, i.e. if $E_{ph} < E_G$ no electron-hole pair can be generated.

SQ5) An incident photon excites a single electron-hole pair only if the photon is at least as energetic as the junction's characteristic band gap, i.e. if $E_{ph} \geq E_G$.

SQ6) If $E_{ph} > E_G$, the excited electron relaxes to E_G before collection such that an amount of $E_{th} = E_{ph} - E_G$ is converted into unusable thermal energy.

Assumptions SQ5) and SQ6) essentially imply that, if an electron-hole pair is excited, the collectable energy is equal to the band gap energy regardless of the exciting photon's original energy. It should be noted that assumption SQ2) here is an improvement upon the original assumption invoked by Shockley and Queisser, who considered the radiation profile emitted by a $6000K$ black body rather than the irradiance actually arriving at

Earth's surface. For terrestrial photovoltaic applications, the latter is obviously more relevant. The standard reference $AM1.5G$ (ASTM G-173-03 [5]) spectrum was established to model terrestrial irradiance, and the original Shockley-Queisser study simply predates its establishment.

The SQ limit as a function of a junction's band gap energy E_G is depicted in Figure 1.4. The dependency on band gap energy follows not just because of the $AM1.5G$ spectrum, but also from assumptions SQ4), SQ5) and SQ6). Decreasing the band gap energy E_G implies that a larger share of the $AM1.5G$ photons will excite an electron-hole pair, yet every excited pair only delivers the smaller band gap energy E_G as a consequence of SQ6). Excess photon energy is lost in thermalisation, which thus increases as the band gap decreases. On the other hand, although increasing the band gap energy directly corresponds to an increased amount of collectable energy per electron-hole pair, less such pairs will be excited because a decreasing share of photons will be sufficiently energetic to bridge the band gap. A trade-off as a function of band gap arises, which is apparent in Figure 1.4. Since the band gap energy is fixed for any particular single-junction PV cell, energy will necessarily be lost either way.

Figure 1.4 clearly reveals how sizeable these loss mechanisms are. Even an idealised single-junction PV cell has an upper conversion efficiency bound of just 31.0% [6]. This SQ limit corresponds to a band gap energy of 1.34 eV. Figure 1.5 shows the Shockley-Queisser limit for spectral utilisation in the market-dominating case of Si, with a band gap of $E_G = 1.11\ eV$ corresponding to $1100nm$. Photons below the band gap energy (above $1100nm$) are not absorbed at all, whilst an increasing share of energy is lost due to thermalisation as the photon energy increases (and photon wavelength decreases accordingly. The Figure also shows that the conversion efficiency at the band gap is 100% under the idealised SQ limit assumptions.

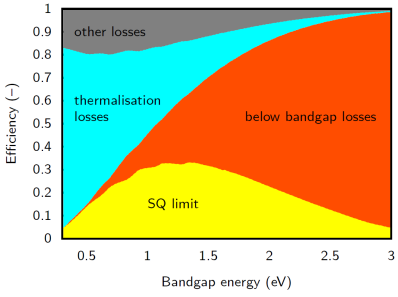

Figure 1.4: The Shockley-Queisser limit and fundamental loss mechanisms as a function of semiconductor band gap energy, reprinted from [7].

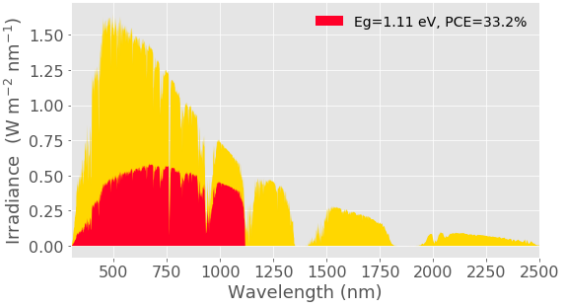

Figure 1.5: The SQ limit for crystalline silicon with $E_G = 1.11eV$ visualised in red, as a fraction of the total AM1.5G spectrum.

The crux is that single-junction PV cells have a fundamentally limited spectral response. Photons constituting the AM1.5G spectrum possess a range of energy values, yet any single-junction PV cell is incapable of converting efficiently across the entire range.

Owing to the poor spectral response, the upper efficiency bound is rather low. Even in case of ideal PV cells, the SQ efficiency limit stands at 33.2 %. For real PV cells, an even sharper upper efficiency bound holds. For indirect band gap materials - like Si - Auger recombination dominates radiative recombination, yet it is not even considered in the original SQ calculation. A recent study for the most prevalent material, crystalline Si, estimates its maximum theoretical efficiency to be 29.43% [8].

As for actually attained efficiencies, the current record Si cell boasts an efficiency of 26.7 ±0.5%, whilst the current record single-junction cell is a GaAs cell with an efficiency of 29.1 ±0.6% [9].The commercially successful PV cells from Figure 1.3, which are optimised with respect to value for money rather than efficiency, are about 17% efficient on average [3]. The record demonstrated Si efficiency is thus already within 10% of the theoretical upper bound, and average commercial cell efficiency is about 60% of the upper bound. Efficiency-wise, the room for improvement is fundamentally limited.

Photovoltaic efficiency exceeding the SQ limit is only possible by deftly circumventing the aforementioned SQ assumptions. Technologies both demonstrated and conceptual that attempt this feat are collectively referred to as third generation concepts [10]. The following section will discuss the one third generation concept which has thus far enabled photovoltaic energy conversion beyond the SQ limit: the multi-junction (MJ) approach.

1.2. THE MULTI-JUNCTION APPROACH

The MJ approach entails utilising multiple single-junction subcells to improve the spectral response. A general description of properties relevant for this thesis is provided, more elaborate documentation is present in e.g. [11] or [12]. Two different MJ strategies are explored in this section: the conventional multi-junction stack, and spectral beam splitting. Both approaches boast advantages yet also suffer from inherent limitations and challenges, which will all briefly be discussed.

1.2.1. TANDEM CELLS

The first MJ approach is that of the tandem cell - also known as the multijunction stacked cell - where multiple semiconductors with different band gaps are stacked on top of each other. The tandem cell constitutes the most technologically mature adaptation of the approach, and was the first successful third generation concept that demonstrably yielded an efficiency beyond the SQ limit. Photons with insufficient energy to interact with the uppermost semiconductor layer, i.e. photons with $E_{ph} < E_G$, tend to simply pass through without being absorbed or transmitted. These photons then enter a subcell with a lower band gap energy, in which the sufficiently energetic photons are absorbed and the insufficiently energetic are again largely transmitted to yet another different subcell. A tandem cell hereby essentially defers subsets of the spectrum to the subcells where conversion is the most efficient. A schematic of a typical triple-junction cell is depicted in Figure 1.10. Compared to a single-junction cell, both thermalisation and non-absorption losses are reduced; this improved spectral response is illustrated in Figure 1.6. The potential efficiency exceeds the SQ limit by simply violating assumption SQ1).

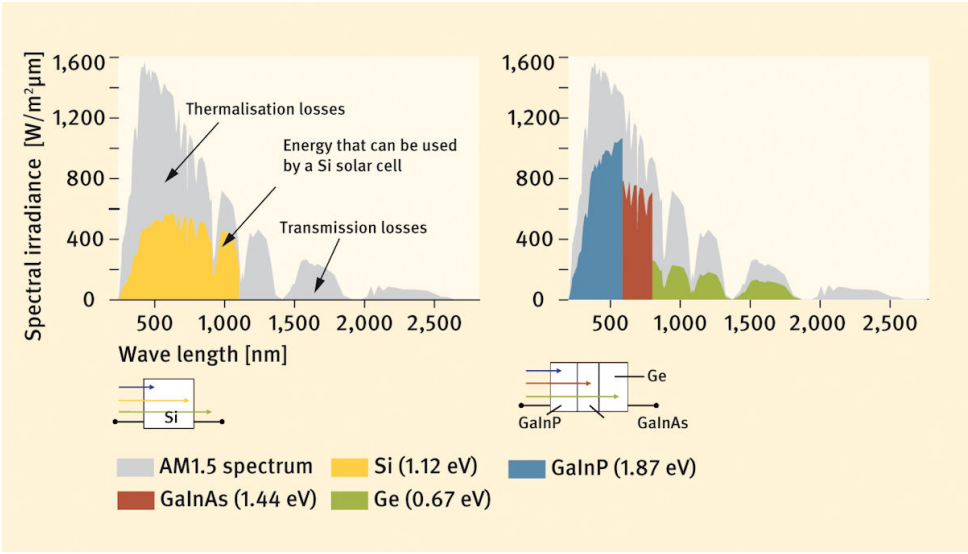

Figure 1.6: A spectral response comparison under the AM1.5G spectrum of a practical Si cell (left), versus a triple-junction GaInP-GaInAs-Ge cell (right). Note that photon energy is inversely proportional to wavelength: $E_{ph} = \frac{hc}{\lambda}$, where h and c respectively denote the Planck constant and the speed of light in vacuum. Reprinted from.

Additionally, tandem cells have more degrees of freedom in their design: it is not strictly necessary to select a material from the optimal band gap range from Figure 1.4, since many combinations can cover the spectrum adequately. Other properties relevant for photovoltaic conversion, such as external quantum efficiency (EQE), can be considered to solve an overall spectral utilisation problem. Tandem cells often employ III-V compound semiconductors because of their excellent photovoltaic properties, and because alloy ratios can be adjusted to tune subcells' band gaps. All in all, the potential overall efficiency is significantly higher compared to the single-junction case. Under a $6000K$ blackbody spectrum, the theoretical limit for an infinite number of junctions is 69.9% [6]. Triple- and quadruple-junctions already have a significantly higher ceiling (49.1% and 53.0% respectively) than the single-junction limit of 31.0% [6]. The current record efficiency under standard testing conditions stands at 38.8 ±1.2% for a quintuple-junction cell, and at 37.9 ±1.2% for a triple-junction cell [9].

Tandem cells also suffer from a number of drawbacks, which impose additional restrictions. Most drawbacks stem from the series-connection of the subcells in a stack [13]. Since a series-connected circuit is characterised by a single current, a tandem cell is current-limited by the subcell with the smallest current. Excess generated current is essentially lost, and it therefore follows that a delicate balance must be struck amongst the subcells such that each generates the same current when exposed to the solar spectral irradiance. This design goal is referred to as current matching. Current matching is achieved in practice by careful material selection based on the junction band gaps,

as well as by adapting the individual junctions' absorptivities through e.g. thickness. It is very important to note that a series-connected tandem cell design is fundamentally linked to the reference spectral radiance. A hypothetical current-matched tandem cell designed for the AM1.5G spectrum will generate the same current in every subcell only when actually exposed to the AM1.5G spectrum, or upscaled and downscaled versions thereof.

Unfortunately, the incident spectral irradiance for a fixed location on Earth is not even remotely constant over time in practice, due to a plethora of factors. The most important factor is the position of the Sun in the sky, with increased scattering resulting in redshifted light as the Sun is closer to the horizon. Atmospheric disturbances such as clouds also impact the real-time spectral irradiance profile incident on a location on Earth.

The incident spectral irradiance profile also varies significantly across locations, in the sense that the spectral content varies. Latitude is an important factor here because it directly determines the optical path length through the atmosphere of sunlight. The $AM1.5G$ standard spectrum is representative for mid latitudes, such as the contiguous U.S.A. Closer to the equator, the optical path length through the atmosphere is shorter on average, resulting in less absorption and a more redshifted incident spectral irradiance profile. Whilst it is of course possible to design a tandem cell for every location's specific annual spectral irradiance profile, this is not economically feasible or mass producible.

Although $AM1.5G$ is a tried and tested representative for the average irradiance at a typical location, it is never the case that a surface on Earth is only exposed to upscaled or downscaled $AM1.5G$ spectra during the day. Since a tandem cell itself is by nature inflexible in adapting its spectral response post-construction, it follows also that frequent current-limited operation is inevitable.

Another drawback is that reverse junctions arise at the interfaces if one would simply connect subcells with different band gaps in series directly. These reverse junctions would significantly limit the voltage, effectively wiping out the advantage of using multiple junctions in the first place. Tunnel junctions separating the subcells are implemented to prevent this voltage drop, but they also result in parasitic losses.

The tandem cell approach conveys material design constraints in addition to the current-matching requirement outlined above. Another requirement is that the photons with only sufficient energy for the lower junctions should pass through the upper layers unimpeded. In other words, the transmittance of photons through both the upper layers and tunnel junctions should be as close to unity as possible. This constitutes an additional material requirement for selecting the upper layer materials, and it is also important to note that this requirement interacts with the current matching problem described above.

Another design constraint worth noting stems from the conventional production method of tandem cells, epitaxy. Epitaxially grown tandem cells require subcells with the same lattice constant, in order to prevent defects between subcells that decrease performance. In recent times however, production methods for metamorphic (i.e. not

lattice-matched) tandem cells have been developed and demonstrated [14].

Due to the increased complexity, the scarcer materials, and above all the significantly smaller market size, tandem cells are orders of magnitude more expensive than the dominant single-junction technologies. Since the efficiencies attained by tandem cells are not orders of magnitude higher to offset this, it follows that tandem cells are not remotely competitive under terrestrial standard operating conditions. Despite this, tandem cells have found their niche in space applications, where the goals and constraints are different and the benefit of more generated electricity per unit area can outweigh the costs.

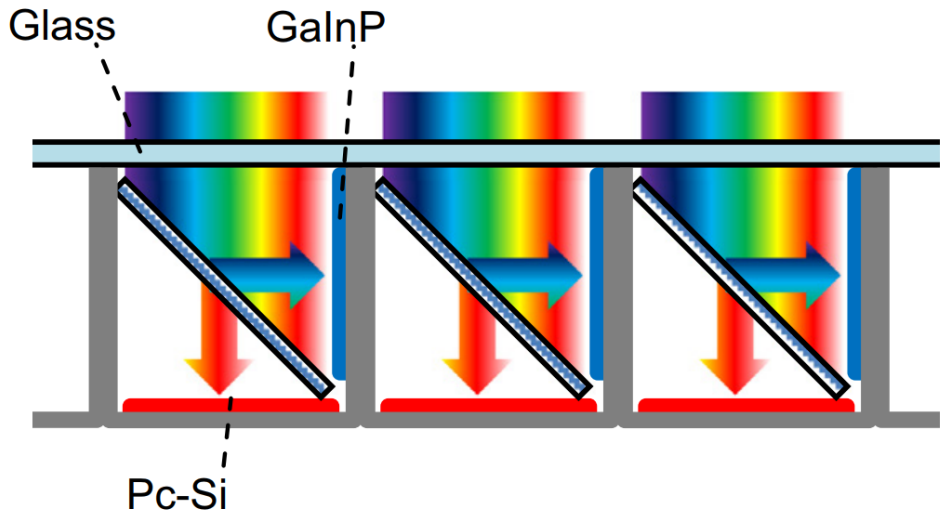

Figure 1.7: A spectral beam splitting configuration where a dichroic mirror reflects high energy light to the high band gap GaInP, and where low energy light is transmitted to the low low band gap Pc-Si, Reprinted from [15].

1.2.2. SPECTRAL BEAM SPLITTING CONFIGURATIONS

A different adaptation of the MJ approach is spectral beam splitting. Spectrally selective optical filters such as dichroic mirrors are used to decouple the irradiance spectrum, and redirect subsets of the spectrum to multiple physically separated junctions. The working principle is illustrated by the dichroic mirror in Figure 1.7. The ideal dichroic mirror has a transmittance of unity for a subset of the spectrum, and a reflectance of unity for all other wavelengths.

The advantages of the spectral beam splitting configuration over the stack approach lie in the inherent physical separation of junctions. Current matching is not required as the separate junctions are not connected in series, and tunnel junctions are also unnecessary. The mechanical challenges of epitaxial lattice matching or metamorphic design

also do not apply. Furthermore, the heat accumulation of a spectral beam splitting configuration is spread out over the various single-junction cells, and therefore easier to manage than a single stack. Finally, single-junction cells with different band gap energies can be deployed, and since these cells are not subject to the strict mechanical constraints of a multi-junction cell stack it is even possible to deploy several off-the-shelf PV cells with different band gap energies.

Figure 1.8 for example shows the spectral utilisation limit for GaAs and Si, with band gaps of 1.44 eV and 1.11 eV respectively. This limit assumes a beam splitting configuration that ensures photons with energies $E_{ph} \geq 1.44\ eV$ are absorbed by the GaAs cell, whilst photons with energies $1.44\ eV < E_{ph} \leq 1.11\ eV$ are absorbed by the Si cell. Furthermore, assumptions SQ2) through SQ6) are also invoked here. The joint spectral utilisation limit is 42.4%, which is already significantly higher than the SQ limits of just GaAs (32.9%) and Si (33.2%). This configuration is significant because GaAs solar cells and Si solar cells are readily available on the market, and proven to be economically competitive. It is thus implied that the higher efficiency can be attained at the same solar cell price level, and such a setup would have a better LCOE if the beam splitting configuration is not too expensive.

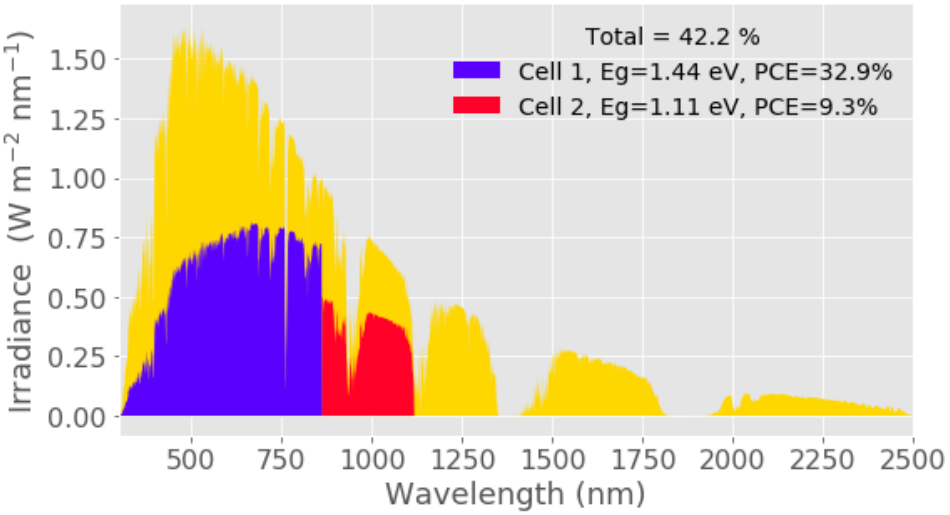

Figure 1.8: Joint detailed balance limited spectral utilisation potential of two technologically mature materials: Si (1.11eV) and GaAs (1.44eV).

Figure 1.9 depicts the limited spectral utilisation in case of four separate materials: GaInP with a band gap of 1.88 eV, GaAs with a band gap of 1.44 eV, Si with a band gap of 1.11 eV, and finally GaSb with a band-gap of 0.73 eV. This configuration is noteworthy because it was experimentally tested by scientists from the Fraunhofer ISE in 2010, whereby conversion efficiencies of 34% were attained outdoors [16]. The working principles of a beam splitting configuration have thus been demonstrated in an experimental setting, but the technological maturity of this approach has not progressed significantly beyond that setting.

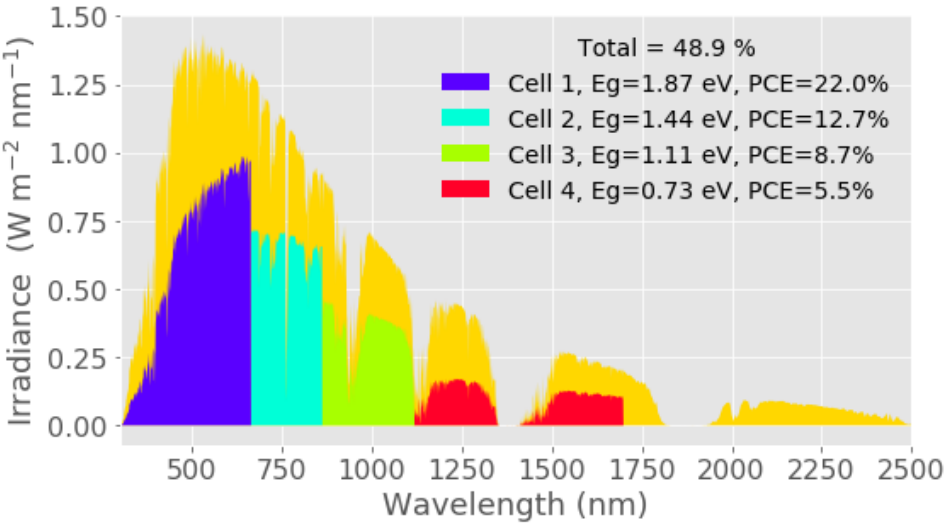

Figure 1.9: Detailed balance limited spectral utilisation potential of four single-junction PV materials: GaSb, Si, GaAs and GaInP, in order of increasing band gap.

The spectral beam splitting strategy also conveys drawbacks. Additional optical elements are of course accompanied by losses, and the optical losses of a practical dichroic mirror are typically larger than the optical parasitic losses due to tunnel junctions and imperfect transmittance in tandem cells. For the Fraunhofer four-junction configuration, the estimated total optical losses incurred by the beam splitting configuration amounted to 4.8%. Another drawback is that spectrally selective optical elements are typically very sensitive to angular deviations [15]. Dichroic mirrors for example optimally decouple the spectrum for an incidence angle of 45°, and lose performance at different incidence angles. Even for a simple terrestrial application, a mechanical reorientation system is therefore necessary to keep the incidence angle near 45° as the Sun apparently moves across the sky over time.

Both MJ approaches discussed enable energy conversion beyond the SQ limit, but come with significantly increased complexity and costs. For terrestrial energy generation, simply covering a larger area with significantly cheaper single junction cells is a superior strategy. This is clearly evident in Figure 1.3, where the MJ approach is absent. It can be concluded that, under ordinary terrestrial irradiance conditions, the MJ approach is not a commercially viable energy generating technology. Tandem cells have however demonstrated to be optimal for a different application, spaceflight, where the optimisation problem is fundamentally different. For MJ approaches to become economically viable on Earth, it is necessary to fundamentally transform the optimisation problem. It is exactly this that the field of concentrator photovoltaics (CPV) attempts.

1

1.3. CONCENTRATOR PHOTOVOLTAICS

Concentration is the redirection of irradiance incident on an area to a smaller area by means of optical elements. A suitable optical train, defined here as a system of optical elements designed to guide light, effectively redistributes the total incident irradiance. The goal is to have a small area receive higher flux. The concentration ratio C is conventionally defined as the dimensionless ratio of irradiance E to the irradiance contained within the $AM1.5G$ spectrum, $1000 W m^{-2}$.

$$C(E) = \frac{E}{1000 W m^{-2}} \tag{1.2}$$

Concentration brings about two main advantages for photovoltaics. Firstly, an increase in concentration typically results in an efficiency increase, i.e. a more than proportional increase in energy output. Secondly, only a relatively small area has to be covered with PV cells. This strongly synergises with more efficient yet more expensive energy conversion solutions such as the multi-junction approach. These two desirable properties incited research into concentrator photovoltaics. The realm of CPV is comprised of Low Concentrator Photovoltaics (LCPV) and High Concentrator Photovoltaics (HCPV), where LCPV corresponds to low concentration ratios $1 < C < 100$ and HCPV is characterised by concentration ratios $C > 100$.

It should be stressed that CPV is distinct from the field of concentrated solar power (CSP), which similarly concentrates irradiance via an optical train to a receiver area. The distinction is that CSP generates electricity from heat driving a turbine, rather than the photovoltaic effect.

Although CPV boasts the two aforementioned advantages, it also faces fundamental limitations and additional challenges that must be considered. This section will first expound how concentration allows for conversion beyond the SQ limit. Subsequently the drawbacks and limitations of CPV are discussed, starting with the most prominent one: irradiance availability.

1.3.1. EFFICIENCY AS A FUNCTION OF CONCENTRATION

The vast majority of conventional PV technologies exhibit an approximately logarithmic increase in efficiency, as C increases. This phenomenon is illustrated in Appendix A.2. In Figure 1.4 the largest share of the 'other losses' are due to the V_{MPP} being lower than the band gap, and concentration essentially alleviates this fundamental loss contribution. Concentration violates assumption SQ2, which is why exceeding the SQ limit is possible. The theoretical efficiency limits per junction number from [6] under a single Sun and optimal concentration are tabulated in Table 1.1.

Table 1.1: The theoretical limit for 1J, 2J, 3J, 4J and infinite junction cells under a 6000K blackbody spectrum and under maximum concentration, copied from [6].

Concentration	1J	2J	3J	4J	∞J
1 (one Sun)	31.0 %	42.7 %	49.1 %	53.0 %	69.9 %
46,050 (max)	40.8 %	55.6 %	63.5 %	68.4 %	86.8 %

As documented in Appendix A.2, the initial trend of increasing efficiency as a function of concentration does reverse at very high concentration levels. A concave characteristic follows, such that there exists a concentration ratio at which efficiency has a maximum. The optimum ratio varies per material, but it is generally orders of magnitude larger than unity. It is therefore implied that concentration generally enhances efficiency. For often used multi-junction configurations, the optimum concentration ratio typically varies between 100 and 1000 equivalent Suns. For the dominant single-junction Si, the optimum concentration ratio also stands at approximately 100 equivalent Suns [17]. The concentration response of a typical GaInP/GaInAs/Ge cell is depicted in Figure 1.11, which shows an experimental optimum around 400 suns.

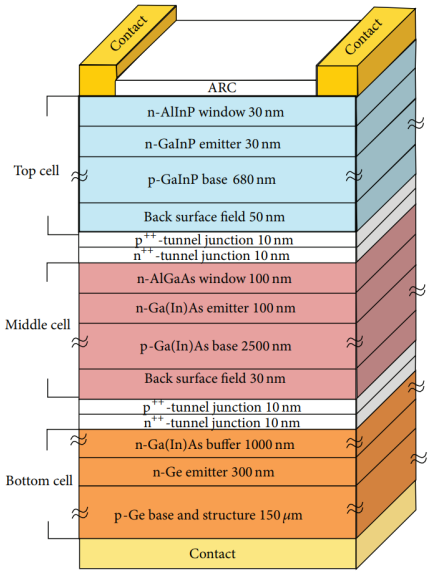

Figure 1.10: A typical triple-junction GaInP/Ga(In)As/Ge cell, reprinted from [18].

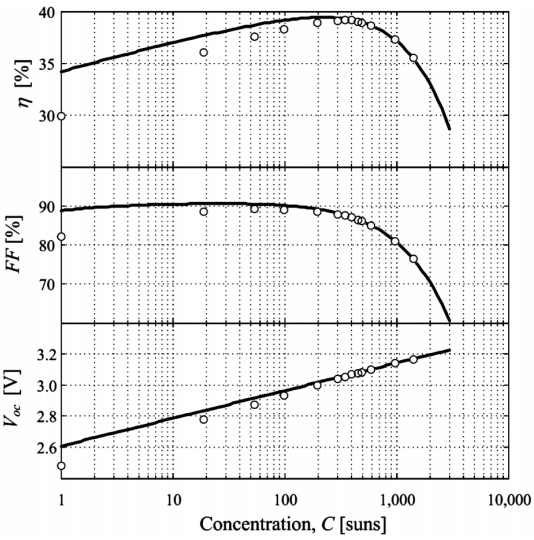

Figure 1.11: The concentrator response of a GaInP/GaInAs/Ge cell, reprinted from [12]. The dots represent observations, whilst the solid lines are fitted to these observations.

1.3.2. DIRECT NORMAL IRRADIANCE

A fundamental limitation of CPV is that a system employing concentrating optics can only access a subset of the incident irradiance. The total irradiance incident on a surface, Global Horizontal Irradiance (GHI), consists of three collectively exhaustive components: direct, diffuse, and albedo. The three components correspond to respective solid angles from which the irradiance originates. Direct Normal Irradiance (DNI) is defined as originating from a cone centred on the Sun with an opening half-angle of 2.9°. Diffuse Horizontal Irradiance (DHI) is irradiance from the entire sky excluding the solid angle reserved for DNI, and the albedo component is irradiance reflected by non-atmospheric objects like the ground. The albedo component is obviously location-

specific and often comparatively negligible in magnitude, such that it is not included in analyses based on a reference standard setting. The simple irradiance relation is therefore as follows:

$$E_{GHI} \approx E_{DNI}(< 2.9^{\circ}) + E_{DHI}(> 2.9^{\circ}) \tag{1.3}$$

Scattering of light in the atmosphere increases DHI and decreases DNI, such that the relative proportion of DNI directly depends on atmospheric parameters. In clear weather DNI is by far the largest component, which is why refractive and reflective optical elements focus on capturing DNI. Even for a concentrating system with a very low concentration ratio, the fraction of DHI arriving at the receiver area is negligibly small. This inability to convert diffuse irradiance is a disadvantage compared to flat-plate modules, but the significance of this disadvantage strongly depends on location. Total annual irradiance is highest for locations with minimal atmospheric obstruction, such that locations with excellent solar potential also have a relatively large DNI component. An overview of global DNI incident on a plane perpendicular to the Sun is presented in Figure 1.12, from which it can be concluded that locations with ample DNI exist.

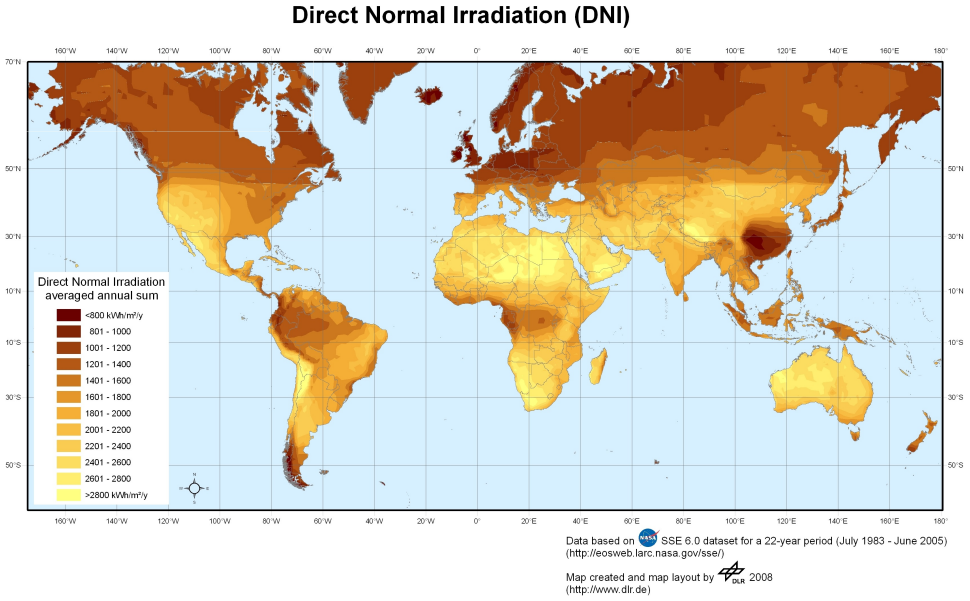

Figure 1.12: Global average annual direct normal irradiance, from [19].

Recognising that irradiance conditions are strongly location-dependent and also strongly time-variant, reference spectra are essential to compare various PV systems on a fair basis. Gueymard's work ([5]) forms the basis of the established standard spectra. Gueymard investigated representative parameters, such as aerosol optical depth, that serve as inputs for the Simple Model of the Atmospheric Radiative Transfer of Sunshine (SMARTS). SMARTS maps the irradiance arriving at the outer atmosphere (AM0 spectrum) into ter-

restrial irradiance using a radiative transfer model of atmospheric interactions. All representative parameters from [5] are tabulated in Appendix A.3.

Two particular SMARTS output spectra are especially important: the full GHI computation that considers all incident irradiance, and the DNI computation for a total opening angle of 2.9ř centred on the Sun. Notice that the 2.9ř opening half-angle is significantly larger than the solid angle subtended by the Sun itself, which varies from 0.262ř to 0.271ř due to the Earth's elliptical orbit. As such, the reference DNI spectrum by definition includes some irradiance originating from the annulus surrounding the Sun, defined as circumsolar irradiance. However, this circumsolar irradiance contributes less than 1% to the total DNI under the atmospheric conditions considered for the SMARTS reference spectra [20]. The SMARTS spectra have been adopted by the American Society for Testing and Materials (ASTM) as the AM1.5D and AM1.5G spectra, respectively. Both spectra are depicted in Figure 1.13 as functions of photon energy. Note that the two spectra are derived under the same conditions, the only difference being the opening angle the AM1.5D spectrum is limited to.

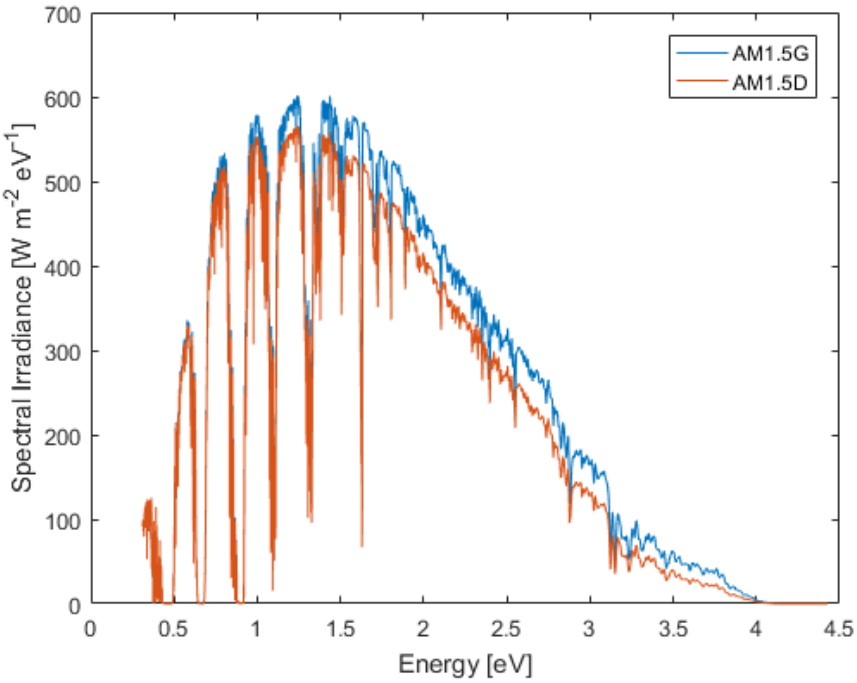

Figure 1.13: The standardised AM1.5G and AM1.5D spectra, transformed to an energy [eV] scale.

Comparing the reference DNI and GHI spectra from Figure 1.13, it appears that the DNI curve is shifted downward by 30 to 40 $Wm^{-2}eV^{-1}$ for photon energies above 1.2 eV. This difference is exactly DHI per Equation (1.3), i.e. the mostly blue sky outside the AM1.5D opening angle. This not only results in a different spectral profile, but also

of course in a significantly smaller integral over the entire spectrum: the integral over AM1.5D is about $890 Wm^{-2}$, versus about $1000 Wm^{-2}$ for AM1.5G. The diffuse component is quite significant even in clear-sky conditions, such that a CPV system is necessarily limited to a subset of the irradiance available to a flat-plate PV system. However, it should be stressed that the sharp 5.9° opening angle defining DNI is rather arbitrary. The irradiance available to a concentrator system depends on its specific topology, and is fundamentally limited by the concentration ratio. LCPV topologies are typically capable of utilising irradiance from slightly outside e 2.9° opening angle as well, whilst HCPV systems are even constrained to a subset of the AM1.5D spectrum.

1.3.3. ANGULAR DEVIATION EXACERBATION

A second important limitation of CPV is that the irradiance incident on the receiver area is necessarily non-collimated. This necessity follows from the fundamentals by which concentration is achieved and the fact that the Sun is not a point source. Note that concentrating optical elements only function optimally for a particular orientation they are 'aimed' at. An ideal lens guides rays of light that are parallel to its axis to a focal point, but off-axis rays by definition do not end up in the focal point. Also note that the Sun is an extended source, appearing as a disk to an observer on Earth. An ideal lens would redirect the largest share of the incident flux to the neighbourhood of the focal point, if its axis were aligned perfectly with the centre of the Sun's disk. Rays from the Sun's edge will deviate from the focal point, but the total deviations are minimal for the orientation where the Sun's centre and the lens' axis overlap. Fundamentally though, it is inevitable that angular deviations exist even for an idealised optical element.

In any optical configuration where light is concentrated, such angular deviations are exacerbated. This is a direct consequence of conservation of étendue, which in turn is a manifestation of the second law of thermodynamics. It is a necessary property, as it cannot be decoupled from how concentration is actually achieved. Étendue and non-imaging optics in general are well-documented, for instance in [21]. As the extent of concentration increases, two incident rays will necessarily be mapped to rays with an increasing angle between them. It is this phenomenon that is referred to as angular deviation exacerbation in this thesis. Figure 1.14 illustrates how even in the case of idealised optical elements an initial angular deviation is exacerbated.

Referring to Figure 1.14, consider a hypothetical perfect incident ray incident on p1. By definition of the parabolic mirror with focal length f_P, any ray parallel to its vertex is redirected to the focal point F. The ray passes through F, and arrives at the perfectly thin converging lens at the point l_1 with focal distance f_L. Note that the lens is perfectly aligned to also have F as its focal point. By definition of a converging lens, any ray emanating from its focal point will be perpendicular to the lens after passing through.

Next, consider any ray incident on the point $p1$ that is not parallel to the parabola's vertex, but instead deviates by an angle θ_i. This ray becomes the red ray in Figure 1.14 after reflection, which does not pass through the focal point F and intersects the lens at a different point l_2 instead. From this point of intersection, it is of course possible to draw a line through the focal point, which intersects the parabola at the point $p2$. Note that,

since this line passes through the parabola's focal point, by definition it corresponds to an incident ray parallel to the vertex. Additionally, by definition of the converging lens, this ray is also perpendicular to the lens after passing through the point l_2. Note that the green lines are thus subject to similar operations, and both are parallel to the vertex before incidence and after passing through the lens. The distance between the green lines is a measure of concentration. E_i denotes the incident irradiance, and E_c the concentrated irradiance.

Now, crucially, note that the deviating red line will not be perpendicular to the lens after passing through l_2; a ray striking l_2 will only be if it passes through the point F. Instead, it will be at an angle θ_c, approximately equal to $\angle(p_1, l_2, p_2)$, i.e. the angle between the red ray and the ray from p_2. This angle θ_c is larger than the initial deviation θ_i if and only if the focal length ratio $\frac{f_P}{f_L} > 1$. This focal length ratio is also exactly how concentration is achieved. Reducing f_L, i.e. placing a stronger lens closer to the mutual focal point F, increases the ratio ceteris paribus. Repeating the procedure outlined in the previous paragraph for the new geometry would yield an increase in both the concentrated irradiance E_c and the angle θ_c. There is a positive relationship between the degree of concentration and the angular exacerbation from θ_i to θ_c. It should be stressed that this phenomenon is a necessary property, and that it arises even if ideal optical elements are considered. Furthermore, recall that the Sun is not a perfect point source, implying deviating rays like the red one in Figure 1.14. Although the deviation between the centre of the Sun and the edge of the Sun is only 0.266°, much smaller than θ_i in Figure 1.14, the concentration ratio is also much larger than illustrated, particularly for HCPV systems.

This angular exacerbation implies that concentrated flux will be intrinsically less collimated than the direct normal irradiance. Optical errors that will be discussed later further augment this phenomenon. Baig et al. [22] present an overview of the problems induced by non-collimated irradiance relevant for CPV performance. The resulting conversion loss depends on the implemented energy conversion method, but for the prototypical multi-junction tandem cell it always constitutes a significant problem as documented by Herrero et al. [23]. The Fresnel equations dictate that the transmission of light into the tandem cell directly depends on the angle of incidence. It is implied that current generation within the tandem cell will vary locally and across junctions, such that the efficiency of the entire cell will be limited by the lowest current. Likewise, heat accumulation will also vary locally and across junctions, and also limit the system as a whole.

For spectral beam splitting approaches, non-collimated irradiance poses an even larger problem. The properties of dichroic mirrors - typically stacks of alternating dielectric materials - worsen significantly as the angle of incidence deviates from 45°, in the sense that irradiance that ought to be transmitted is increasingly reflected and vice versa. The more significant the angular exacerbation, the less effective beam splitters become. Additionally, the angle of incidence on the receivers following the beam splitters will also be suboptimal. In Figure 1.7, hypothetical incident rays other than the depicted 0ř beam will be split and absorbed less efficiently. To circumvent these problems, sec-

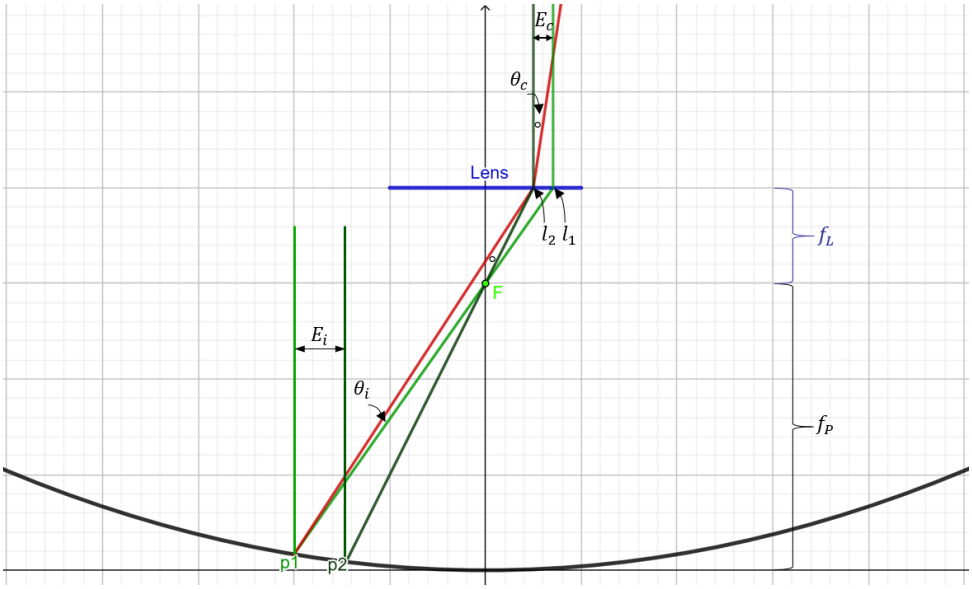

Figure 1.14: Illustration of angular exacerbation as a necessary consequence of concentration. Higher concentration $\frac{E_i}{E_c}$ is intrinsically tied to a higher angular exacerbation $\frac{\theta_c}{\theta_i}$; see the text for an explanation of the figure.

ondary optical stages are often used in CPV systems to collimate the irradiance again after the necessary deviations induced by the first concentrating stage. Nevertheless, fundamental deviations in the incident irradiance exist even with a well-designed secondary stage. The Sun is not a point source, and manufacturing errors, tracking errors and local atmospheric factors are inevitable. Under concentration such small errors - which are insignificant for ordinary PV systems - are exacerbated. It is a fundamental drawback that receiver irradiance is necessarily less collimated post concentration - especially so with realistic errors - and any energy conversion strategy suffers from this lesser extent of collimation.

1.3.4. OTHER FUNDAMENTAL LIMITATIONS AND CHALLENGES

CPV suffers from more fundamental limitations, and additional design challenges arise. Another fundamental loss stems from the optical train itself. Practical mirrors do not just reflect light, but also absorb and transmit a small fraction. Refraction by a lens also incurs an optical efficiency loss. The throughput of an optical train depends on both the geometry and material choice [24], but it is always less than the input.

Another limitation for CPV is that a tracking mechanism is absolutely necessary. The Sun apparently moves across the sky, requiring either the optical elements to adjust their orientation or the receiver to move accordingly. Tracking accuracy becomes progressively more important as the concentration factor increases. Up to a concentration factor of 70x, single-axis tracking can still be sufficient and the economically optimal

choice, but for higher concentration factors dual-axis tracking is required. A tracking mechanism represents additional costs, and constitutes a significant share of total costs for CPV systems [12]. It should also be noted that tracking is not inherently a drawback, as it increases the irradiance a system receives by ensuring that the system is continuously perpendicular to the Sun's rays. This essentially increases the equivalent annual sun hours relative to a case without tracking and readjustment. Even for ordinary flat-plate PV systems, a single-axis tracking mechanism can be an economically justifiable expense for various locations on Earth [25]. However, because tracking constitutes a requirement rather than a design option in case of CPV systems, it must be interpreted as a limitation.

Furthermore, meticulous thermal management is necessary for CPV applications. In a PV module, the portion of energy not immediately reflected or converted ultimately ends up as heat. Indeed, all loss mechanisms indicated in Figure 1.4 end up in the form of heat. Assuming a single-junction module with a realistic initial reflectivity of 5% and a high conversion efficiency of 20%, 75% of the total irradiance is ultimately converted into heat. This is problematic, because a PV cell's efficiency typically decreases as its operating temperature increases [26]. This constitutes an important design problem for flat-plate PV systems, where even systems with well-designed passive heat sinks reach operating temperatures that significantly decrease conversion efficiency already. Now, even though the percentage of irradiance accumulating as heat is lower for CPV systems because of the higher conversion efficiency, concentration implies significantly more heat accumulation per unit area. Rather than a design problem, this increased heat flux poses an operational threat for CPV systems. Adequate thermal management is absolutely necessary to maintain operating conditions.

On the other hand, the intensified heat accumulation can also be utilised to some extent. After all, the established and rapidly growing field of Concentrated Solar Power (CSP) essentially converts a concentrated solar flux into heat to drive a thermal electricity generation process. The combination of CPV and CSP, where a PV component converts a portion directly and the heat is also utilised, is known as the field of concentrated photovoltaic thermal (CPVT) [27]. CPVT strategies theoretically boast extremely high energy conversion, solving both the spectral utilisation limitation of PV cells - by only allocating the suitable subset of the spectrum to the PV subsystem - as well as the thermal management problem by actually converting the thermal energy. CPVT as an industry however is in an even more fledgling state than CSP and CPV. The ever-fluctuating nature of practical irradiance conditions make CPVT strategies complex to execute.

All in all the increased efficiency, CPV represents a vastly different set of design limitations and opportunities. The CPV system design optimisation problem fundamentally differs from the ordinary flat-plate PV case. Importantly, the significantly smaller receiver area makes relatively expensive but efficient candidate receivers more attractive. The MJ approach clearly falls into this category, and the synergies with CPV are apparent.

1

1.3.5. THE STATE AND OUTLOOK OF CPV

CPV has mostly manifested as a utility-scale generation technology, and high-concentration photovoltaics (HCPV) constitutes more than 90% of the cumulative installed capacity [28]. HCPV refers to concentration factors over 100x, and as such absolutely requires dual-axis tracking. Recall from subsection 1.3.1 that the interesting semiconductor materials typically exhibit a maximum efficiency in the HCPV range. Furthermore, for HCPV systems the advantage of comparatively less required PV cell area is more significant. No universally adopted optical train configuration exists, but the majority of the installed capacity features a Fresnel lens as the first optical stage [27]. An overview of popular optical train configurations currently used in CPV systems is given in [12]. In recent years, the CPV landscape has almost completely shifted to multi-junction conversion because of the aforementioned synergy [29]. The cumulative installed capacity stands at about 370 MW_p globally, but annual deployment has fallen in recent years [28]; see Figure 1.15.

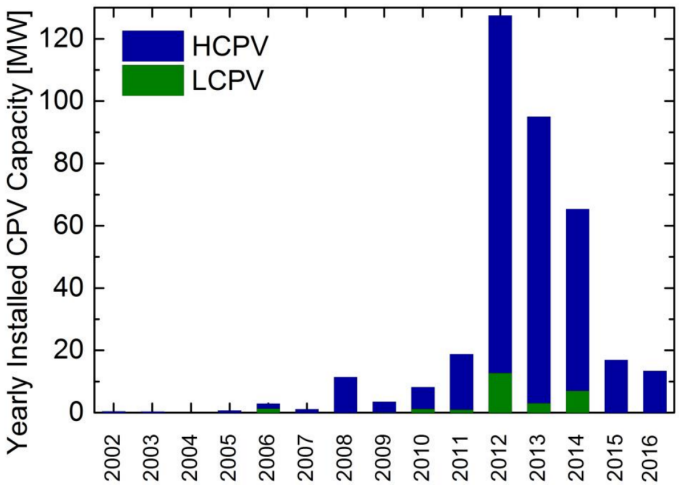

Figure 1.15: Annual installed capacity for HCPV and LCPV

The decrease in annual CPV installations is a result from the significant LCOE decrease exhibited by silicon-based PV (Figure 1.2) as well as the impact of the severe 2007 financial crisis, which steered decision-makers towards relatively safe, mature technologies. It should be noted that CPV systems compete directly with flat-plate PV because of the similar power output characteristics. As such, the investment decision between a CPV system and an ordinary PV system is largely based on LCOE (Equation (1.1)), and therefore energy output and costs. Silicon-based PV prices dwindled due to a combination of rapidly scaled manufacturing as China took on the mantle as dominant supplier, and the end of the silicon shortage in 2008 [29]. These cost reductions have outweighed the more rapid technological advancement of tandem cells, which have seen the strongest and most sustained improvement rates amongst PV technologies in recent years [30]. A 2015 NREL breakdown of costs demonstrates the difference: for a reference multi-junction CPV system with a Fresnel lens, the optical train and dual-axis tracking

respectively already represent $0.20\frac{\$}{W_p}$ and $0.30\frac{\$}{W_p}$ [31]. For comparison, an entire flat-plate Si module would cost about $0.57\frac{\$}{W_p}$ at the time. Whilst a comparison of the price per peak power rating is not entirely representative - as systems with trackers will capture more irradiance - the fact that just the optical train is about as expensive as an entire flat-plate energy conversion system paints a gloomy picture for HCPV. The costs of the MJ energy conversion solution are not even factored in yet, and these costs are sizeable. The numbers suggest that the traditional Fresnel lens approach simply cannot compete with flat-plate PV. The optical train alone is too expensive and this expense is not justified by the additional output of a multi-junction conversion approach. Stated differently, the conventional CPV motivation of employing cheap optics to offset the expensive PV cell no longer holds, as the PV cell itself became cheaper than the relatively complex optical system. For HCPV to succeed, it is necessary to achieve the high efficiencies at a relatively affordable optical system cost.

In addition to installed capacity, it is also insightful to consider the historic evolution of prices. Haysom et al. estimated the learning curves for HCPV, CSP and flat-plate PV [32]. The resulting log-log plot of the turn-key price versus the cumulative installed capacity is depicted in Figure 1.16. It should be stressed that the horizontal axis indicates cumulative installed capacity and not time, as was the case for Figure 1.2. The points in Figure 1.16 do not necessarily correspond to successive years; instead, they correspond to publications where both cumulative capacity and the turn-key price were simultaneously known or estimated. The learning curves' downward trends are not to be understood entirely as technological advancement, since increasing economies of scale by themselves would also result in a downward trend in the absence of technological advancement. Learning curves capture the joint contribution of economies of scale and technological advancement to price evolution, and can therefore be interpreted as the overall effect on price levels of manufacturers 'learning' from experience, be it technologically or economically.

From Figure 1.16, at first glance HCPV appears to be an attractive alternative to regular PV because its learning curve is steeper and because its learning curve is shifted to the left. Even in the aforementioned absence of a universally accepted optical train - which every party could learn from and improve upon - apparently the technological and economical learning is significant. However it should be stressed that it cannot be concluded that HCPV is technologically superior to flat-plate PV, especially considering the aforementioned silicon shortage which ended in 2008. The final flat-plate PV entries show a markedly steeper learning curve than before, and the flat-plate PV market has experienced explosive growth since the most recent data point from Figure 1.16: global PV capacity is over $627GW$ [33]. Of course, it should also be pointed out that whilst a steep learning curve is desirable, it is obviously of no benefit if a technology does not move along its curve. In light of Figure 1.15, this point should not be taken lightly. Instead, a learning curve both steeper and shifted to the left should be interpreted as a necessary condition for a technology to become viable. As such, it can only be concluded from the exhibited learning curves that economic viability of HCPV might be possible.

In order to attain actual economic viability a significant increase in efficiency or de-

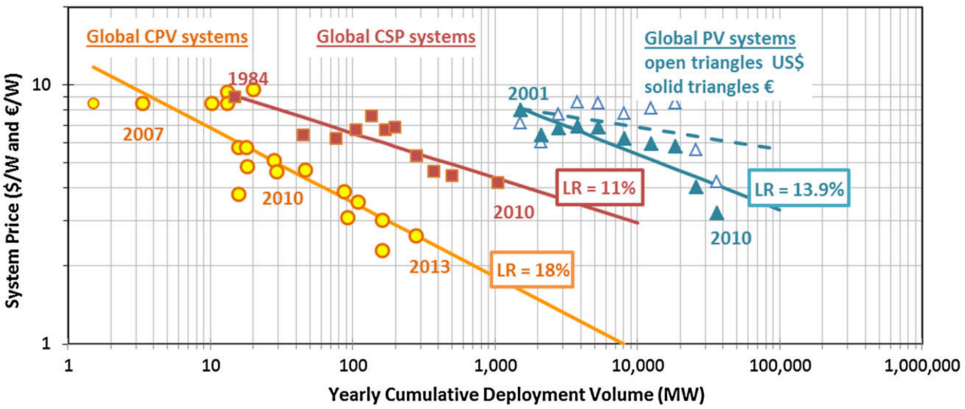

Figure 1.16: Learning curves and the average learning rate (LR), plotted for HCPV (>200 Suns), CSP and flat-plate PV from [32].

crease in costs is necessary, whilst simultaneously the unique limitations of CPV must be addressed. The exact road towards competitiveness has not been determined yet, but potential factors that have been identified are scaling and maturity [31], increased efficiency through innovation [28] and possibly thermal energy utilisation, e.g. a steam turbine [34] or desalination [35]. The declining annual installed capacity in Figure 1.15 paints a pessimistic picture, but on the other hand Figure 1.16 suggests that CPV is not intrinsically inferior. The consensus is that CPV could be superior to flat-plate PV for locations with ample DNI, but the viability of CPV hinges upon innovation and cost reduction [29] [28].

In the related, rapidly growing field of CSP, where a concentrating optical train is used to essentially heat a central receiver, the topology of choice for utility-scale systems is shifting towards that of a solar tower [36]. Solar tower systems employ an array of mirrors, often simple flat ones, called heliostats. Heliostats reorient themselves to continuously reflect sunlight to a central receiver, and the accumulated heat at this central receiver is used to drive an electricity generation process. Heliostats including dual-axis tracking currently cost about $100\frac{\$}{m^2}$, and are projected to decrease to a target figure of $75\frac{\$}{m^2}$ due to technological advances as well as returns to scale in production [37]. Davila-Peralta et al. documented a heliostat design that is estimated to reach an installed cost on the order of $60\frac{\$}{m^2}$ assuming mass manufacturing [38].

The relative contribution of heliostat array costs to total system costs in $\frac{\$}{W_p}$ terms depends on many system-specific factors - most important factor being energy conversion efficiency - but it is possible to estimate a representative case. Assuming a total optical train loss from heliostat to multi-junction receiver of 10%, the flux arriving at the receiver will be approximately $900\frac{Wp}{m^2}$ based on the standard testing conditions of $1000\frac{Wp}{m^2}$. At a conversion efficiency of 40% and the target installed heliostat cost of $75\frac{\$}{m^2}$, a heliostat

cost contribution of about $0.21\frac{\$}{Wp}$ follows, which is significantly less than the $0.50\frac{\$}{Wp}$ corresponding to the Fresnel primary optic with trackers.

Whilst a heliostat array is likely the cheapest primary optic candidate for CPV systems, it also conveys drawbacks. Most important is optical performance; an array of flat mirrors approximating a parabola is inferior to a parabola in terms of energy throughput for a variety of reasons. Firstly, there is spacing between heliostats in array, resulting in irregular flux at the receiver. Additionally, perpendicular light rays leaving a flat mirror do not intersect, implying that the lion's share of the flux arrives near the focal point instead of at the focal point. The sacrifice in optical performance might even interact with the inherent exacerbation of angular deviations described in Section 1.3.3, possibly resulting in an optical throughput that is fundamentally incompatible with the sensitive HCPV receiver candidates. Yet another problem that comes to mind is whether the multi-junction approach is feasible for solar tower receivers on the order of metres, seeing as the scale of almost every existing HCPV receiver is on the order of centimetres. The fundamental question is whether CPV and a heliostat array are compatible, and the answer to this question necessitates a characterisation of the optical performance loss.

1.4. RESEARCH GOALS

Having introduced the field of CPV and in particular its unique design challenges and limitations, this section will introduce the objective of this thesis. As was mentioned before, CPV can only succeed if systems achieve higher output through justifiable increased costs. Small-scale CPV optical trains - such as the dominant Fresnel lens topologies - are relatively complex, and by themselves approximately as expensive as entire flat-plate PV module in terms of $\frac{\$}{Wp}$. Heliostat arrays represent the cheapest primary optical stage available, but also represent a loss in optical performance compared to parabolic mirrors. Of crucial importance is the extent of this performance loss for CPV applications, i.e. whether utility-scale HCPV with a heliostat array is feasible. In the absence of drastically cheaper alternative primary optics, it even follows that the viability of HCPV as a terrestrial energy generation technology depends on heliostat feasibility. Quantifying the optical performance in HCPV is a problem in itself, as there is no existing metric, framework or model. Establishing such a framework is the central problem this thesis seeks to address.

Firstly, it is postulated that it is necessary to calculate the propagation of radiant energy in its most extensive form for a particular optical train topology. As Chapter 2 demonstrates, the conventional methodology of an AM1.5D spectrum upscaled by a topology-specific geometric concentration factor $C(E)$ defined in Equation (1.2) is invalid. To evaluate an optical train properly, radiant energy must be mapped throughout the optical train in its most extensive form. Spectral radiance should serve as the quantity of analysis, since CPV energy conversion solutions have a wavelength-dependent efficiency and also because of the aforementioned angular deviation exacerbation inherent in high concentration systems. Unfortunately, no spectral radiance standard analogous to the AM1.5D spectral irradiance standard exists yet, which precludes a standardised approach to this calculation. It is of utmost importance to establish such a spectral

radiance standard.

This thesis postulates a workhorse spectral radiance source representation that could be used to characterise HCPV systems. Chapter 2 will motivate the necessity of such a model in further detail. The candidate spectral radiance source representation is derived from the AM1.5D spectral irradiance standard - widely accepted in the CPV literature - using a wavelength-dependent solar limb darkening model from astronomy literature. Crucially, the spectral sunshape considers the dependence of flux on both wavelength and its exact origin on the solar disk. The derived spectral radiance model will be compared to current state-of-the-art models of the Sun from both the PV and CSP literature. In paricular, it will be demonstrated how the simplifying assumptions underlying the use of these current models invalidate HCPV analyses. Finally, it is shown how software can implement the derived spectral radiance source model, such that the capabilties of existing software can be extended to enable valid HCPV analyses.

Chapter 3 then incorporates a realistic optical error model for heliostat operation into the analysis. Initially, a geometric optics framework for propagation is motivated and developed. Optical errors are introduced, and a heliostat error model is combined with the spectral radiance source model to arrive at a representation of heliostats as effective sources. As will be documented in Chapter 3, an effective source representation has the potential to greatly reduce the processing power required to calculate the optical performance of a HCPV system. The source representation and heliostat error model finally enable fully characterising the performance price paid upon replacing the paraboloid mirror by a heliostat array, and and the thesis concludes with a geometric optics framework that can be used to compare the ideal parabolic mirror primary stage to a heliostat array.

2

SPECTRAL SUNSHAPE

This Chapter documents the spectral sunshape, a workhorse spectral radiance model of the Sun. It is essentially a vector field representation of the Sun, where irradiance is characterised as a function of both wavelength and polar angle. Section 2.1 introduces the concept of spectral radiance, and defines the spectral sunshape formally. Afterwards, a rationale for the spectral sunshape as the source representation of choice for HCPV applications is provided in Section 2.2. Section 2.3 then discusses well-established solar flux standards are essentially derivative forms of the spectral sunshape. Of course, it is a necessary condition for a candidate spectral sunshape representation to reproduce these established standards. Finally, Section 2.4 develops an analytical functional form for the spectral sunshape based on the phenomenon of solar limb darkening, well-documented in astronomical literature. The ultimate goal of this chapter is arriving at an estimate for the spectral sunshape, based on the literature and industry standards.

2.1. DEFINITION

Prior to deriving a spectral radiance representation of the Sun, it is instrumental to first define spectral radiance itself. A background on the radiometric quantities introduced in this section can be found in e.g. [7] or [39]. Radiance L is the radiant power received or emitted by a given surface per solid angle. It serves as the fundamental quantity in radiometry, and has units $[Wm^{-2}sr^{-1}]$. Radiance is thus irradiance per solid angle, and measures the directional distribution of power. Analogous to how spectral irradiance $\frac{\partial E}{\partial \lambda}$ denotes differential irradiance per wavelength, let us define spectral radiance as the differential radiance per wavelength:

$$\mathscr{L}(\lambda,\omega) \overset{def}{=} \frac{\partial}{\partial \lambda} L(\omega) = \frac{\partial}{\partial \lambda}\left(\frac{\partial E}{\partial \omega}\right) = \frac{\partial^2 E}{\partial \lambda \partial \omega} \tag{2.1}$$

The latter equality indicates that spectral radiance can also be thought of as spectral irradiance per solid angle, or as radiance per solid angle per wavelength. Even though angles are dimensionless, the spectral radiance units are denoted as $[\mathscr{L}(\lambda,\omega)] = Wm^{-2}nm^{-1}sr^{-1}$ to emphasise angular dependence.

Spectral radiance as defined above is a general physical quantity, which applies to any setting involving radiative transfer. Consider in particular the setting of a HCPV system on Earth, for which the Sun appears as the product of Figure 2.1 and a journey through Earth's atmosphere. The spectral radiance in this case is defined as the spectral sunshape $\mathscr{L}_{\odot}(\lambda,\theta)$:

$$\mathscr{L}_{\odot}(\lambda,\theta) \overset{def}{=} \frac{\mathscr{L}_{\odot}(\lambda,\omega)}{2\pi} \tag{2.2}$$

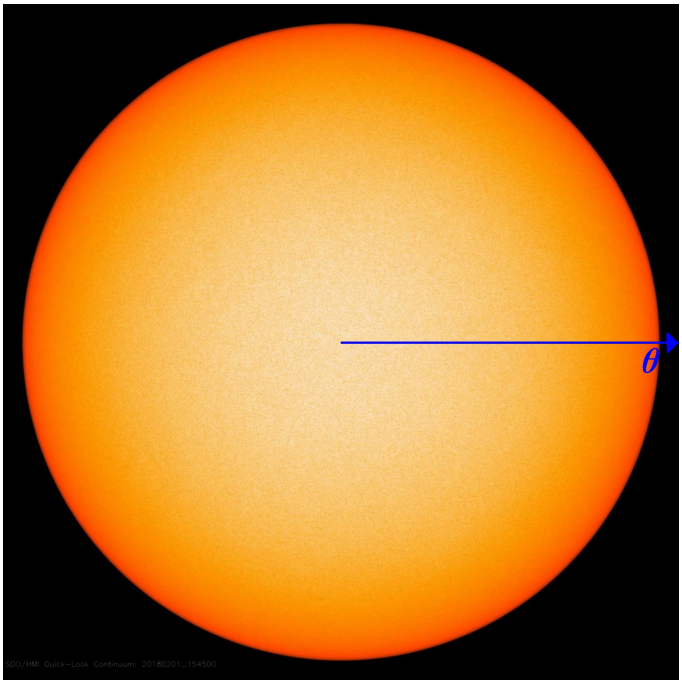

Figure 2.1: A photograph of the Sun, adapted to depict the definition of the opening half-angle θ. Adapted from the image labelled PIA22242 of the NASA Jet Propulsion Laboratory's Photojournal.

The opening half-angle θ is defined as the angle with respect to the solar vector. The solar vector is defined as the vector pointing from the very heart of the Sun to an observer on Earth. It follows that $\theta = 0°$ corresponds to the solar vector. The opening half-angle is the only considered polar variable because of assumed azimuthal symmetry, i.e. the expected spectral radiance is invariant under rotation of the axis in Figure 2.1 around the centre of the Sun. Since this assumption is made for an observer on Earth, it should not just hold for Figure 2.1 but also still hold after passing through Earth's atmosphere. For clear sky settings when the Sun is not very close to the horizon, this assumption is very reasonable [40] [41] [42]. This assumption is also supported by the practical fact that a HCPV system is typically limited to direct irradiance, and the correlation between direct irradiance and clear sky conditions. Transforming the solid angle ω dependence into an opening half-angle θ dependence under azimuthal symmetry is equivalent to divid-

ing by the factor 2π. The spectral sunshape as defined in Equation (2.2) is the radiance corresponding to a particular vector - not the entire cone - forming an angle θ with the Sun's centre. That is, $\mathscr{L}_{\odot}(\lambda, \theta_{edge} = 0.266°)$ corresponds to the spectral radiance from any vector from the very edge, not the total spectral radiance contributed by the entire circle.

2.2. RATIONALE

As was extensively reviewed in Section 1.1, various PV technologies differ in their spectral response. Designing an intrinsically spectrally selective receiver requires a spectral source representation, such as the AM1.5G and AM1.5D spectra in Figure 1.13. For flat-plate PV systems, dissecting just this one property of solar flux is sufficiently accurate. Although the Sun is not a point source, it is sufficiently far away to treat it as such. The very edge of the Sun's photosphere, visible in Figure 2.1 corresponds with a opening half-angle of just $\theta_{edge} = 0.266°$. For a flat-plate PV module, even though light from the photosphere's edge technically arrives at a different angle relative to light from the very centre, the cosine law's effect is negligible.

If the solar flux is concentrated however, small deviations are necessarily exacerbated due to conservation of étendue. This principle was illustrated in Section 1.3.3. Conservation of étendue essentially implies that the angular deviation of $\theta_{edge} = 0.266°$ between a ray from the centre of the Sun and a ray from the photosphere edge will increase as these rays are mapped through a concentrating optical train. Post optical train, the resulting rays can be significantly divergent. The higher the concentration, the lower the upper bound on the angle between the two resulting rays.

This principle is important, because the origins of the edge and centre ray are markedly different. Intensity and spectrum strongly depend on θ, as is apparent in Figure 2.1's non-uniformity in colour and brightness. This effect is known as solar limb darkening, and it mainly follows from two phenomena. Firstly, both the temperature and density decrease as the solar radius increases, such that the emission spectrum varies with solar radius. Secondly, the solar radius from which photons arriving at Earth originate depends on the half-angle θ, because the radial distance corresponding to an optical depth varies; see Figure 2.2 for an illustration.

The emission spectrum's dependence on radius is easily illustrated. Recall that the solar limb, i.e. the edge of the photosphere, is at $\theta_{edge} = 0.266°$. For notational convenience, arcminutes (') will be used from here onwards as the unit for half-angle, motivated by the fact that $0.266° \approx 16.0'$. Hence, the domain considered is $\theta \in [0', 16']$. For $\theta = 0'$, the photons originate in the deepest layer of the photosphere where the temperature is approximately $6400K$. At the limb, i.e. $\theta = 16'$, the temperature is only approximately $4400K$. To indicate the impact on the emission spectrum, consider blackbodies in thermal equilibrium. This is a decent first-order approximation for a shell at a given radius, and therefore temperature, of the Sun. For a blackbody in thermal equilibrium, the spectral radiance as a function of temperature follows Planck's law:

$$B_T(\lambda) = \frac{2hc^2}{\lambda^5 (e^{\frac{hc}{Tk_b\lambda}} - 1)} \tag{2.3}$$

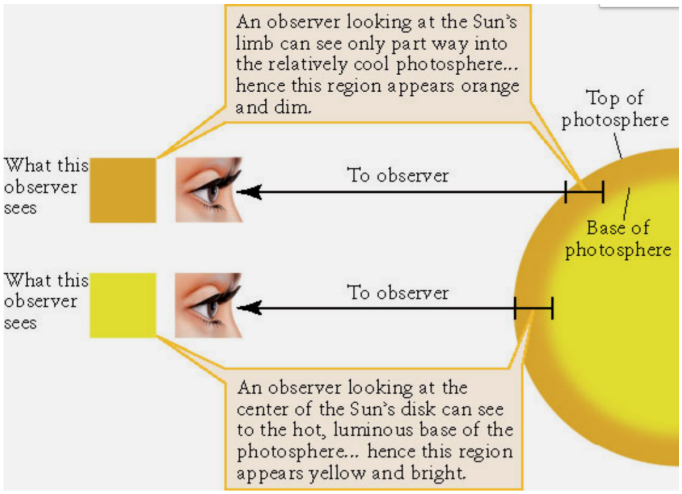

Figure 2.2: An illustration of limb darkening, from [43].

h, c, and k_B denote Planck's constant, the speed of light in vacuum and Boltzmann's constant. A few blackbody spectral radiance curves for the temperature range in the photosphere are depicted in Figure 2.3. It follows that, as the half-angle θ increases and accordingly temperature decreases, the spectrum loses intensity and is simultaneously redshifted. Limb darkening therefore implies that the spectral radiance observed on Earth depends on the origin of the ray, i.e. $\mathscr{L} = \mathscr{L}(\lambda, \theta)$.

Rays arriving at Earth at an opening half-angle $\theta = 0'$, i.e. aligned with the solar vector, correspond roughly to the $6400K$ spectrum. On the other hand, rays from the limb with $\theta = 16'$ correspond to the $4400K$ spectrum. Since an optical element like a mirror can only have one orientation, the optimal orientation always redirects rays from the centre of the Sun to the focal point. This implies that the relatively blueshifted $\theta = 0'$ ray intersects the focal plane at the focal point, yet the redshifted $\theta = 16'$ ray misses the focal point and intersects the focal plane at a different location. Exactly this phenomenon is illustrated in Figure 1.14, where the deviating red ray does not intersect the focal point. Generalising this result to all rays ending up at the focal plane, it follows that arriving rays are more blueshifted the closer they are to the focal point.

This phenomenon is clearly relevant for receivers placed at the focal plane, which will be subject to non-uniform irradiance as a fundamental consequence. The focal point receives blueshifted flux, and any other point in the focal plane receives progressively more redshifted flux the further it is distanced from the focal point. The described phenomenon is also relevant for designs with a secondary optical stage, as every secondary optical stage is fixed in orientation. As such, the most blueshifted ray from the centre of the Sun and the focal point is mapped according to design. However, the increasingly redshifted deviating rays that originated elsewhere do not arrive at the second stage properly, because they do not arrive from the focal point. After the secondary opti-

cal stage then, the deviation will be even more significant. This implies that blueshifted light is more likely to be propagated throughout the optical train than redshifted light.

It is important to note that it is therefore physically impossible to end up with an 'upscaled' version of the input spectrum after multiple optical stages, since the more blueshifted incident centre rays are more likely to end up at the receiver at a more perpendicular angle than redshifted limb rays. Finally, it should be noted that properties of optical stage elements themselves depend on angle of incidence. Section 3.3 expands upon the reflectance of a mirror, which is indeed a function of both incidence angle and wavelength. It is clear that, for every possible HCPV receiver design, angular exacerbation implies that both the angular and spectral properties of radiance must be considered in the analysis of every optical stage.

Summarising the argument, the radiance observed on Earth depends on both wavelength and opening half-angle due to limb darkening. Section 1.3.3 detailed how concentration of sunlight necessarily exacerbates angular deviations between incident rays. Optical properties of any optical train element also depend on both wavelength and incident angle. As a consequence, the flux after the primary optical stage is the result of an interaction effect between this exacerbation and the primary stage's optical properties. It then follows that both wavelength and incident angle must be considered for subsequent optical stages - including the receiver - in a high-concentration settings. Stated differently to contrast the HCPV setting with the conventional realm of flat-plate PV, high concentration invalidates the assumption of the Sun as a point source. As such, considering just spectral irradiance in an analysis is insufficient. For HCPV applications, the directional aspect of the flux matters too. Both the angular and wavelength dependence of the source radiance and optical train elements must therefore be considered.

2.3. EXPLORING THE SPECTRAL SUNSHAPE

Having established the importance of the spectral sunshape, the next step is estimating a functional form that can be used. There is unfortunately no reference spectral sunshape in existence, unlike how for example AM1.5D is a reference spectrum for DNI. However, several standards exist in the literature that are functionally equivalent to the spectral sunshape collapsed along one of the two dimensions. For example, recall that the AM1.5G and AM1.5D spectra are respectively defined as the spectral irradiance from the entire sky and from a 2.9° half-angle centred on the Sun. From the definition of spectral radiance in Equation (2.1), it follows that the AM1.5G and AM1.5D spectra are the spectral radiance integrated over a particular solid angle. The AM1.5G reference spectrum is simply the spectral radiance at an observer point integrated over the entire hemisphere:

$$AM1.5G(\lambda) = \frac{\partial E_{\odot,sky}}{\partial \lambda} = \int^{sky} \mathscr{L}_{ASTM}(\lambda,\Omega)\, d\Omega \tag{2.4}$$

Note that the integration is over solid angle $d\Omega$, which can be expressed in polar coordinates as $d\Omega = \sin(\theta)\, d\theta\, d\phi$. Compared to Equation (2.2), the term $\mathscr{L}_{\odot}(\lambda,\theta)$ referring to the Sun in general has been substituted by a term $\mathscr{L}_{ASTM}(\lambda,\theta)$ to stress that AM1.5D

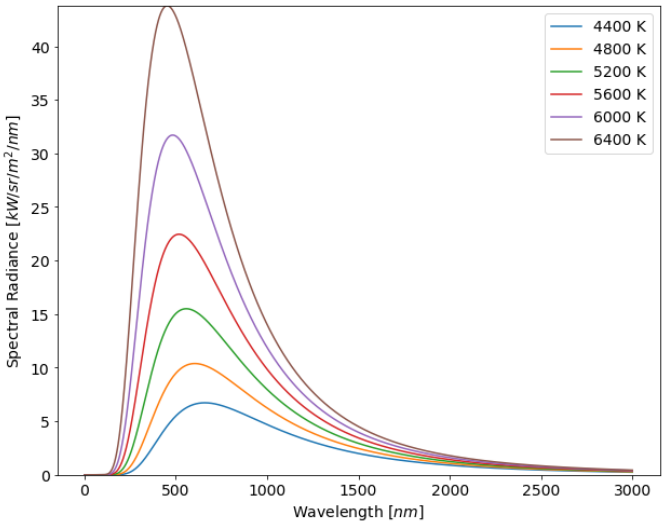

Figure 2.3: Black-body spectral radiance curves for selected temperatures within the photosphere's temperature range, from Equation (2.3)

.

is a particular estimate by the American Society of Testing and Materials. In a similar fashion, AM1.5D follows from integration of the same $\mathscr{L}_{ASTM}(\lambda,\theta)$ over a solid angle corresponding to a 2.9° half-angle centred on the Sun. Assuming azimuthal symmetry in $\theta = 0$, the integration over the azimuthal direction ϕ results in a factor 2π. This factor is however cancelled out by the half-angle counterpart definition in Equation (2.2), defined as such for notational convenience:

$$AM1.5D(\lambda) = \frac{\partial E_{\odot,2.9^\circ}}{\partial \lambda} = \int_0^{2.9^\circ} \mathscr{L}_{ASTM}(\lambda,\theta)\sin(\theta)d\theta \tag{2.5}$$

By integrating over the solid angles the two standard spectra are respectively defined by, the spectral sunshape $\mathscr{L}_{ASTM}(\lambda,\theta)$ collapses along the angular dimension to the familiar spectral irradiance in $[Wm^{-2}nm^{-1}]$. Of course, it is also possible to collapse the spectral radiance along its other dimension, i.e. the entire wavelength domain Λ. This results in a so-called sunshape profile [44]:

$$SS(\theta) = \int^{\Lambda} \mathscr{L}_{SS}(\lambda,\theta)d\lambda \tag{2.6}$$

The sunshape profile is a measure for the radiance derived from a particular opening half-angle, and has units $[SS(\theta)] = Wm^{-2}arcmin^{-1}$. The sunshape is the workhorse model in Concentrated Solar Power (CSP) system design, where solar concentration is used to generate a high heat flux. CSP systems utilise receivers that convert concentrated irradiance into heat effectively across the entire spectrum, i.e. the spectral response is rather uniform. As such, the information contained in a spectral profile is largely irrelevant for CSP purposes; what matters is the total irradiance that can effectively be

mapped to the receiver. As the previous section also indicated, this mapping from incident irradiance to receiver flux strongly depends on the source's angular profile and the optical train.

The sunshape that is effectively detected on Earth strongly depends on atmospheric conditions; several normalised sunshapes plotted by Blanc et al. [42] based on telescope measurements by Grether et al. [45] are depicted in Figure 2.4. The study of sunshape profiles is closely linked to the study of circumsolar radiation, i.e. radiation emanating from the solid angle just outside the angle subtended by the Sun, because this circumsolar radiation is typically at the border of being accessible for a CSP system.

Three main sunshape models are prevalent in the literature and software packages: the uniform sunshape, the Gaussian sunshape, and the Buie sunshape [41], in order of increasing complexity and accuracy. These three sunshapes are all particular forms of the sunshape $SS(\theta)$ as defined in Equation (2.6). Note that neither of these models distinguishes spectral information; all consider radiance as a function of opening half-angle only. There is no established standard sunshape analogous to how AM1.5D is a spectral irradiance standard, however the Buie sunshape is by far the most accurate sunshape profile that very accurately reproduces the data from Figure 2.4.

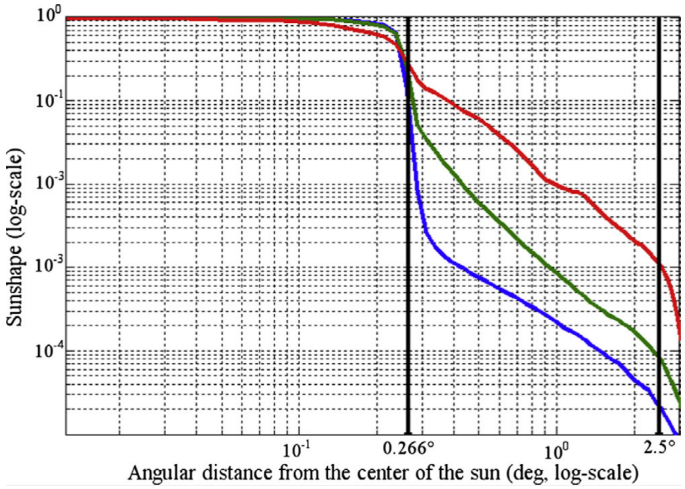

Figure 2.4: Three normalised sunshape profiles from LBNL circumsolar telescope data [45]. The leftern vertical black line indicates the edge of the solar disk, whilst the rightern indicates the opening angle of a typical pyrheliometer. half-angle of a typical pyrheliometer. The degree of scattering due to atmospheric parameters increases from the blue curve to the green curve to the red curve.

It is important to highlight that the workhorses in PV and CSP design - the spectral irradiance and the sunshape - are essentially simplified forms of the spectral radiance collapsed along one dimension. Both fields disregard information of one kind, as it is not relevant to the energy conversion strategy. Flat-plate PV features an energy conversion strategy with a specific spectral response, such that the spectral content of the irradiance is extremely important to consider. On the other hand, the half-angle between the so-

lar limb and the solar centre is negligibly small for ordinary PV systems, such that it is superfluous to consider irradiance as a function of opening half-angle. CSP features energy conversion strategies with a rather uniform spectral response, as the receiver simply converts all irradiance into heat regardless of wavelength. On the other hand, for CSP the irradiance per opening half-angle is a crucial design variable due to the fundamentals of concentration. It follows logically that CPV - which by definition features a specific spectral response as well as a concentrating optical train - should consider spectral radiance in its most extensive form.

The AM1.5G/AM1.5D solar spectra and the sunshape have been extensively scrutinised in the literature, and there is consensus within the respective fields of PV and CSP that they are adequately representative and accurate. As Equations (2.2), (2.4) and (2.5) demonstrate, the solar spectra and sunshape can be interpreted as the spectral sunshape integrated with respect to a particular variable. This suggests that it is a necessary condition for any candidate spectral sunshape representation to reproduce these reference AM1.5 spectra and the sunshape, upon substitution into the aforementioned equations. This requirement rings especially true for the AM1.5D spectrum, as it has been specifically established with concentrator appplications in mind. Stated differently, a candidate $\hat{\mathscr{L}}(\lambda,\theta)$ that does not adequately reproduce the AM1.5D spectrum when plugged into Equation 2.5 makes a poor candidate, since it will not hold up to the scrutiny the AM1.5D spectrum has faced over the years.

2.4. DERIVING AN ANALYTICAL FORMULATION

2.4.1. ASSUMPTIONS ON THE NATURE OF IRRADIANCE

In formulating an analytical spectral sunshape, it is instrumental to consider how the opening half-angle affects both the origin and the journey of a ray of light to an observer on Earth. Three characteristic solar regions can be identified: the solar disk from $\theta = 0$ up until $\theta \approx 0.266°$, the circumsolar region from $\theta \approx 0.266°$ to $\theta \approx 2.9°$, and finally the remaining sky $\theta \notin [0°, 2.9°]$. Rays within the solar disk are mostly unscattered photons which originate in the Sun's photosphere. There are also radiant solar layers exterior to the photosphere, such as the corona, which are evidently not as bright as the photosphere and only visible during a solar eclipse. Unscattered photons from these exterior layers contribute to the circumsolar radiation, and also a sizeable amount of photons scattered in either the Earth's atmosphere or the solar exterior layers. The radiance from the remaining sky consists of photons that are scattered in the Earth's atmosphere, amounting to the Diffuse Horizontal Irradiance (DHI). The solar disk and circumsolar region jointly constitute the DNI component. By decomposing the total radiance according to opening half-angle, an exhaustive piecewise spectral sunshape follows:

$$\mathscr{L}(\lambda,\theta) = \begin{cases} \mathscr{L}_1(\lambda,\theta), & \theta \in [0°, 0.266°) \\ \mathscr{L}_2(\lambda,\theta), & \theta \in [0.266°, 2.9°] \\ \mathscr{L}_3(\lambda,\theta), & \theta \notin [0°, 2.9°] \end{cases} \tag{2.7}$$

The three domains correspond to the half-angle regions discussed in the previous paragraph. $\mathscr{L}_1(\lambda,\theta)$ denotes radiance emanating from the solar disk, $\mathscr{L}_2(\lambda,\theta)$ from the

circumsolar region, and $\mathscr{L}_3(\lambda,\theta)$ is DHI. Reviewing Equations (2.4) and (2.5), it follows that $\mathscr{L}_1(\lambda,\theta)$ and $\mathscr{L}_2(\lambda,\theta)$ jointly constitute DNI as per AM1.5D, whilst GHI and the corresponding AM1.5G standard are comprised of all three exhaustive components.

It follows from the fundamentals of concentrating optics that the amount of irradiance available to a concentrator system depends on the extent of concentration. A non-concentrating system has access to all three radiance components of Equation (2.7), but the accessible radiance decreases as the concentration ratio is increased. Low-concentration systems quickly lose access to $\mathscr{L}_3(\lambda,\theta)$, and are therefore limited to DNI. For high-concentration systems the $\mathscr{L}_2(\lambda,\theta)$ component is partially unavailable, implying that such systems are even limited to a subset of DNI. The extent of the limitation of irradiance depends on the extent of concentration, and it is therefore important to characterise the distribution of DNI among its two components $\mathscr{L}_1(\lambda,\theta)$ and $\mathscr{L}_2(\lambda,\theta)$. This characterisation, also known as the circumsolar contribution to beam radiation, is a well-documented topic in the CSP literature [42].

Figure 2.4 suggests that the extent of scattering, and by extension the contribution of $\mathscr{L}_2(\lambda,\theta)$ relative to $\mathscr{L}_1(\lambda,\theta)$, strongly depends on atmospheric conditions. The atmospheric conditions assumed for the standard spectra AM1.5G and AM1.5D are tabulated in Table A.1. Note in particular that the standard spectra are defined by an Aerosol Optical Depth (AOD) of 0.084, which essentially corresponds to a very clear sky. The standard spectra are therefore consistent with the assumption of azimuthal spectral radiance symmetry. Figure 2.5 shows the circumsolar contribution to beam radiation as a function of wavelength, i.e. $CSC(\lambda)$. In the terminology of Equation 2.7, the $CSC(\lambda)$ is defined as follows:

$$CSC(\lambda) \overset{def}{=} \frac{\int_{0.266^\circ}^{2.9^\circ} \mathscr{L}_2(\lambda,\theta)d\theta}{\int_{0^\circ}^{0.266^\circ} \mathscr{L}_1(\lambda,\theta)d\theta} \tag{2.8}$$

Referring again to Figure 2.5, note that the blue line corresponds to an Aerosol Optical Depth (AOD) of 0.084, which is the value used for the ASTM standard spectra cited in Table A.1. It is shown that the contribution of $\mathscr{L}_2(\lambda,\theta)$ relative to $\mathscr{L}_1(\lambda,\theta)$ amounts to much less than 1% over almost the entire wavelength range. In other words, assuming the same conditions under which the reference spectra were generated, the contribution of $\mathscr{L}_2(\lambda,\theta)$ from Equation 2.7 is marginal. Furthermore, it was already mentioned earlier that the domain $\theta \notin [0^\circ, 2.9^\circ]$ is inaccessible for any HCPV system. It therefore follows that only the $\mathscr{L}_1(\lambda,\theta)$ component is generally relevant for HCPV systems.

It should be mentioned that it might be worthwhile to model $\mathscr{L}_2(\lambda,\theta)$ and even $\mathscr{L}_3(\lambda,\theta_f)$ for LCPV applications, where a wider range of opening half-angles reaches the receiver due to the lower concentration. Additionally, quantification of $\mathscr{L}_1(\lambda,\theta)$ under conditions other than a clear sky would also be insightful for a complete HCPV system analysis. These topics however elude the scope of this thesis, which will focus on $\mathscr{L}_1(\lambda,\theta)$ under clear sky conditions. This focus is motivated by the emphasis on HCPV, and also by the fact that the vast majority of incident solar flux will come from this component. The next step is developing a model for the $\mathscr{L}_1(\lambda,\theta)$ component.

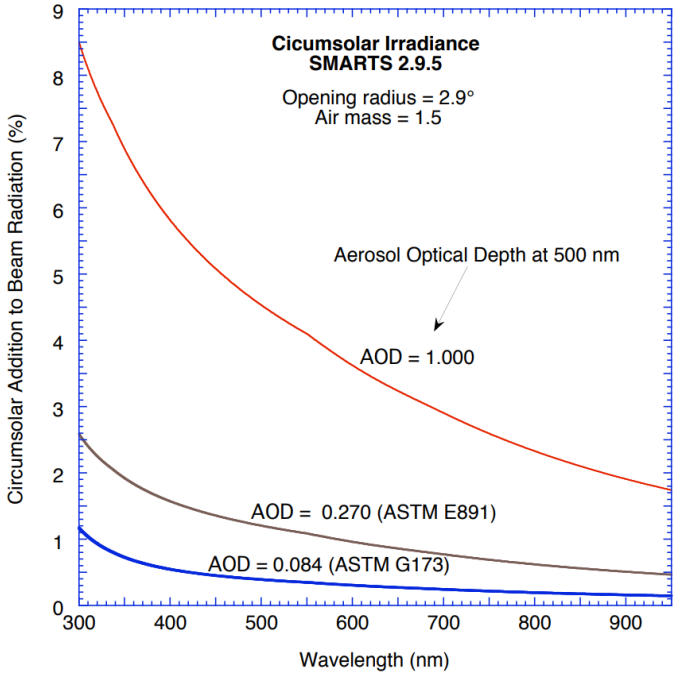

Figure 2.5: The total circumsolar contribution $CSC(\lambda) \overset{def}{=} \frac{\int_{0.266°}^{2.9°} \mathscr{L}_2(\lambda,\theta)d\theta}{\int_{0°}^{0.266°} \mathscr{L}_1(\lambda,\theta)d\theta}$ for three Aerosol Optical Depth (AOD) values, computed with SMARTS. The blue curve represents the AOD that is incorporated into the AM1.5D standard, and implies an insignificant contribution of $_2(\lambda,\theta)$ to total irradiance. Reprinted from [20]

.

2.4.2. INCORPORATING A LIMB DARKENING MODEL

Having established the scope of analysis, let us analyse the radiance $\mathscr{L}_1(\lambda,\theta)$ originating within the solid angle subtended by the solar disk in more detail. Three subsets of rays jointly constitute this radiance: photons emitted by the Sun passing through both the Sun's and Earth's atmospheres, photons scattered in the solar atmosphere that pass through the Earth's atmosphere, and finally photons that scatter in Earth's atmosphere. In practice, both scattered sets of photons represent an insignificant contribution to the photon flux within this limited solid angle [42]. For the non-scattered photon flux, limb darkening - as introduced in Figures 2.1 and 2.2 - is the dominant phenomenon that affects the spectral sunshape. Limb darkening observations of the Sun have been made by instruments on Earth, and the most straightforward spectral sunshape candidate would be a functional form in both λ and θ agreeing with these observations.

Pierce and Slaughter [46] and Pierce et al. [47] fitted polynomials, labelled PS(W), in the opening half-angle to various sets of intensity observations. Every set of observations is made at a particular wavelength in the broadband spectrum, corresponding to the telescope filter used. Neckel and Labs [48] fitted similar polynomials, labelled NL, to 30 sets of observations in the $[303nm, 1099nm]$ range. The PS(W) and NL data were all observed using the McMath-Pierce solar telescope at Kitt Peak National Observatory in Arizona, USA. That is, these observations also boast the advantage that any possible effects between the origin of the photons and their arrival at the McMath-Pierce solar telescope have also been accounted for; a suitable spectral sunshape model for terrestrial applications should also account for these. In the terminology of this thesis, the PS(W) and NL polynomials are essentially estimates of $\mathscr{L}_1(\lambda,\theta)$ for particular values of λ, i.e. $\hat{\mathscr{L}}_1(\bar{\lambda},\theta)$. A hat superscript indicates an estimate, whilst a bar superscript denotes a particular value.

To arrive at $\mathscr{L}_1(\lambda,\theta)$, it is necessary to fit a functional form in λ as well. Neckel demonstrated that limb darkening is smooth in wavelength, i.e. interpolation of the particular $\bar{\lambda}$ values at which the PS(W) and NL observations were made is feasible [49]. The only exception is in the neighbourhood of the Balmer jump, around $364.6nm$. Hestroffer and Magnan postulated the following parsimonious empirical law for relative intensity as a function of wavelength and opening half-angle [50]:

$$\frac{\mathscr{L}_{HM}(\lambda,\theta)}{\mathscr{L}_{HM}(\lambda,0)} = 1 - u(1-\mu(\theta)^{\alpha(\lambda)}) \tag{2.9}$$

$$\mu(\theta) = \sqrt{1 - \frac{\sin^2(\theta)}{\sin^2(16')}}, \qquad \theta \in [0', 16'] \tag{2.10}$$

$$\alpha(\lambda) = \begin{cases} -0.507 + 441\lambda^{-1}nm, & \lambda \in [303.327nm, 349.949nm] \\ \alpha_{Balmer}, & \lambda \in (349.949nm, 416.320nm) \\ -0.023 + 292\lambda^{-1}nm, & \lambda \in [416.320nm, 2401.800nm] \end{cases} \tag{2.11}$$

In Equation (2.9), $\mathscr{L}_{HM}(\lambda,0)$ denotes the spectrum at the centre of the Sun. The function $\mu(\theta)$ appearing in Equation (2.9) is the conventional representation of opening

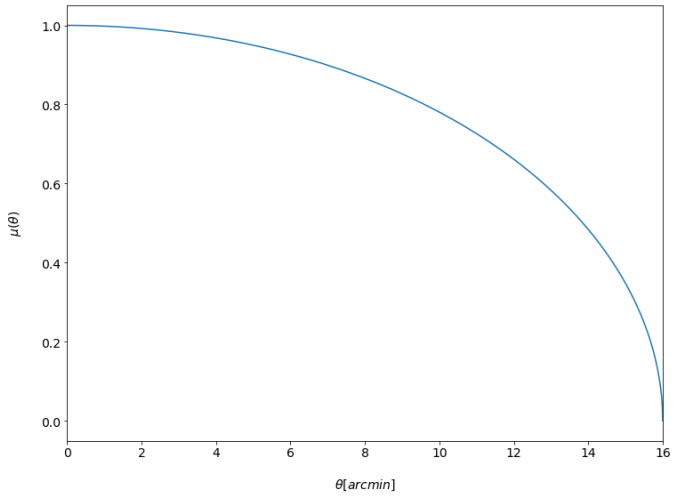

Figure 2.6: The function $\mu(\theta)$ as defined in Equation (2.10) depicted over its entire domain.

half-angle in stellar limb darkening literature; it is related to the opening half-angle θ employed thus far by Equation (2.10). It is used in the stellar limb darkening literature for its numerical convenience, beacuse it assumes a value between 0 and 1; 0 for $\theta = 16'$, i.e. at the limb, and 1 for $\theta = 0'$, i.e. at the centre of the Sun. The function $\mu(\theta)$ is plotted over the limb domain $\theta \in [0', 16']$ in Figure 2.6.

The factor u in Equation (2.9) is a dampening factor, and it follows from the $[0,1$ range of $\mu(\theta)$ that $1-u$ equals the ratio of intensity at the limb to intensity at the centre. $\alpha(\lambda)$ represents the wavelength-dependent limb darkening, and also assumes a value between 0 and 1. The piece-wise function in Equation (2.11) follows from fitting the model to the PS(W) and NL observational data for $u = 0.85$. $\alpha(\lambda)$ as a function of wavelength from Equation (2.11) is depicted in Figure 2.7, in which α_{Balmer} is a cubic spline interpolation of the 14 particular values from this region that were tabulated in the Hestroffer Magnan paper.

This model agrees with the data within ±1% for a radius up to 0.9 times the solar radius [50]. Beyond this point the deviation increases as the edge of the solar disk is approached, but remains within ±10%. The vast majority of the solar radiance stems from the region with excellent agreement, such that the parsimonious Equation (2.9) is a suitable building block for a spectral sunshape model. A more elaborate treatise on the agreement with the PS(W) and NL observational data is included in the original article by Hestroffer and Magnan. The analytical form of the Hestroffer-Magnan model is convenient for the analytical approach in this thesis, but it is recognised that the original observational data themselves would constitute a more accurate estimate.

2.4.3. THE ESTIMATED SPECTRAL SUNSHAPE

The right-hand side of Equation (2.9) has been defined, but an unknown quantity still appears on the left-hand side: $\mathscr{L}_{HM}(\lambda, 0)$, the spectrum at the very heart of the Sun. No

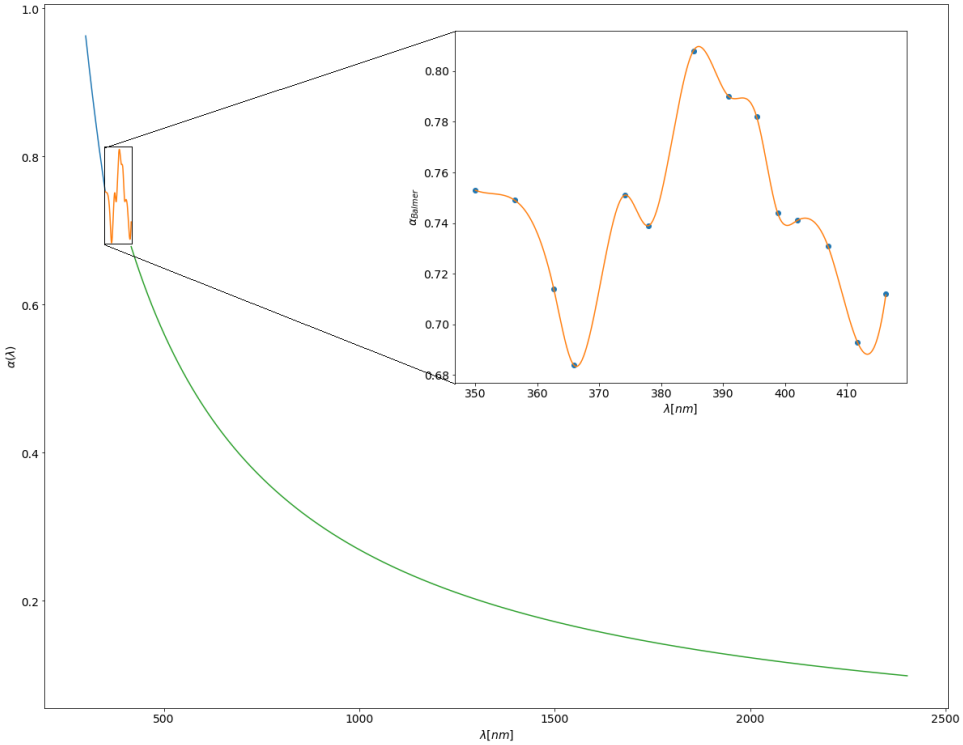

Figure 2.7: $\alpha(\lambda)$ as defined in Equation (2.11). The inset shows the second region α_{Balmer}, for which a cubic spline interpolation is invoked in the absence of data. A significant and a small jump respectively exist at the boundaries $349.949nm$ and $416.320nm$.

established standard spectrum exists, but it is possible to estimate it based on a standard that does exist: the AM1.5D spectrum. Note that Equation (2.9) holds for every wavelength, and that AM1.5D standard defines the spectral irradiance from the entire opening half-angle range as per Equation (2.5). Since $\mathscr{L}_{HM}(\lambda,0)$ by definition does not depend on opening half-angle, it is possible to calculate $\mathscr{L}_{HM}(\lambda,0)$ through combining Equations (2.5) and (2.9) and substituting the wavelength-dependent limb darkening function. One problem remains: the domains do not match. The AM1.5D spectrum is defined corresponding to a 2.9° half-angle, i.e. it includes both $\mathscr{L}_1(\lambda,\theta)$ and $\mathscr{L}_2(\lambda,\theta)$. The limb darkening observations only hold for the solar disk, and thus only correspond to $\mathscr{L}_1(\lambda,\theta)$. As such, it is necessary to correct for the contribution of $\mathscr{L}_2(\lambda,\theta)$. This correction is done through the $CSC(\lambda)$ from Equation (2.8), depicted in Figure 2.5. Since the raw data are unavailable, the relevant blue line corresponding to $AOD = 0.084$ is approximated as follows:

$$C\hat{S}C(\lambda) \approx 450\lambda^{-1.854} \tag{2.12}$$

The original Figure only depicts the $[300nm, 900nm]$ range, which does not span the AM1.5D domain of $[303.327nm, 2401.800nm]$. Since the $CSC(\lambda)$ is a decreasing function of wavelength, and since the value at $900nm$ is already rather small and insignificant, the approximation in Equation (2.12) is extended to the entire domain. The resulting $C\hat{S}C(\lambda)$ is depicted in Figure 2.8.

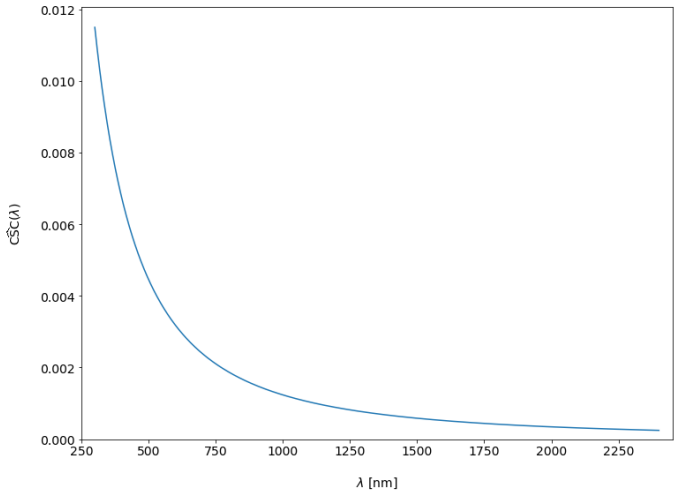

Figure 2.8: The approximation of the circumsolar contribution as a function of wavelength as defined in Equation (2.12) over the wavelength range considered. Note that the approximation closely agrees with the $AOD = 0.084$ circumsolar contribution depicted in Figure 2.5.

Substituting (2.9) for $\mathscr{L}_{ASTM}(\lambda,\theta)$ in the AM1.5D Equation (2.5), and including the correction factor $(1 + C\hat{S}C(\lambda))$ defined in Equation (2.12), it follows that:

$$\frac{AM1.5D(\lambda)}{(1+C\hat{S}C(\lambda))} = 2\pi \int_{0'}^{16'} \mathscr{L}_{HM}(\lambda,0)\left(0.15+0.85\mu(\theta)^{\alpha(\lambda)}\right)\sin(\theta)d\theta \tag{2.13}$$

Again, since the spectral sunshape at the centre of the solar disk $\mathscr{L}_{HM}(\lambda,0)$ is independent of θ, it can simply be taken outside of the integral. Define the estimator for the spectral sunshape at the centre of the solar disk based on the Hestroffer-Magnan limb darkening model to be $\hat{\mathscr{L}}_{HM}(\lambda,0)$:

$$\hat{\mathscr{L}}_{HM}(\lambda,0) = \frac{AM1.5D(\lambda)}{\left(1+C\hat{S}C(\lambda)\right) * 2\pi \int_0^{'16'} (0.15+0.85\mu(\theta)^{\alpha(\lambda)})\sin(\theta)d\theta} \tag{2.14}$$

It is important to note that the AM1.5D standard spectrum is defined for a wavelength domain $\lambda \in [280nm, 4000nm]$ whereas the Hestroffer Magnan limb darkening function is only defined for the domain $\lambda \in [303.327nm, 2401.800nm]$. As such, only this subset of the AM1.5D spectrum is considered. This limitation does not jeopardise a HCPV conversion efficiency analysis however, because the excluded regions are largely irrelevant. The $[280nm, 303.327nm]$ domain corresponds to less than $0.001Wm^{-2}$, and is therefore insignificant. The $[2401.800nm, 4000nm]$ interval contains approximately $10Wm^{-2}$, but even with multi-junction solutions this entire interval is inaccessible. $2401.8nm$ corresponds to a band gap energy of $0.5162eV$, well below the band gaps of the lowest band gap semiconductors used in multi-junction cells. That is, the $10Wm^{-2}$ contained in the $[2401.800nm, 4000nm]$ interval will in practice always be thermalised and thus lost in the form of heat. However, considering the necessity of meticulous thermal management in case of HCPV, this $10Wm^{-2}$ must be taken into account as additional heat flux on the receiver.

Finally, the spectral sunshape $\mathscr{L}(\lambda,\theta)$ can be estimated by substituting the estimator from Equation (2.14) into Equation (2.9). The estimated spectral sunshape based on the Hestroffer-Magnan limb darkening model $\hat{\mathscr{L}}_{HM}(\lambda,\theta)$ follows. All right-hand side terms in Equations (2.10), (2.11) and (2.14) have been fully identified:

$$\hat{\mathscr{L}}_{HM}(\lambda,\theta) = \hat{\mathscr{L}}_{HM}(\lambda,0)\left(0.15+0.85\mu(\theta)^{\alpha(\lambda)}\right) \tag{2.15}$$

It should be noted that this spectral limb darkening characterisation pertains to the Sun itself, and is independent of perturbations - such as atmospheric attenuation - induced by the journey from the Sun to an observer on Earth. The limb darkening observations, from which the Hestroffer-Magnan model is derived, have been carefully purified to remove such perturbations. It is very reasonable to assume that such perturbations are independent of the half-angle θ, because attenuation during the optical journey through space and the Earth's atmosphere is unlikely to significantly differ for small θ variations.
This independence then implies that the bracketed term in Equation (2.15) fully captures the spectral limb darkening phenomenon. The term $\hat{\mathscr{L}}_{HM}(\lambda,0)$ in Equation (2.15) on the other hand represents the AM1.5D irradiance conditions - as is evident from Equation (2.14) - and these include wavelength-dependent atmospheric attenuation. It follows that it is rather simple to extend this model to terrestrial locations for which the AM1.5D spectrum might not be representative, such as a location with an Air Mass 2 optical journey. The AM1.5D-specific $\hat{\mathscr{L}}_{HM}(\lambda,0)$ term can simply be replaced by a different baseline $\hat{\mathscr{L}}(\lambda,0)$. This baseline can be obtained by replacing the term $AM1.5D(\lambda)$ in Equation

(2.13), such as the AM2 spectrum in the example at hand. The algorithm then yields a spectral radiance profile akin to (2.15) for the alternative location of interest.

The goal of this subsection has now been attained: the spectral sunshape in Equation (2.15) has been estimated by inverting the AM1.5D spectrum based on the Hestroffer-Magnan solar limb darkening model. A 3D plot of $\hat{\mathscr{L}}_{HM}(\lambda,\theta)$ in both its arguments is depicted in Figure 2.9. This spectral sunshape representation meets the necessary condition of reproducing the AM1.5D spectrum (recall Subsection 2.3) by construction. Importantly, Equation (2.15) can be incorporated into the geometrical optics equations from the previous section to assign magnitudes to rays, so as to evaluate the radiative transfer.

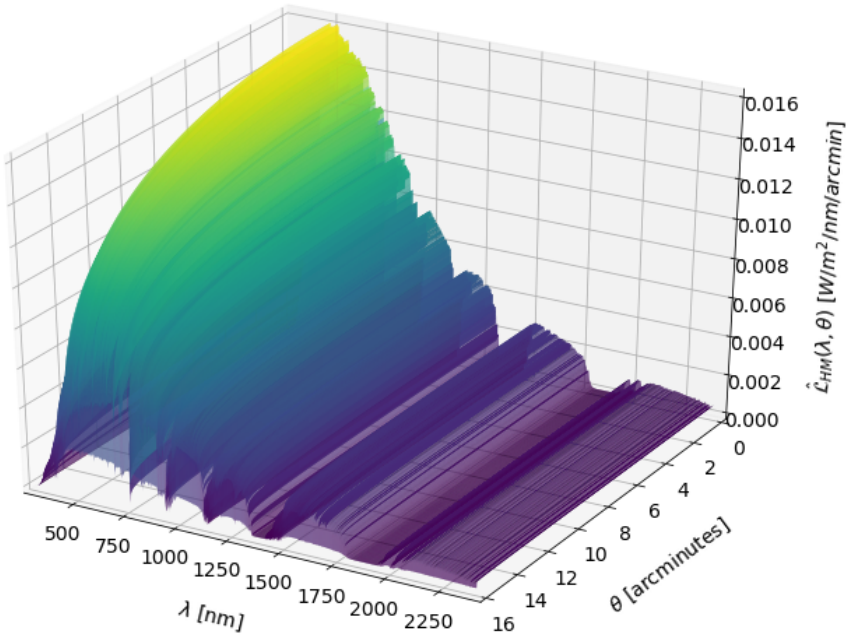

Figure 2.9: A 3D plot of the estimated spectral sunshape in both its arguments λ and θ. The half-angle domain depicted spans the entire solar limb.

2.5. SPECTRAL SUNSHAPE PROPERTIES

This section considers the spectral sunshape's properties in detail, and in particular their implications for HCPV system analyses. First and foremost, consider the units of the spectral sunshape: $[Wm^{-2}nm^{-1}arcmin^{-1}]$. Recalling that radiance - or irradiance over solid angle - has units $[Wm^{-2}sr^{-1}]$, and that spectral irradiance - or irradiance over wavelength - has units $[Wm^{-2}nm^{-1}]$, it follows that this spectral sunshape is essentially

a combination of both: irradiance as a function of both solid angle and wavelength. In this analogy, it is important to clarify that the spectral sunshape has opening half-angle θ as an argument rather than solid angle ω. The reason is that azimuthal symmetry of the Sun in its centre was assumed, i.e. in the line corresponding to $\theta = 0°$. Half-angle dependence rather than solid angle dependence also greatly aids in the intuitive visualisation of the spectral sunshape. The switch to arcminutes as opening half-angle measure was motivated by the notational convenience of the solar limb extending to $16.0'$. The scale is of course arbitrary, and the half-angle domain could easily be transformed into $[0°, 0.266°]$ or a measure in radians.

Now, since the spectral sunshape depicted in Figure 2.9 is an extension of the AM1.5D spectrum, it is equal to the AM1.5D spectrum if collapsed along the half-angle dimension. The total spectral irradiance contained in the AM1.5D spectrum, i.e. the integral over its entire wavelength domain $[280nm, 4000nm]$, amounts to $900.1 Wm^{-2}$. However, recall that the limb darkening model was only available for the $[303.327nm, 2401.800nm]$ subdomain. The AM1.5D spectrum amounts to $890.0 Wm^{-2}$ in this subdomain, omitting the $10 Wm^{-2}$ contained in the $[280nm, 300nm]$ interval and the negligible spectral irradiance corresponding to the $2401.800nm, 4000nm]$ interval.

Integrating the depicted spectral sunshape over both its domains results in an integral of $141.3 Wm^{-2}$. After integrating over the azimuthal direction as well - equivalent to multiplication by the factor 2π due to azimuthal symmetry - this amounts to $887.7 Wm^{-2}$. The difference between this number and the total AM1.5D amount of $890 Wm^{-2}$ follows from the circumsolar contribution correction factor apparent in Equation (2.13). As such, the spectral sunshape has been constructed in a valid manner. To reiterate, this $887.7 Wm^{-2}$ is the total irradiance contributed by the $\mathscr{L}_1(\lambda, \theta)$ component in Equation (2.7), or the radiance originating in the solid angle subtended by the Sun. The spectral sunshape peaks at the solar vector $\theta = 0'$, and at the same $\lambda = 531nm$ wavelength where the AM1.5D spectrum peaks. The peak spectral radiance value is 0.0160 $[Wm^{-2}nm^{-1}arcmin^{-1}]$

2.5.1. COMPARING THE DERIVED SPECTRA AT PARTICULAR OPENING HALF-ANGLES

Figure 2.10 shows the spectral radiance per opening half-angle for selected wavelengths. The profiles follow from substitution of the corresponding wavelength for λ in Equation (2.15), and are thus slices of Figure 2.9. Figure 2.10 essentially displays Equation (2.15) over the opening half-angle domain. Apparent are the more significant limb darkening for shorter wavelengths as well as the wavelength-dependent starting points $\hat{\mathscr{L}}_{HM}(\lambda, 0)$ from Equations (2.9) through (2.7).

Additionally, spectral radiance profiles for four particular opening half-angles, including $\hat{\mathscr{L}}_{HM}(\lambda, 0)$, are depicted in Figure 2.11. The profiles in turn follow from substitution of the corresponding particular half-angle for θ_i in Equation (2.15). The profiles are redshifted and smaller in magnitude as θ_i increases, which again corresponds to the

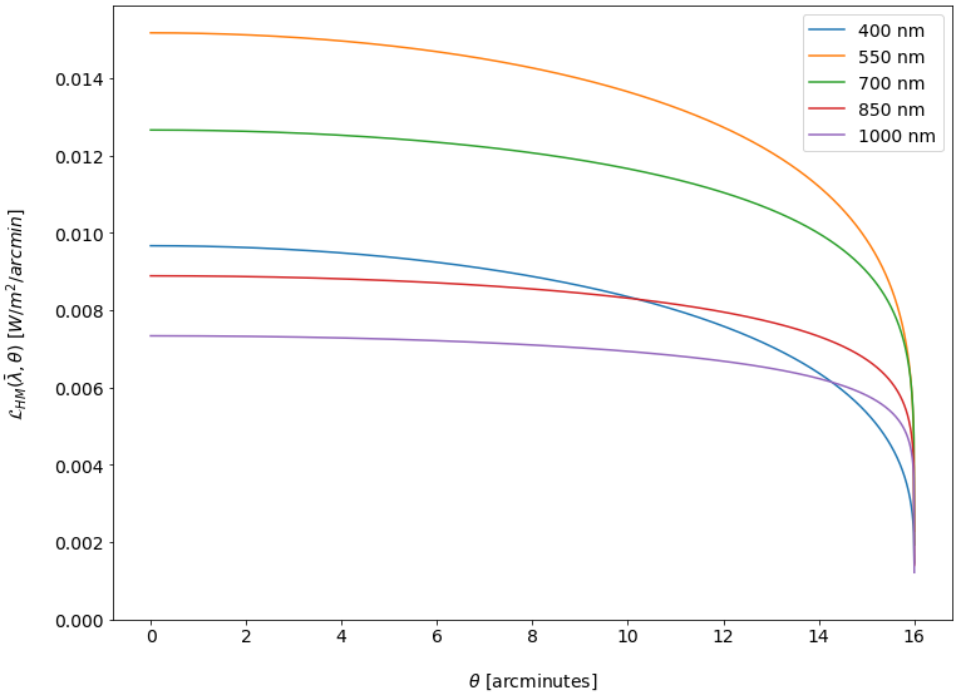

Figure 2.10: The derived intensity over opening half-angle for five particular values of λ : $400nm, 550nm, 700nm, 850nm$ and $1000nm$. These limb darkening functions are slices of the spectral sunshape depicted in Figure 2.9.

limb darkening phenomenon of a redder, dimmer Sun near the edges. The profiles are consistent with the trend visible in Figure 2.3, which mapped the blackbody spectral radiance curves for selected temperatures. Again, these profiles imply that the focal point receives the most blueshifted and most intense spectrum, and that other points in the focal plane at height F receive a more redshifted and less intense spectrum as the radial distance increases.

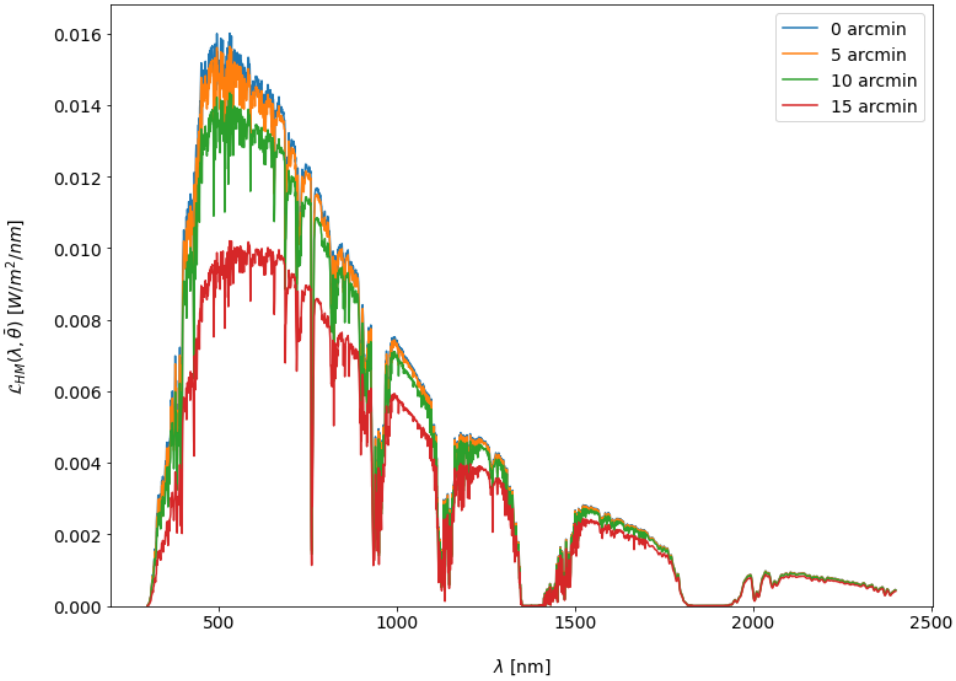

Figure 2.11: The derived spectra for four particular values of $\theta : 0', 5', 10'$ & $15'$. These spectra are slices of the spectral sunshape depicted in Figure 2.9.

A few properties apparent in these slices are very relevant for spectrally selective energy conversion strategies such as solar cells. Firstly, it is implied that the radiance received by the focal plane is nonuniform. Consider again the illustration of angular exacerbation in Figure 1.14. Assuming that the perfect, green lines in that illustration correspond to the heart of the Sun $(\theta) = 0°$, it is implied that more energy corresponding to $400nm$ than corresponding to $850nm$ arrives at F. However, if the red line indicated deviates by more than $\theta) = 10°$, then the point at the same height as F which the red line crosses receives more energy corresponding to $850nm$ than to $400nm$. Incident radiance thus inherently depends on distance from the focal point. It should be stressed that this holds even in case of a perfectly specular optical train, as it is a property of the source.

A second important property that should be considered is that the spectrum post-concentration will necessarily differ from the spectrum pre-concentration. As such, the

concentrated spectral irradiance at any receiver will necessarily deviate from a more intense, upscaled AM1.5D spectrum. It should be emphasised that this effect, where rays are more redshifted the further one deviates from the focal point, does not just apply for the AM1.5D case. The effect derives from the bracketed term in Equation (2.15), and as the previous paragraph explained it thus holds globally.

This inevitable consequence of concentration is important, because state-of-the-art multi-junction (MJ) cell designs do assume a scaled AM1.5D spectrum **??**. In fact, the ASTM standard for testing solar cells under concentration prescribes a scaled-up AM1.5D spectrum **??**. Recall that stacked MJ cells are generally connected in series, such that an underperforming junction will current-limit the other junctions' current output. This necessitates careful tuning of each junction's thickness etc. to minimise the discrepancy between the individual junction currents. Clearly, the individual currents depend on the incident spectrum. If MJ cells are designed assuming a scaled AM1.5D spectrum, whilst they would inevitably not be subjected to a scaled AM1.5D spectrum in any realistic HCPV setup, it follows that such cells are essentially current-limited by design. Instead of designing MJ cells assuming scaled AM1.5D, the actual spectral irradiance incident on the cell must be calculated by mapping a representative spectral radiance profile through an optical train. Chapter 3 will delve deeper into this problem.

For the other candidate HCPV receiver introduced earlier, the spectral beam splitter configuration which defers subsets of the spectrum to different specialised photovoltaic cells, the effect is also significant. Although the current matching problem is circumvented altogether, another problem arises due to the coupled dependence on incidence angle and wavelength. A beam splitting optical filter such as a dielectric stack functions optimally when the incidence angle is 45°. Post concentration, a significant share of the concentrated beam will necessarily be incident at a different angle of incidence. The crux is that the deviation in angle of incidence correlates with redshift. A ray ray from the centre of the Sun is properly propagated throughout the optical train, such that it arrives at the intended incidence angle of 45°. On the other hand, relatively redshifted light from the limb arrives at a different incident angle. The higher the concentration, the more significant this effect becomes.

In conclusion, the spectral sunshape implies that the irradiance at the focal plane depends on distance from the focal point due to the nature of the Sun. This implication maches the intuitive prediction outlined in Section 2.2. It is therefore problematic to design a HCPV energy conversion receiver by simply assuming an upscaled AM1.5D spectrum as the incident irradiance profile. This finding is important, because the literature on HCPV receivers does generally make this assumption. In case of multi-junction tandem cell design for example, current matching is the goal attained by carefully designing the individual subcells. This calculation requires a spectral irradiance profile as the input, and if the spectral irradiance profile is incorrect of course the current matching problem will not be solved adequately. In HCPV receiver design, the actual spectral irradiance incident on the receiver should be calculated by mapping a spectral sunshape estimate - such as the one developed here - through a specified optical train. Chapter 3

will delve deeper into this problem, and present a generalised method to perform exactly this mapping for a heliostat.

2.5.2. COMPARING WITH EXISTING SUNSHAPE MODELS

This section compares the derived spectral sunshape to existing sunshape models, so as to quantify the improvement of considering the spectral information. Three main sunshape models are prevalent in the literature and software packages: the uniform sunshape, the Gaussian sunshape, and the Buie sunshape [41]. These three sunshapes are all particular forms of the sunshape $SS(\theta)$ as defined in Equation (2.6). Note that neither of these models distinguishes spectral information; all consider radiance as a function of opening half-angle only. The sunshapes are therefore not formulated as spectral radiance profiles, but for every single one of them a unique corresponding spectral radiance function is identified according to Equation (2.6).

A sunshape i is typically expressed in the form $SS_i(\theta) = I_i * limb_i(\theta)$, where I_i represents the intensity at the Sun's centre and $limb_i$ represents the so-called limb function, which assumes a value between 0 and 1(at the centre). The limb function therefore represents the intensity at a particular opening half-angle θ relative to the intensity at the centre. It should be noted that this section will only compare the sunshapes as defined for the $[0', 16']$ opening half-angle domain, corresponding to $\mathscr{L}_1(\lambda, \theta)$ from Equation (2.7). Restriction to the $[0', 16']$ domain is done through the indicator function $\mathbb{1}(\theta < 16')$, which assumes a value of 1 for $\theta < 16'$ and 0 elsewhere. As such, every sunshape restricted to the $[0', 16']$ domain can be expressed as $SS_i(\theta) = I_i * limb_i(\theta) * \mathbb{1}(\theta < 16')$

It should be noted that the opening half-angle dependence of every sunshape is entirely captured in the limb function term; the intensity at the centre is independent of θ. By construction, every sunshape is required to amount to the total irradiance of $887.7 W m^{-2}$ upon integration over the opening half-angle domain. Since integrals of particular limb functions over the opening half-angle domain are not necessarily the same, it follows that the intensity at the Sun's centre will renormalise to satisfy the correct total irradiance amount. That is, since the total irradiance is conserved, a different limb intensity at the centre is implied for limb functions with a different integral over the half-angle domain.

The uniform or 'pillbox' sunshape is the simplest, and the first step in considering the Sun as an extended source. It is simply assumed that the Sun is equally bright regardless of the opening half-angle, i.e. the intensity is $I_{uniform}$ for the entire half-angle domain. The pillbox sunshape is expressed in Equation (2.16) and shown in the accompanying figure 2.5.2. It should be noted that, in a ray-tracing setting, the uniform sunshape is implicitly assumed if one randomly samples vectors from the solid angle subtended by the Sun without applying weights. This is a commonly used approach because of the computational simplicity; often, directional vectors are traced throughout a topology without assigning weights or magnitudes to the vectors. The uniform sunshape is therefore the default implicit sunshape, and rather common.

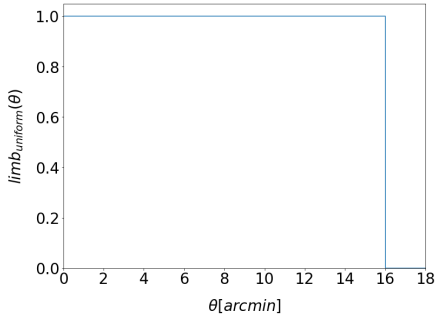

$$
\begin{aligned}
SS_{uniform}(\theta) &= I_{uniform} * limb_{uniform} \\
&= I_{uniform} * \mathbb{1}(\theta < 16') \\
SS_{Buie}(\theta) &= I_{Buie} * limb_{Buie}(\theta) \\
&= I_{Buie} * \frac{cos(0.326\theta)}{cos(0.306\theta)} * \mathbb{1}(\theta < 16')
\end{aligned}
\tag{2.16}
$$

The second commonly invoked sunshape is the Gaussian sunshape. The limb function assumes the form of the half-domain Gaussian function, as defined in Equation (2.17) and visualised in the accompanying figure. The Gaussian limb function has a single parameter, the standard deviation σ, which was set to $2.73mrad$ in this case. This number is also the standard deviation implemented in SolTrace, a software package used to assess CSP systems. The result of this particular value is a limb function with a Gaussian shape, declining from 1.00 at $\theta = 0'$ to 0.234 at $\theta = 16'$. The Gaussian sunshape is popular because it is easily integrated with typical optical error models. As the next Chapter 3 will document, the aggregate optical error tends to a Gaussian distribution too. For now, it suffices to say that the method to calculate the result of a spectral radiance function interacting with an optical surface is through a mathematical convolution. The convolution of a Gaussian with another Gaussian is yet another Gaussian, which is very convenient from a computational point of view. As such, the Gaussian sunshape is often implemented in analyses where the optical error of the optical train is also considered.

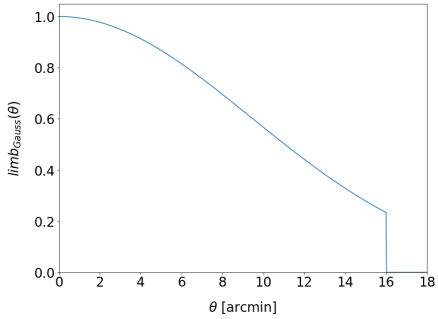

$$
\begin{aligned}
SS_{Gauss}(\theta) &= I_{Gauss} * limb_{Gauss}(\theta) \\
&= I_{Gauss} * e^{\frac{-\sigma^2}{2}} * \mathbb{1}(\theta < 16')
\end{aligned}
\tag{2.17}
$$

The final and most accurate sunshape profile is referred to as the Buie sunshape. Buie constructed the Equation in (2.18) to closely fit actual observations of the Sun obtained by the LBNL circumsolar telescope, the very same telescope that yielded the three sunshape profiles in Figure 2.4 [41]. The Buie sunshape is the state of the art sunshape used in thorough CSP analyses. This limb function declines to a value of 0.391 at $\theta = 16'$. Since it is a trigonometric function, it is more computationally intensive to convolve the Buie sunshape with a Gaussian aggregate optical error model. The complexity increases as more optical stages are added, such that the Gaussian sunshape might be preferable for such systems.

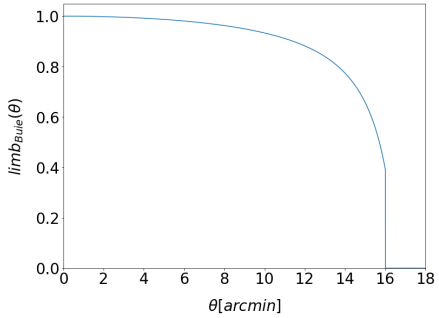

$$SS_{Buie}(\theta) = I_{Buie} * limb_{Buie}(\theta) = I_{Buie} * \frac{cos(0.326 * \theta_{rad})}{cos(0.306 * \theta_{rad})} * \mathbb{1}(\theta < 16') \tag{2.18}$$

Now, note that any sunshape specification should represent the exact same amount of solar flux: the total. Note also that the sunshape has no spectral information by definition, which implies the separation of spectral radiance into sunshape $SS(\theta)$ and a spectral component $\mathscr{W}(\lambda)$ expressed in Equation (2.19).

$$\mathscr{L}_{SS}(\lambda,\theta) = \mathscr{W}(\lambda) * SS(\theta) \tag{2.19}$$

It then follows that a unique spectral sunshape formulation $\hat{\mathscr{L}}_{SS,i}(\lambda,\theta)$ is identified for every single sunshape specification i. That is, for all three aforementioned sunshapes the integral over the opening half-angle subtended by the Sun equals the total irradiance. The corresponding spectral radiance functions $\hat{\mathscr{L}}_{SS,i}(\lambda,\theta$ is identified in Equation (2.20) by inverting the AM1.5D spectrum, much in the same vein as Equation (2.13). Recall that the spectral sunshape only pertains to the spectral radiance component $\mathscr{L}_1(\lambda,\theta)$ from the Sun's solid angle, such that the same circumsolar contribution correction $\frac{1}{1+C\hat{S}C(\lambda)}$ is applied.

$$\frac{AM1.5D(\lambda)}{(1+C\hat{S}C(\lambda))} = 2\pi \int_{0'}^{16'} \mathscr{W}_i(\lambda) * SS_i(\theta)\sin(\theta)d\theta \tag{2.20}$$

Again the spectral sunshape formulation must account for the AM1.5D spectrum at every wavelength, and there is only a single wavelength-dependent term on the right-hand side due to the separation of variables in Equation (2.19). The implicit spectral component $\mathscr{W}_i(\lambda)$ is thus identified for every sunshape i:

$$\mathscr{W}_i(\lambda) = \frac{AM1.5D(\lambda)}{\left(1+C\hat{S}C(\lambda)\right) * 2\pi \int_0^{16'} SS_i(\theta)\sin(\theta)d\theta} \tag{2.21}$$

The unique spectral sunshape corresponding to every ordinary sunshape can now be constructed using Equation (2.19), and the resulting spectral sunshapes are all shown in Figure 2.12. For all spectral sunshapes, the integral over both arguments amounts to $887.7 Wm^{-2}$, the total irradiance contained in the AM1.5D spectrum excluding the circumsolar correction. The uniform spectral sunshape $\hat{\mathscr{L}}_{uniform}(\lambda,\theta)$ - derived from the uniform sunshape - is depicted in the upper left of Figure 2.12. It is simply a rescaled three-dimensional extrusion of the AM1.5D spectrum, and does not take any limb darkening into account. The upper right shows the Gaussian spectral sunshape $\hat{\mathscr{L}}_{Gauss}(\lambda,\theta)$ corresponding to the Gaussian sunshape defined by Equation (2.17), which exhibits the most significant limb darkening. The Buie spectral sunshape $\hat{\mathscr{L}}_{Buie}(\lambda,\theta)$ is located in the

lower left, and appears to be very similar to the reference spectral sunshape estimated earlier in this Chapter, which is the final depicted spectral sunshape $\hat{\mathscr{L}}_{HM}(\lambda,\theta)$.

Recall that the Hestroffer-Magnan spectral sunshape developed in this Chapter had a peak spectral radiance of 0.0160 $[Wm^{-2}nm^{-1}arcmin^{-1}]$. The uniform, Gaussian and Buie spectral sunshapes respectively exhibit peak spectral radiance of 0.0142, 0.0212, and 0.0156 $[Wm^{-2}nm^{-1}arcmin^{-1}]$, or relative differences of -11%, $+32.5\%$ and -2.44%. The colour map and vertical axes have all been scaled according to the Gaussian spectral sunshape to allow for a fair comparison. Figure 2.12 shows clear differences which are mostly the result of the underlying limb darkening models. The estimated $\hat{\mathscr{L}}_{HM}(\lambda,\theta)$ and $\hat{\mathscr{L}}_{Buie}(\lambda,\theta)$ strongly resemble each other, which makes sense because the Hestroffer-Magnan spectral limb darkening model and the Buie sunshape are based on similar solar telescope observations. The Buie model however does not consider spectral information, and a closer look is required to distinguish the spectral differences.

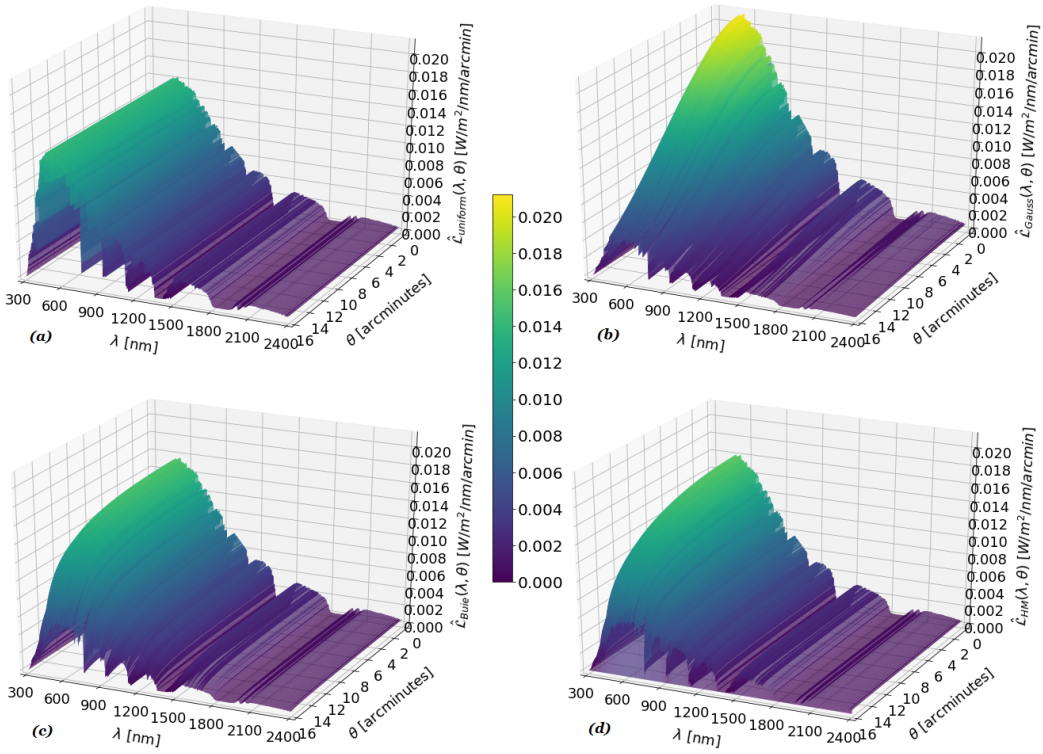

Figure 2.12: All four spectral sunshapes, formatted to share the same colour map and z-axis. (a), (b), (c) and (d) respectively show $\hat{\mathscr{L}}_{uniform}(\lambda,\theta)$, $\hat{\mathscr{L}}_{Gauss}(\lambda,\theta)$, $\hat{\mathscr{L}}_{Buie}(\lambda,\theta)$, and the estimated $\hat{\mathscr{L}}_{HM}(\lambda,\theta)$

To contrast the spectral sunshapes in more detail, the reference spectral sunshape $\hat{\mathscr{L}}_{Buie}(\lambda,\theta)$ was also subtracted from every other spectral sunshape. That is, for every

$i = uniform, Gauss, Buie$, the spectral sunshape difference in Equation (2.22) was constructed:

$$\text{diff}(\hat{\mathscr{L}}_{Buie}, \hat{\mathscr{L}}_{HM}, \lambda, \theta) = \mathscr{L}_{Buie}(\lambda, \theta) - \mathscr{L}_{HM}(\lambda, \theta) \tag{2.22}$$

The spectral sunshape differences also have units $[Wm^{-2}nm^{-1}arcmin^{-1}]$, and it is insightful to also have a relative percentage point difference metric to compare the representations as a whole. To that end, define the 'average deviation' AvDev_i between spectral sunshape i and $\hat{\mathscr{L}}_{HM}(\lambda, \theta)$ to be the average of the absolute difference over the entire domain divided by the average value of $\hat{\mathscr{L}}_{HM}(\lambda, \theta)$. Letting $|x|$ denote the absolute value of x, AvDev_i is defined as follows:

$$\text{AvDev}_i = \frac{\text{Av}[|\text{diff}(\hat{\mathscr{L}}_i, \hat{\mathscr{L}}_{HM}, \lambda, \theta)|]}{\text{Av}[\mathscr{L}_{HM}(\lambda, \theta)]} * 100\%; \qquad \text{Av}[f(\lambda, \theta)] \overset{def}{=} \frac{\iint_{\Lambda,\Theta} f(\lambda, \theta) d\lambda d\theta}{\iint_{\Lambda,\Theta} 1 d\lambda d\theta} \tag{2.23}$$

The average deviation AvDev_i is simply a measure of the extent to which a particular spectral sunshape $\hat{\mathscr{L}}_i(\lambda, \theta)$ deviates from the reference $\hat{\mathscr{L}}_{HM}(\lambda, \theta)$ over the entire wavelength domain Λ and opening half-angle domain Θ. The closer to 0 the value of AvDev_i, the better the two spectral sunshapes agree.

Recall from Section 1.3.3 that an optical train topology is oriented optimally when it is aimed at the solar vector; this ensures that the largest share of total flux arrives near the focal point as designed. Section 1.3.3 also elucidated how, in the case of idealised optical elements, radiance corresponding to the solar vector is perfectly propagated throughout the optical train and arrives at the focal point as designed. On the contrary, increasing the value θ of a ray will also increase the mismatch between the incident ray and the focal design point. The lower θ is, the better the propagation throughout an optical train. For CPV applications it therefore follows that spectral radiance is more important the lower θ is.

It therefore follows that another interesting metric is the spectral sunshape difference at the solar vector $\theta = 0'$ or $\text{diff}(\hat{\mathscr{L}}_i, \hat{\mathscr{L}}_{HM}, \lambda, 0')$ in terms of Equation (2.22). This difference at the solar vector can likewise be converted to an average deviation by plugging in $\theta = 0'$ in Equation (2.23) and averageing over the wavelength domain instead. Crucially, since the half-angle dimension is collapsed, the average deviation at $\theta = 0'$ essentially captures the spectral mismatch for the flux that is most likely to arrive at the receiver. The spectral mismatch is very important, considering the spectral response of HCPV receivers such as the multi-junction stack or the spectral beam splitting approach.

The uniform spectral sunshape difference, or $\text{diff}(\hat{\mathscr{L}}_{uniform}, \hat{\mathscr{L}}_{HM})$, is plotted in Figure 2.13, with an $\text{AvDev}_{uniform}$ of 8.44%. The discrepancy due to limb darkening - which is implicitly absent for the uniform spectral sunshape - is apparent. The uniform spectral sunshape exhibits significantly less spectral radiance near the centre of the Sun: the average deviation for $\theta = 0'$ is 8.59%. On the other hand, the uniform sunshape vastly overstates the spectral radiance near the limb. The crossover - where the difference is approximately zero - occurs for an opening half-angle slightly larger than $\theta = 10'$. Applying these results to a CPV optical train topology, it follows that the uniform spectral

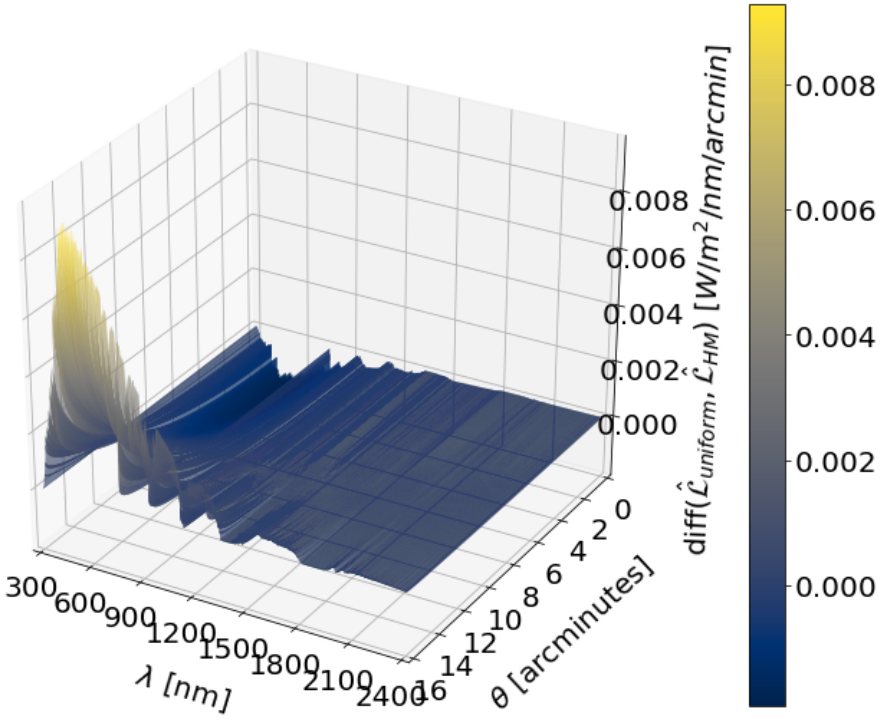

Figure 2.13: Difference between the uniform spectral sunshape $\hat{\mathscr{L}}_{uni}(\lambda,\theta)$ and the estimated spectral sunshape $\hat{\mathscr{L}}_{HM}(\lambda,\theta)$. The average deviation is 8.44%.

sunshape would underestimate the solar flux that propagates properly and arrives near the focal point.

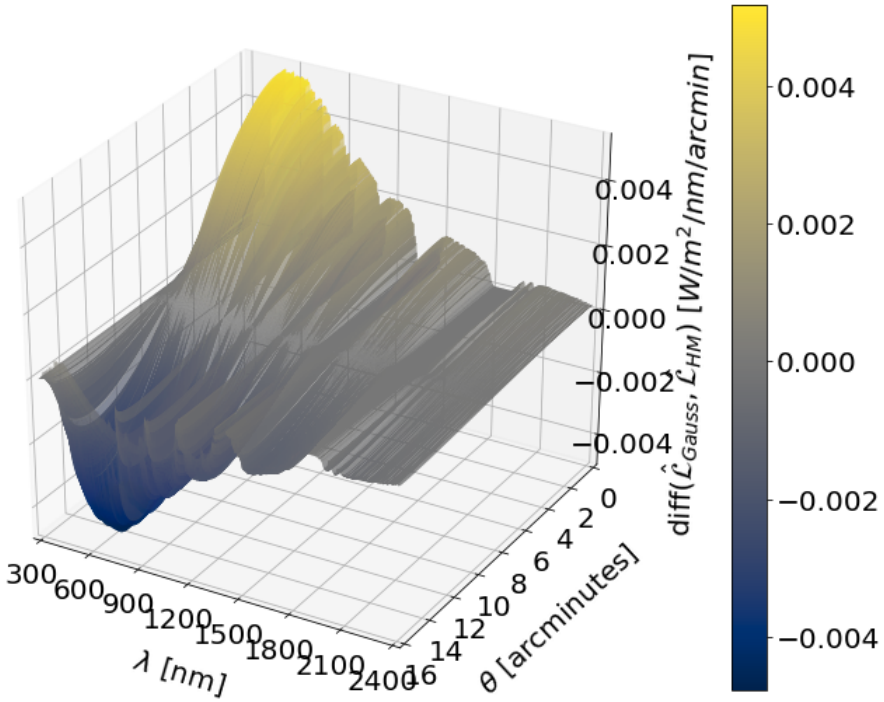

Figure 2.14: Difference between the Gaussian spectral sunshape $\hat{\mathcal{L}}_{Gauss}(\lambda,\theta)$ and the estimated spectral sunshape $\hat{\mathcal{L}}_{HM}(\lambda,\theta)$. The average deviation is 25.2%.

Secondly, Figure 2.14 shows diff($\hat{\mathcal{L}}_{Gauss}, \hat{\mathcal{L}}_{HM}$), which exhibits a very high AvDev$_{Gauss}$ of 25.2%. The Gaussian spectral sunshape implies limb darkening that is too severe, as the spectral radiance is significantly higher at low values of θ and lower for high values of θ. The crossover occurs for a value of θ slightly smaller than 8′. The Gaussian spectral sunshape vastly overestimates the spectral radiance near the solar vector $\theta = 0'$; the average deviation for $\theta = 0'$ stands at 36.4%. As such, an optical train analysis employing a Gaussian source model would tremendously overestimate the solar flux propagated by the optical train.

Finally, diff($\hat{\mathcal{L}}_{Buie}, \hat{\mathcal{L}}_{HM}$) is displayed in Figure 2.15. The spectral sunshape corresponding to the Buie sunshape model shows good agreement with the spectral sunshape $\hat{\mathcal{L}}_{HM}(\lambda,\theta)$ derived in this Chapter. Ignoring the discrepancies near the solar limb, the differences are approximately an order of magnitude smaller compared to the uniform and Gaussian cases. AvDev$_{Buie}$ = 3.19%, but a sizeable share of the deviation is contributed by the region near the limb as θ approaches 16′. As was mentioned in Section The limb is the region where both the Hestroffer-Magnan spectral limb darkening model

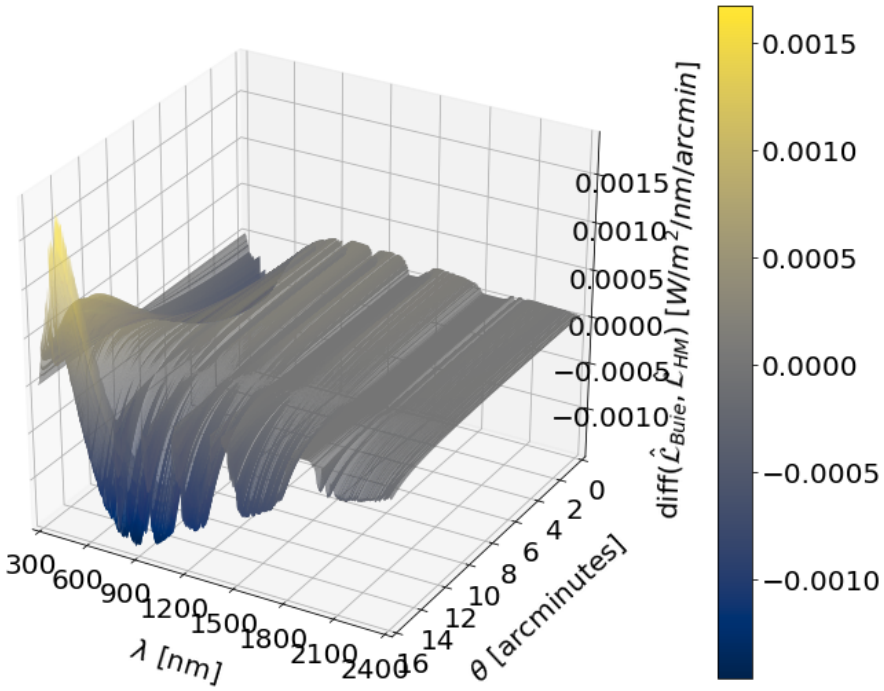

Figure 2.15: Difference between the spectral sunshape $\hat{\mathscr{L}}_{Buie}(\lambda,\theta)$ corresponding to the Buie sunshape and the estimatewd spectral sunshape $\hat{\mathscr{L}}_{HM}(\lambda,\theta)$. The average deviation is 3.19%.

agrees relatively poorly with the data, at ±10%. The Buie sunshape model agrees excellently with the measurements at the very limb, but also deviates slightly below the limb [41]. Both representations suffer from the difficulty of capturing a partially asymptotic phenomenon - that of the limb - with a parsimonious trigonometric function. Artefacts of this nature are very likely the culprit for the sudden inversion in the diff($\hat{\mathscr{L}}_{Buie}, \hat{\mathscr{L}}_{HM}$) plot at short wavelengths and as $\theta \rightarrow 16'$.

Aside from the inversion artefact near the solar limb, two important trends are visible in Figure 2.15. Firstly, the Buie spectral sunshape significantly underestimates the short wavelength spectral radiance near the solar vector $\theta = 0'$ and slightly overestimates the long wavelength spectral radiance there. This observation is underscored by the average deviation metric at $\theta = 0'$, which stands at 4.11%. This local average deviation is higher than the overall average deviation, despite the latter being inflated by the apparent artefact. It follows that the differences are most pronounced for spectral radiance close to the solar vector. Recall again that spectral radiance is more important for CPV the lower the value of θ, as better propagation to the receiver target is implied for such spectral radiance.

The second apparent trend is the reversion of the first trend as θ increases one moves away from the solar centre to its limb. It is particularly visible that longer wavelength spectral radiance is underestimated by the Buie spectral sunshape at higher values of θ. Both trends are direct improvements owed to the spectral limb darkening model incorporated into $\hat{\mathscr{L}}_{HM}(\lambda, \theta)$, and they quantify the quasi-qualitative arguments in the rationale from Section 2.2.

All in all, the differences between the spectral sunshape $\hat{\mathscr{L}}_{HM}(\lambda, \theta)$ derived in this work and the sunshapes agnostic of spectral limb darkening are striking. The uniform spectral sunshape, implicit if one were to treat the Sun as an extended source without any limb darkening, significantly deviates from the spectral sunshape $\hat{\mathscr{L}}_{HM}(\lambda, \theta)$. It would significantly underestimate the flux at a HCPV receiver. Counter-intuitively, considering computationally feasible limb darkening in the form of the Gaussian sunshape even worsens the problem, although instead the spectral radiance arriving at the receiver would be overestimated. The exceedingly accurate Buie sunshape model appears to agree well with the spectral sunshape, but still deviates significantly for exactly that subset of the spectral radiance domain that matters most for HCPV applications. It can be concluded that the opening half-angle and wavelength dependence of spectral radiance cannot be decoupled, and that a full spectral radiance source representation such as the spectral sunshape is necessary for HCPV system analysis.

2.6. APPLICATION TO OPTICAL MODELLING SOFTWARE TOOLS

This Section discusses how the spectral sunshape can be incorporated into existing optical modelling software. An elaborate review on state-of-the-art optical modelling tools used in CSP system analysis was presented by Li et al. [51], and a verification on sunshape implementations in particular was presented by Wang et al. [52]. A distinction is

made between two modelling categories: Monte Carlo ray-tracing (MCRT) and a convolution-based optics method. MCRT essentially randomly samples photons from a specified directional radiance distribution, computes the optical path of this sample of photons throughout a specified optical train, and then infers the mapping from the source to the receiver based on the sample results.

The convolution-based method considers the specified directional distribution of solar photons in full, and maps this radiance distribution throughout the optical train by convolving the radiance distribution function with specified input-output distribution functions of optical element. Because the convolution of two Gaussian functions is easy from a processing power perspective, the Gaussian sunshape is typically the distribution of choice here. The MCRT method is numerical and therefore applicable to any topology, whilst the computational feasibility of the convolution-based method depends on the optical train topology.

All optical modelling tools covered in the cited literature are designed for CSP applications, and no HCPV-specific software exists. Importantly in the context of this thesis, all existing tools also implement the three prevalent sunshapes described in Section 2.5.2 but not a spectral radiance source representation. Whilst tools such as SolTrace and Tonatiuh do allow for specification of an incident spectral irradiance profile in conjunction with a sunshape, it is exactly this separate treatment of opening half-angle and wavelength that results in the corresponding spectral sunshapes depicted in 2.12.

Fortunately, only a single amendment is necessary to make the existing optical modelling tools suitable for HCPV applications: the existing source formulation must be replaced by ta spectral sunshape formulation such as the estimated spectral sunshape $\hat{\mathscr{L}}_{HM}(\lambda,\theta)$ depicted in Figure 2.9. In other words, the spectral sunshape should serve as the distribution from which photons are sampled in the MCRT tools, and should be mapped throughout the optical train in convolution-based tools. For MCRT applications, photons of a particular wavelength and direction θ should simply be sampled at a likelihood according to the value of the spectral sunshape. In essence, if the spectral sunshape in Figure 2.12 were transformed to a photon flux distribution through the photon energy relation $E_{ph} = \frac{hc}{\lambda}$, this transformed distribution could simply be treated as a probability density function to sample photons from.

Of course, drawing photons from a two-dimensional distribution rather than a one-dimensional one does require a larger sample size before the MCRT results converge to a result. An equivalent approach would be drawing vectors from an extended source much like the existing tools currently do, yet allocating a θ-specific spectrum to the vector rather than a slightly downscaled version of the AM1.5D spectrum. Referring to Figure 2.11, a vector making an angle of $\theta = 15'$ with the solar vector should correspond to the red spectrum, whilst the solar vector itself should correspond to the blue spectrum. Essentially, the vectors should lookup the corresponding spectrum from Equation (2.15).

In a very similar vein, the spectral sunshape can also be incorporated into the convolution-based method. This does require convolution-based tools to relinquish the conventional

and easily implemented Gaussian sunshape, which is probably a good idea regardless in light of the Figure 2.14. For such tools, it is the spectral sunshape that should be convolved with optical train elements. Of course this also requires a representation of optical train elements where the optical properties are expressed as a function of both wavelength and incident angle. It is exactly this representation that will be detailed in the next Chapter 3.

3

Optical Train Model

This Chapter aims to establish a model for heliostats, the optical train elements of interest, in order to put the spectral sunshape derived in the previous Chapter 2 to use. Firstly the framework of geometric optics to model propagation of light in a utility-scale High Concentration Photovoltaic (HCPV) system is justified in Section 3.1. Within this framework it is valid to employ rays as the element of analysis, and Section 3.1 also develops how solar rays should be mapped by a primary optical stage to achieve concentration. Section 3.2 introduces the paraboloid, and documents how it satisfies the primary optical stage requirements assuming perfectly specular reflection.

Perfectly specular reflection is impossible in reality, which could be particularly relevant for HCPV systems. A realistic optical train model should also consider imperfections in optical elements, which can be exhaustively divided into two cases: attenuation and optical errors. Attenuation is defined as energy loss upon interaction with a stage, such that the magnitude of the desired outgoing ray is smaller than that of the incident ray. For a reflective mirror such as a heliostat, attenuation is known as reflectance.

Optical errors are defined as errors resulting in a probability of the outgoing ray's direction being different than intended despite proper alignment. Section 3.3 will analyse the conventional heliostat materials, and in particular how reflectance and scattering - a source of optical error - depend on wavelength and incidence angle. Of interest is selecting a suitable material for HCPV purposes. Section 3.4 discusses other optical error sources for a HCPV optical train, and motivates the aggregation of several optical error sources into an overall optical error.

Section 3.5 develops how the overall optical error can be convolved with the spectral sunshape source representation to produce an effective post-reflection spectral radiance model. Finally, Section 3.5.1 performs this convolution for the heliostat case at hand, resulting in an equivalent effective source spectral radiance model for heliostats.

3.1. GEOMETRIC OPTICS AND THE VECTOR THEORY OF REFLECTION

Geometric optics employs rays, defined as infinitesimally narrow beams of light. Infinitesimal quantities tend to be convenient approximations, and this case is no different. The exact nature of light propagation is governed by Maxwell's equations. Solutions to Maxwell's equations are so-called wave optical fields, where the direction and amplitude are intertwined. If the wave optical fields are analytic, they can be represented in the form of a Taylor series. The base order approximation of a wave optical field's Taylor representation is called the ray optical field.

Crucially, for the ray optical field, the phase and amplitude are decoupled. This implies that direction and magnitude can be treated separately, which significantly facilitates analysis. Wave optical fields are analytic in a homogenous medium, such that the ray optical field exists. Furthermore, if the objects traversed by the light are considerably larger than the light's wavelength, higher order Taylor components are negligible. That is, the ray optical field accurately describes the full wave optical field solution. An elaborate overview of the relevant considerations for the validity of geometric optics is provided by Deschamps [53].

For the setting at hand of utility-scale HCPV systems, it can be safely assumed at the ray optical field approximation holds. Ray-tracing, the dominant method of analysis for similarly sized CSP systems, implicitly assumes geometric optics to be valid. It is thus sufficient to consider only the ray optical field, which allows for a decoupled analysis of direction and magnitude. In other words, it is valid to trace vectors throughout the optical train and couple This Section will first consider the directional aspect in the idealised case of rays, to develop the intuition of a concentrating topology.

From Maxwell's equations and boundary conditions, the general vector formula for perfectly specular reflection off a dielectric interface follows:

$$\hat{r} = \hat{\imath} - 2\,(\hat{\imath}\cdot\hat{n})\,\hat{n} \tag{3.1}$$

Here $\hat{r}$ denotes the unit vector describing the reflected ray, $\hat{\imath}$ the unit vector of the incident ray, and $\hat{n}$ the unit vector normal to the reflection interface. That is, if the normal vector at the dielectric interface $\hat{n}$ is determined, any incident unit vector can be mapped to a reflected vector.

Now, consider an Euclidean coordinate system with a focal point at the point $(0;0;F)$. Throughout this Chapter, the notation $(x;y;z)$ is used for vectors with components in the x, y and z directions. Additionally, consider a reflecting surface element located at an arbitrary point $I = (\bar{x};\bar{y};\bar{z})$. The goal of a primary optical stage is to redirect rays to the focal point. In terms of Equation (3.1), this is equivalent to requiring that $\hat{r}$ points from $(\bar{x};\bar{y};\bar{z})$ to $(0;0;F)$. Renormalisation by the vector's magnitude yields the following requirement for $\hat{r}$ t:

$$\hat{r}_{req} = \frac{1}{\sqrt{\bar{x}^2+\bar{y}^2+(F-\bar{z})^2}}\left(-\bar{x};-\bar{y};F-\bar{z}\right) \tag{3.2}$$

Equation (3.2) is thus the requirement for any reflecting surface located at $(\bar{x};\bar{y};\bar{z})$ to successfully map an incident ray $\hat{\imath}$ to $(0;0;F)$. Considering Equation (3.1), this requirement fully determines the desired orientation of the surface's normal vector $\hat{n}$.

In a HCPV central receiver topology, the goal is always to map the Sun's rays to the focal point. Recall that the Sun appears as an extended source for an observer on Earth, and that it is optimal for a HCPV primary optical stage to redirect the $\hat{\imath}$ vector corresponding to its centre to the focal point. Denote this unit vector originating in the centre of the Sun, also referred to as the solar vector, by $\hat{\imath}_{0'}(t)$. This unit vector is time-dependent because the Sun apparently moves across the sky. A HCPV primary optical stage therefore has a required surface orientation $\hat{n}_{req}(t)$ that maps $\hat{\imath}_{0'}(t)$ to $\hat{r}_{req}$.

Combining Equations (3.1) and (3.2) and substituting the relevant unit vectors yields the requirement in Equation (3.3). Recall that the entire left-hand side consists of fixed parameters: the arbitrary point of incidence $I=(\bar{x};\bar{y};\bar{z})$ and the fixed focal point height F. The right-hand side consists of two vectors: the input $\hat{\imath}_{0'}(t)$ and the required surface orientation $\hat{n}_{req}(t)$.

$$\frac{1}{\sqrt{\bar{x}^2+\bar{y}^2+(F-\bar{z})^2}}\left(-\bar{x};-\bar{y};F-\bar{z}\right)=\hat{\imath}_{0'}(t)-2\left(\hat{\imath}_{0'}(t)\cdot\hat{n}_{req}(t)\right)\hat{n}_{req}(t) \tag{3.3}$$

3.2. PARABOLOID OPTICAL JOURNEY

A familiar topology exists in 3D Euclidean space that is both smooth and capable of satisfying Equation (3.3) for all possible coordinates $(\bar{x};\bar{y};\bar{z})$: the paraboloid. A paraboloid is also known as a parabola of revolution, i.e. a 2D parabola revolved around its vertex. Smooth here refers to mathematical smoothness, which implies continuity and differentiability everywhere. Smoothness is convenient because it implies a globally well-defined gradient. Since a paraboloid is convex, it is also implied that reflected rays are not blocked by other surface elements on their way to the focal point.

To illustrate the paraboloid's properties, consider without loss of generality a Sun directly overhead, such that $\hat{\imath}_{0'}=(0;0;-1)$. The paraboloid is defined as follows:

$$Z_M(x,y)=\frac{x^2+y^2}{4F}, \qquad R_{min}<\sqrt{x^2+y^2}<R_{max} \tag{3.4}$$

The quantity F in the denominator is the focal length, and implies that the focal point of this paraboloid is indeed $(0;0;F)$. Both R_{min} R_{max} simply constrain the radial domain to $[R_{min},R_{max}]$. For any surface, the normal vector at any point can be computed by evaluating surface's gradient. Consider the implicit form $H_M(x,y,z)$ of Equation (3.4), which follows from simply subtracting z:

$$H_M(x,y,z)=Z_M(x,y)-z=\frac{x^2+y^2}{4F}-z=0 \tag{3.5}$$

The del operator is defined as $\nabla=\hat{x}\frac{\partial}{\partial x}+\hat{y}\frac{\partial}{\partial y}+\hat{z}\frac{\partial}{\partial z}$, where $\hat{x}$, $\hat{y}$ and $\hat{z}$ denote the unit vectors in the Cartesian coordinate system. The gradient is defined as follows:

$$\nabla H_M = \left(\frac{\partial H_M}{\partial x}; \frac{\partial H_M}{\partial y}; \frac{\partial H_M}{\partial z}\right) = \left(\frac{x}{2F}; \frac{y}{2F}; -1\right) \tag{3.6}$$

The gradient is not normalised yet, it is still necessary to divide by its magnitude to obtain the surface normal vector. Additionally, the normal vector of interest has a positive z-component rather than a negative one, so it is also necessary to multiply by -1. The desired unit vector follows:

$$\hat{n}_M(x,y) = \frac{2F}{\sqrt{x^2+y^2+4F^2}}\left(\frac{-x}{2F}; \frac{-y}{2F}; 1\right) \tag{3.7}$$

Substituting Equation (3.7) for $\hat{n}_{req}(t)$ and $\hat{i}_{0'} = (0;0;-1)$ for $\hat{i}_{0'}(t)$ in Equation (3.1) yields a reflected vector for any particular point of incidence $(\bar{x};\bar{y};\bar{z})$. Indeed, this exercise globally yields the required vector $\hat{r}_{req}$ in Equation (3.2). This demonstrates that the paraboloid Z_M properly redirects incident light rays that are parallel to to its vertex. This property holds for any $\hat{i}_{0'}$, as long as the paraboloid is rotated such that the vertex of the paraboloid is parallel to $\hat{i}_{0'}$. That is, as the Sun moves across the sky, the paraboloid is required to adjust its position and track it accordingly. This section will proceed assuming, without loss of generality, that the Sun is directly overhead. That is, $\hat{i}_{0'} = (0;0;-1)$ is the solar vector.

Having established that the solar vector ray is mapped to the focal point, let us now consider the optical journey of other solar rays. Consider a ray incident at an arbitrary point $(\bar{x};\bar{y};\bar{z})$ that forms an angle θ_i with the perpendicular incident ray $\hat{i}_{0'} = (0,0,-1)$. Such a vector satisfies the following constraints:

$$\hat{i}_\theta = \left(\hat{i}_{x,\theta}; \hat{i}_{y,\theta}; -\cos\theta\right), \quad \sqrt{\hat{i}_{x,\theta}^2 + \hat{i}_{y,\theta}^2} = \sin^2\theta \tag{3.8}$$

It is important to recall that the normal vector $\hat{n}_M(x,y)$ is determined for all x and y according to the vector from the Sun´s centre $\hat{i}_{0'} = (0,0,-1)$. Equation (3.1) can be used to compute the reflected ray. Since the incoming vector forms an angle θ_i with the ray $(0,0,-1)$ and the normal vector $\hat{n}_M(\bar{x},\bar{y})$ is the same, it can easily be verified that the reflected ray also deviates from $\hat{r}_{req}$ by the same angle θ_i. As such, the deviating ray will not pass through the focal point after reflection: the distance between the deviating ray and the focal point depends on the angle θ as well as the distance separating the point of incidence $I = (\bar{x};\bar{y};\bar{z})$ from the focal point $(0;0;F)$.

3.3. MATERIAL PROPERTIES: REFLECTANCE AND SCATTERING

Perfectly specular reflection was assumed in the previous section to illustrate the principles of concentration, and this section will consider material-induced limitations. Two relevant material properties, reflectance and scattering, can be discerned. Reflectance refers to energy loss upon interaction with a mirror, and scattering is an optical error. An ideal mirror material would have a reflectance of unity over the entire applicable wavelength and incidence angle domain, such that all of the incident energy is reflected. Furthermore, an ideal material would also exhibit perfectly specular reflection according to Equation (3.1), i.e. zero scattering, such that energy is redirected exactly as desired. In practice not all of the incident radiation is reflected, which constitutes a significant loss

factor, and material-inherent scattering results in imperfect specular reflection.
Both properties have been extensively studied in the literature. Reflectance is governed by the famous Fresnel equations, in which a material's reflective index appears. The refractive index in turn depends on wavelength, such that reflectance simultaneously depends on both arguments of spectral radiance, the incidence angle and wavelength [54]. Angular scattering results in a non-zero probability for an incident ray to exactly follow Snell's law, and can therefore be interpreted as an optical error. Reflector materials typically exhibit more scattering as the wavelength decreases, and also as the angle of incidence increases.

Good et al. measured the reflectance and scattering of "conventional and novel reflective materials for solar concentrators" under varying experimental conditions, including incidence angle and incident wavelength [55]. As such, their work exactly characterises the mirror properties required within the spectral radiance framework. Furthermore, Good et al. also published the raw measurement data [56]. Observations have been made at incident angles of 15°, 45° and 60°, for wavelengths ranging from $300nm$ to $2500nm$. As such, the wavelength domain contains the [300, 2400] nm domain of the estimated spectral sunshape from Equation (2.15) and Figure 2.9.
Since photovoltaic energy conversion is wavelength-dependent, reflectance $R_{spec}(\lambda)$ should also be considered per wavelength. In assessing a mirror's performance with respect to sunlight, it is therefore instrumental to weigh spectral reflectance according to direct spectral irradiance. To that end, define the solar-weighted spectral reflectance $R_{spec,\odot}$ to be:

$$R_{spec,\odot} = \frac{\int R_{spec}(\lambda) * AM1.5D(\lambda) d\lambda}{\int AM1.5D(\lambda) d\lambda} \tag{3.9}$$

$R_{spec,\odot} = 1$ is equivalent to all of the energy contained in the AM1.5D spectrum being reflected. In the Good et al. paper, Table 2 presents $R_{spec,\odot}$ for the tested reflectors at the three incidence angles considered. The silver-based mirrors exhibit the highest solar-weighted spectral reflectance, particularly the back-silvered glass mirrors and silvered aluminium sheets.

From Table 3 in the Good et al. paper, it appears that the 4 mm-thick back-silvered glass reflector by Flabeg and the aluminium reflector film by Toray exhibit the least angular scattering by a significant margin. The standard deviations of fitted single Gaussian angular scattering distributions are at least an order of magnitude smaller than for the other considered mirrors. For these two mirrors, the standard deviations for the same selection of wavelengths are replicated from the Good et al. paper and presented in Table 3.1. These two mirrors exhibit the least scattering, or equivalently a more specular reflection profile.

Recall that the opening half-angle subtended by the Sun is $16' = 4.65$ mrad, such that the standard deviations tabulated in Table 3.1 are approximately two orders of magnitude smaller. It can be concluded that, for these two mirrors, approximately specular reflection can be assumed. It follows that the aluminium reflector film and the 4 mm back-silvered glass reflector constitute suitable choices for a HCPV primary mirror based

on the scattering selection criterion.

Table 3.1: Standard deviations of fitted Gaussian scattering distributions for a selection of wavelengths and incidence angles, replicated from Good et al. [55]. The measurement setup has an angular resolution of 0.033 mrad, such that observations below that value are denoted as '< 0.033'.

	$\lambda[nm]$	350	400	500	555	600	700	800	950	1050
	AOI [°]					$\sigma[mrad]$				
AlFilm	15					<0.033 (all)				
	45					<0.033 (all)				
	60	0.042	0.048	0.042	0.038	<0.033	0.036	0.035	<0.033	<0.033
Ag4mm	15	<0.033	0.036				<0.033			
	45	0.040	0.043	0.0.042	0.048	<0.033	0.036	0.035	<0.033	<0.033
	60	0.060	0.064	0.057	0.055	0.053	0.053	0.058	0.053	0.049

The spectral reflectance data from these two reflectors are plotted in Figures 3.1 and 3.2. The dots denote observations, whilst the lines are cubic spline interpolations of the observations. For reference, the normalised AM1.5D spectrum is also plotted. The spectral reflectance of the 4 mm back-silvered glass mirror outperforms the aluminium film, as evidenced by the significantly higher values for $R_{spec,\odot}$. This superiority stems from the back-silvered glass' spectral reflectance being higher for those wavelengths where the direct solar spectrum also peaks. Assuming specular reflection, about 4% more energy would reach a receiver with back-silvered glass instead of aluminium film.

It should also be noted that the wavelengths at which silver-based mirrors reflect rather poorly also conveniently correspond to relatively inaccessible energy. Consider for example the [300, 400 nm] interval, in which the reflectances from Figure 3.1 climb towards 0.9. Photons corresponding to this interval are highly energetic, such that the lion's share of their energy will be lost due to thermalisation even in the highest band gap subcell in a multi-junction (MJ) cell. On the tail end of the wavelength range depicted in Figure 3.1, reflectance also declines. These photons in turn have an energy below even the lowest band gap material in MJ cells, such that these are non-absorbed anyway. The solar-weighted reflectance in Equation (3.9) does not fully capture these properties.

Perhaps even more importantly in the context of HCPV is the realisation that the thermalisation and non-absorption losses will eventually result in heat accumulation at a receiver. This is undesirable for HCPV systems, as the spatial confinement implies that heat becomes problematic and could hamper performance. The reflector spectral response in Figure 3.1 is therefore beneficial, as it filters out exactly those photons that particularly contribute to heat accumulation.

Finally, glass mirrors are the dominant mirror technology, and it is therefore likely that back-silvered reflectors are relatively affordable despite silver not being not the most abundant element. Thus, back-silvered glass is selected to comprise the first optical stage because of its limited scattering, its high solar-weighted spectral reflectance, and its beneficial filtering of inaccessible photons.

It is interesting to point out that selecting a material for a primary optical stage also has implications for successive optical stages. In particular, it is beneficial to choose a

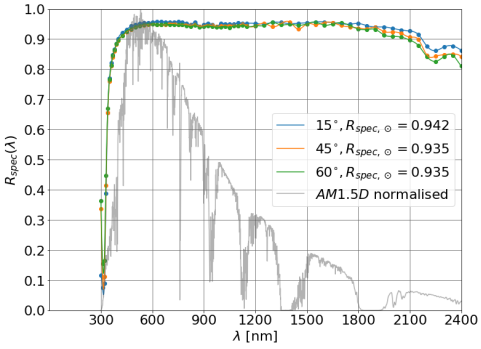

Figure 3.1: Spectral reflectance of 4 mm back-silvered glass for three angles of incidence [56]. The AM1.5D spectrum is also plotted.

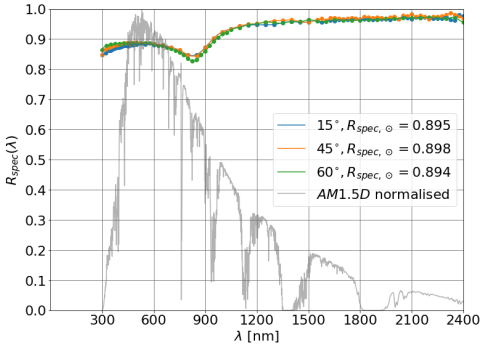

Figure 3.2: Spectral reflectance of aluminium film for three angles of incidence [56]. The AM1.5D spectrum is also plotted.

material with a similar spectral response for successive stages to maximise the ultimate flux. Multiple optical stages incurs extra losses, but these are minimal if the stages have a similar spectral response. To illustrate this principle, consider the extreme hypothetical case of a step-shaped spectral response for an optical stage; unity in an interval, zero elsewhere. Multiple such stages do not incur additional losses, i.e. 100% of the energy incident on the successive stages would be reflected.

For the realistic materials at hand, a weakened form of the same principle holds. Consider a second optical stage featuring a similar spectral reflectance to Figure 3.1. This second mirror's poor performance in the [300, 400 nm] interval hardly impacts outgoing flux, since a relatively small amount of energy from within this interval even reaches the second stage. On the contrary, if an aluminium film like Figure 3.2 is chosen as the second stage, one mirror's spectral strengths are undermined by the other mirror's weaknesses and vice versa. It is therefore beneficial for a second optical stage to exhibit a similar spectral reflectance as Figure 3.1, which hints at a silver-based second stage.

To incorporate the back-silvered glass mirror into the spectral radiance framework, a characterisation of reflectance depending on both wavelength and angle of incidence is necessary. Unfortunately, the information at hand to base such estimates on is rather limited. The Good et al. measurements cover many wavelengths, but only three angles of incidence. To make matters worse, a 60° AOI hardly ever applies to a heliostat in a terrestrial application, such that the corresponding reflectance data are meaningless. Additionally, Good et al. obtained no measurements for a 0° AOI, and no spectral reflectance datasheet is presently available from the now-defunct manufacturer Flabeg. However, Good et al. state that the manufacturer Flabeg reported a $R_{spec,\odot} > 0.945$ for 0° AOI. Consulting the literature, Sutter et al. found that the reflectance of silvered-glass mirrors is almost independent of incidence angle up until 70° [57].

The small impact of incidence angle is also apparent in Figure 3.3. The [400, 1200 nm] domain of Figure 3.1 is depicted, which contains 79.7% of the total irradiance in AM1.5D. The specular reflectance is generally shifted upwards for an AOI of 15° compared to 45°,

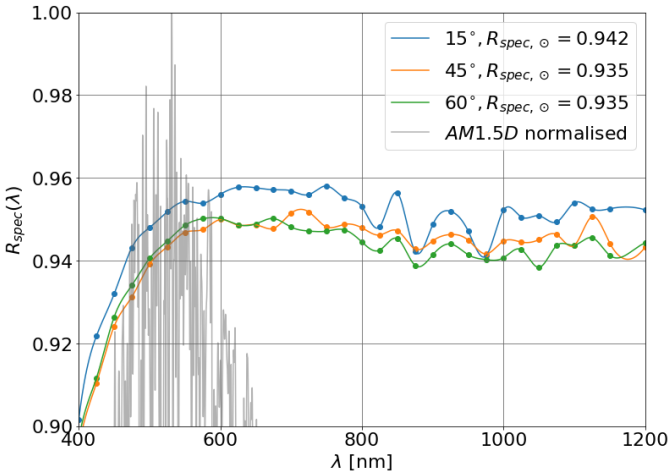

Figure 3.3: Specular reflectance for 4 mm back-silvered glass for the [400,1200 nm] range which corresponds to 79.7% of the irradiance in AM1.5D.

but there is no such apparent global difference between the 45° and 60° series. The 0.07 difference in $R_{spec,\odot}$ between the 15° and 45° series is small, but still significant in case of HCPV's concentration factors above 100x. The significance is also augmented in case of multiple optical stages. Thus, in an effort to recognise the impact of incidence angle, a simple model of specular reflectance linear in angle of incidence is postulated. It is based on the difference between the 15° and 45° Good et al. data. Letting $R_{15}(\lambda)$ and $R_{45}(\lambda)$ denote the corresponding spectral reflectance series from Figure 3.1:

$$\hat{\mathscr{R}}(\lambda, AOI) = \frac{R_{45}(\lambda) - R_{15}(\lambda)}{30°} * (AOI - 15°) + R_{15}(\lambda) \qquad AOI \in [0°, 45°] \tag{3.10}$$

By construction, this simple linear model reproduces the $R_{15}(\lambda)$ and $R_{45}(\lambda)$ Good et al. series upon substitution of the two angles of incidence. Validity of the estimator $\hat{\mathscr{R}}(\lambda, AOI)$ is dubious inside the [15°,45°] range, because of the limited information on which it is based. The [0°,15°] validity is even more questionable because there is no spectral data for an AOI of 0°. Substitution of normal incidence ($AOI = 0°$) into Equations (3.10) and (3.9) results in a solar-weighted reflectance of 0.946. This value agrees with the value reported by the manufacturer (> 0.945), which supports the validity of the estimator for the [0°,15°] range.

Thus, despite the limitations of the estimator in Equation (3.10), it will be considered because it is superior to disregarding AOI entirely. It should be noted that the separation of spectral reflectance into a spectral component and a linear angle of incidence factor is supported by the reasonable assumption of specular reflection due to negligible scattering. Decoupling the two variables would otherwise be problematic, especially given the intertwined nature of the spectral sunshape.

Combining the representation in Equation (3.10) with the estimated spectral sunshape $\hat{\mathscr{L}}_{HM}(\lambda,\theta_i)$ from Equation (2.15), it is now possible to estimate the spectral radiance that reflects off a point on a back-silvered glass mirror placed at a particular angle of incidence with respect to the Sun:

$$\hat{\mathscr{L}}_{refl}(\lambda, AOI, \theta_{\hat{r}_{0'}}) \approx \hat{\mathscr{R}}(\lambda, AOI) * \hat{\mathscr{L}}_{HM}(\lambda,\theta_i) * cos(AOI) \tag{3.11}$$

Recall that θ was defined as the angle between the solar vector ($\theta = 0'$) and a particular vector. Let us label this variable θ as developed in Chapter 2 as θ_i, to emphasise that it corresponds to an incident ray. Following the reflection identity in Equation (3.1), the solar vector $\theta_i = 0'$ is mapped to some $\hat{r}_{0'}$. Let us define the angle $\theta_{\hat{r}_{0'}}$ to be the angle between any vector and the vector $\hat{r}_{0'}$.

Similar to how $\hat{\mathscr{L}}_{HM}(\lambda,\theta_i)$ is a cone around the centre of the Sun, $\hat{\mathscr{L}}_{refl}(\lambda,\theta_{\hat{r}_{0'}})$ is a cone centred around the vector $\hat{r}_{0'}$. Furthermore, the factor $cos(AOI)$ stems from the cosine law for radiance at an angle. Equation (3.11) is not presented as an exact equality, because perfect specularity (reflection governed exactly by Equation (3.1)) is implicitly assumed in the construction of $\hat{\mathscr{R}}(\lambda, AOI)$. Equation (3.11) thus represents the spectral radiance leaving a point on a back-silvered glass mirror placed at a particular angle of incidence.

3.4. OPTICAL TRAIN ERRORS

Optical errors are defined as directional errors that do not attenuate. In terms of Equation (3.1), an incident ray $\hat{\imath}$ has a nonzero probability of resulting in a reflected vector with a direction different from $\hat{r}$ if an optical error is significant. In other words, the reflection identity does not hold with absolute certainty due to optical errors. Scattering at a material interface is an example of such an optical error, although the previous section demonstrated the insignificance of this optical error for the selected mirror material.

Another optical error that is often significant in practice is known as the tracking error. Recall that for a HCPV system with a fixed focal point, primary stage mirrors have to be continually reoriented as the Sun apparently moves across the sky. This is known as tracking, and the mechanical nature of reorientation results in inevitable tracking errors. External random events, such as a fluctuating wind load on a heliostat, might also induce optical errors. Any practical primary optical stage will necessarily deviate from the idealised system at times. This is particularly important for HCPV applications, as the inherent exacerbation of angular deviations amplifies the effect on receiver flux.

In the nomenclature of the primary stage requirement expressed earlier in Equation (3.3), recall that the primary optical stage should readjust its required surface $\hat{n}_{req}(t)$ over time to track the apparently moving solar vector. Optical errors can be interpreted as external errors that cause the actual orientation to deviate from the required orientation. This section will consider these optical errors in detail, and discuss the assumptions underlying aggregation of these individual errors into an overall optical error.

3.4.1. TRACKING ERROR

Let us first consider the inevitable tracking error. The tracking problem is the surface reorientation to continuously satisfy $\hat{n}_{req}(t)$. The tracking problem is continuously identified, because the location $(\bar{x};\bar{y};\bar{z})$ is fixed, the distance F to the focal point is known, and the apparently moving solar vector $\hat{\imath}_{0'}(t)$ is also determined at all times. HCPV systems require dual-axis tracking, which enables freedom in reorientation satisfying Equation (3.3) is possible regardless of the apparent position of the Sun. Continuously tracking perfectly is impossible; let the actual reflected vector be $\hat{r}_{\epsilon_{tr}}$ rather than the $\hat{r}_{rec}$ from Equation (3.2), where ϵ_{tr} denotes an angular tracking error term. That is, the inner product between this reflected vector and the ideal vector $\hat{r}_{\bar{M},||}$ is as follows:

$$cos(\epsilon_{tr}) = \hat{r}_{\epsilon_{tr}} \cdot \hat{r}_{req} \tag{3.12}$$

This equation holds by construction; ϵ_{tr} is defined as the error that ensures it holds at all times. Of interest is the distribution of the error term ϵ_{tr} over time. It is an obvious requirement for a viable tracking system that the error term is mean-zero, i.e. the expected value at a point in time is 0: $\mathbb{E}[\epsilon_{tr} \mid t] = 0$. This is equivalent to the requirement that the tracking system must aim at the focal point on average. At times the tracking might deviate, but it should not systematically do so in any particular direction. If there would be a systematic bias such that $\mathbb{E}[\epsilon_{tr} \mid t] \neq 0$, it would be better to readjust the tracking algorithm such that is becomes mean-zero. Not much else can be said about the distribution of ϵ_{tr}; the literature typically computes a standard sample error based on experimental data. For the purposes of this chapter, it is sufficient to adopt the mean-zero requirement, and that its variance σ^2_{tr} is finite.

$$\mathbb{E}[\epsilon_{tr} \mid t] = 0, \quad \mathbb{E}[\epsilon^2_{tr} \mid t] = \sigma^2_{tr} < \infty, \quad \forall t \tag{3.13}$$

3.4.2. OTHER OPTICAL TRAIN ERRORS

Secondly, consider the error due to imperfectly manufactured mirrors. Such errors can be understood as deviations from the ideal surface normal vector for a mirror. That is, even if the tracking system maintains perfect aim at a point in time, there might be local bumps or irregularities on a mirror surface such that the reflected vector still deviates from the required vector $\hat{r}_{rec}$. Let ϵ_m denote this angular manufacturing error, in a similar fashion to ϵ_{tr}, with assumed finite variance σ^2_m. The effect of these irregularities is similar to that of tracking errors, in the sense that the actual reflected vector deviates from the idealised direction. An important difference arises however, because surface imperfection errors are systematic in nature. That is, if there is a deformity, the resulting reflected vector will deviate in the same direction for all points in time.

The crucial assumption for manufacturing errors is twofold. Firstly, there is no expected preferred direction of manufacturing-induced deviation. Secondly, deformities are not more likely to exist at any particular position $(\bar{x};\bar{y};\bar{z})$ versus others. Then, the expected deviation for any point on a surface is still zero: a priori, $\hat{r}_{\bar{M},||}$ is the expected direction for the reflected vector. Note that this assumption does not hold for all points in time, because as mentioned earlier there will be systematic deviations. However, it is assumed that exactly how these systematic deviations will appear is indeterminable

at the time of design. Denoting variance by σ_m^2, similar error term requirements are assumed:

$$\mathbb{E}[\epsilon_m \mid \bar{x}, \bar{y}, \bar{z}] = 0, \quad \mathbb{E}[\epsilon_m^2 \mid \bar{x}, \bar{y}, \bar{z}] = \sigma_{tr}^2 < \infty, \quad \forall \bar{x}, \bar{y}, \bar{z} \tag{3.14}$$

Other optical errors such as wind pressure on a mirror can be treated in a similar manner. The crucial assumption that should hold for all significant optical errors is that the expected resultant vector direction is $\hat{r}_{\bar{M},||}$ globally.

3.4.3. OVERALL OPTICAL ERROR

Aggregating all individual optical error components into an overall optical error is a common strategy in the CSP literature, motivated by the central limit theorem. The central limit theorem states that, if many individual mean-zero error sources with finite variance contribute to the overall error and no single error source dominates the others, then the resulting overall error tends to an approximately zero-mean Gaussian distribution. Note that the central limit theorem does not impose functional form requirements on the individual error source distributions, other than having finite variance and being mean-zero.

Invoking the central limit theorem is not entirely justified because, in practice, tracking errors do tend to dominate the overall optical error [58]. The literature however does consistently assume a Gaussian tracking error distribution. Overall optical error is then the aggregation of a dominant Gaussian zero-mean error and several mean-zero error sources. Such an aggregation also tends towards an approximately zero-mean Gaussian distribution. Furthermore, more accurate tracking systems could reduce the variance σ_m^2 and hence curtail the stochastic dominance of the tracking error term. Attaining a tracking error variance more in line with the other error sources appears to be a matter of tracking system quality and thus system costs. In case the tracking error's variance is similar in magnitude to the other errors' variances, the aforementioned central limit theorem holds. In conclusion, an aggregated Gaussian optical error follows in both the case of a Gaussian dominant tracking term, and the case of a dominant optical error source. Given the limited information on the individual error structures, it is also not possible to do better. As such, the overall optical error ϵ_{opt} is assumed to follow a zero-mean Gaussian distribution defined by an overall optical error σ_{opt}^2:

$$\sigma_{opt}^2 = \sigma_t^2 + \sigma_m^2 + \sum_i^{other} \sigma_i^2 \tag{3.15}$$

Bonanos reports that this overall optical error typically has a value in the range of $[1-3$ mrad$]$. Scattering is normally also considered as a component of this optical error, but it was already incorporated separately in Section 3.3. It is often also a significant contributor to the overall optical error, as evidenced by the other reflector characteristics reported by Good et al. In this case however, having selected a mirror material exhibiting minor angular scattering, it is not a significant contributor. For this analysis, an overall optical error of $7'$, i.e. slightly over 2 mrad, is assumed.

The corresponding Gaussian probability density function $f_{\epsilon_{opt}}(\theta)$ for the overall optical error is depicted in Figure 3.4. The overall optical error should be interpreted as follows: for a ray of light incident at an angle θ_{in} with respect to the surface normal, the probability that the reflected ray is within the angular cone ϵ_{tot} centred around θ_{out} is equal to the probability density function's integral. θ_{out} is related to θ_{in} by the law of specular reflection. That is, 68.27% of reflected rays fall within an angular cone of $7'$, 95.45% fall within an angular cone of $14'$, etc. It does not matter which individual error source - or combination of individual sources - results in the deviation, as all are aggregated into this distribution of outcomes.

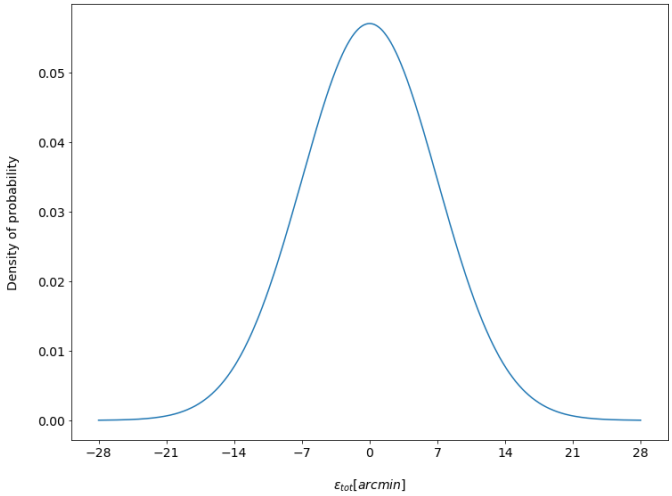

Figure 3.4: Probability density function $f_{\epsilon_{opt}}(\theta)$ for a Gaussian distribution with a standard deviation of $7'$.

3.5. COMBINATION INTO EFFECTIVE SOURCE

Recall that Equation (3.11) denoted the spectral radiance reflected by a realistic mirror which is perfectly aimed. The previous Section (3.4) established a representation for the overall optical error. Combining these two yields a representation of the expected spectral radiance reflected by a realistic mirror in realistic operating conditions. This procedure yields a spectral radiance profile that is realistically reflected by the primary optical stage in a HCPV system.

To combine the two, it is necessary to assume that the overall optical error developed in Section 3.4 is independent of wavelength. This appears to be a reasonable assumption, considering its components. If a tracking error results in a deviation in direction at a point in time, it is very reasonable to assume that this induced deviation is the same for any two wavelengths. Thus, the distribution of ϵ_{tr} does not depend on wavelength. Analogously for surface imperfections, bumps can be reasonably assumed to reflect blue and red light to the same incorrect direction.

The assumption of wavelength independence does not follow as naturally for angular scattering, which is known to depend simultaneously on wavelength and incidence angle. This is why a representation in both wavelength and incidence angle was developed in Section 3.3. Since the scattering angular error for back-silvered glass at $\approx 0.04 mrad$ is two orders of magnitude smaller than the overall optical error of $\approx 2 mrad$ assumed, it can be safely assumed that wavelength-depending scattering in this setting does not violate the assumption of the overall optical error being wavelength-independent. Furthermore, the scattering angular error being an order of magnitude smaller also implies that an interaction effect between scattering and other individual optical errors is insignificant.

Incorporating the Gaussian optical error model into the reflected spectral radiance representation from Equation (3.11) requires a convolution. To illustrate why, consider a particular ray pointing from the surface in the direction of the focal point. Without loss of generality, consider $\hat{r}_{req}$ from Equation (3.2). The spectral radiance along this required direction does not just originate from the incident ray with direction $\hat{\imath}(0')$. As a result of the angular dispersion from the optical errors, a contribution also comes from other incident rays. Additionally, a share of the incident radiance along $\hat{\imath}(0')$ is also dispersed to post-reflection directions other than $\hat{r}_{req}$.

To compute the spectral radiance in a particular direction, it is therefore necessary to convolve the incident spectral radiance with the Gaussian optical error model. That is, all incident rays should be considered and appropriately weighted by the probability that the incident ray results in a particular outgoing ray. Therefore, the effective spectral radiance centred around $\hat{r}_{req}$ is obtained by convolving the spectral radiance leaving a mirror from Equation (3.11) with the optical error Gaussian distribution $f_{\epsilon_{opt}}(\theta)$ depicted in Figure 3.4:

$$\hat{\mathscr{L}}_{eff}(\lambda, AOI, \theta_{eff}) = \int f_{\epsilon_{opt}}(\theta_{eff} - \theta_{\hat{r}_{0'}}) * \hat{\mathscr{L}}_{refl}(\lambda, AOI, \theta_{\hat{r}_{0'}}) d(\theta_{\hat{r}_{0'}}) \tag{3.16}$$

Again, θ_{eff} is defined as the angle between any vector and the vector $\hat{r}_{req}$ around which the spectral radiance distribution is centred It is important to note that this convolution has no relatively simple analytic expression, even though the right-hand side terms in the integral do. The mean-zero Gaussian probability density function is straightforward, and $\hat{\mathscr{L}}_{refl}(\lambda, AOI, \theta_{\hat{r}_{0'}})$ also has an analytic representation following Equations (2.15) and (3.10).

The result for an AOI of 15° is depicted in Figure 3.5. This figure thus represents the spectral radiance leaving a primary optical stage, considering both a realistic mirror and an overall optical error with a standard deviation of 7′. For reference, the incident spectral sunshape is also plotted with the same axes and colourmap in Figure 3.6. It is visible that the optical errors effectively smear the energy out over a wider angular domain.

Furthermore, the optical errors significantly affect the peak of the spectral radiance profile: the peak value is 0.0142 $[Wm^{-2}nm^{-1}arcmin^{-1}]$, which is 11.3% smaller than the 0.0160 $[Wm^{-2}nm^{-1}arcmin^{-1}]$ peak in Figure 3.6. The fact that the peak radiance

is redirected incorrectly at times due to optical errors results in this smaller magnitude for time-averaged radiance, as does the attenuation due to reflection. Since the solar-weighted spectral reflectance $R_{spec,\odot}$ is approximately 0.942 for an AOI of 15° as visible in Figure 3.1, it follows that a sizeable percentage of the spectral radiance loss at $\theta = 0'$ is due to the optical errors. Recall that the spectral radiance near $\theta = 0'$ is most important for a HCPV system, such that the loss is quite significant.

Interestingly, the $\theta \in [0', 30']$ domain depicted in Figure 3.5 contains 132.8 $[Wm^{-2}]$ upon integration along both dimensions, which is 99.7% of the 141.3 $[Wm^{-2}]$ contained in the spectral sunshape. That is, assuming an overall optical error with a standard deviation of $7'$, the lion's share of the spectral radiance leaves the mirror surface within a cone of $30'$. As Figure 3.5 shows, a very large share is even within a cone of $16'$.

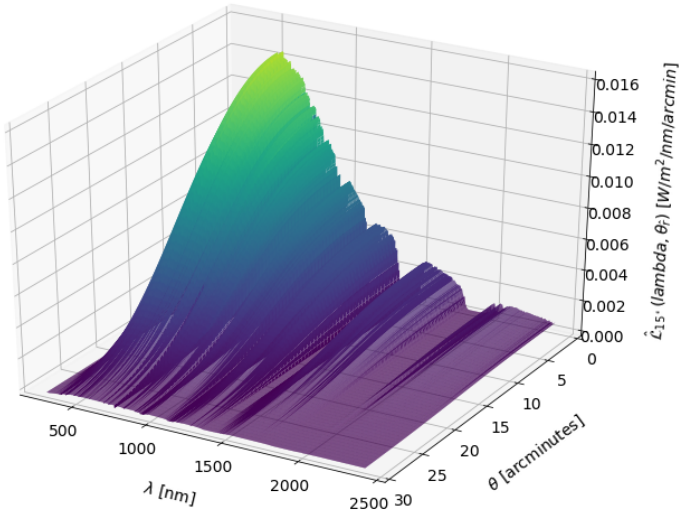

Figure 3.5: Spectral radiance after reflection by a back-silvered glass mirror at a 15° angle of incidence with respect to the Sun, assuming a total optical error with a standard deviation of $7'$. The colour mapping is identical to the mapping in Figures 2.9 and 3.6

.

3.5.1. THE BENDT-RABL EFFECTIVE SOURCE MODEL

It was already discussed that, for erroneously reflected spectral radiance, it is ultimately irrelevant to which individual source the error should be attributed. This idea can be extended to the treatment of optical train stages as a whole. For a receiver, a mirror resulting in the spectral radiance profile from Figure **??** centred at $\hat{r}_{req}$ is equivalent to an emitting surface exhibiting the very same spectral radiance profile. That is, the mirror can be considered an effective source. Bendt and Rabl developed an analytic effective source model which incorporates an aggregate optical error model into a sunshape model [59], and the spectral radiance profile from Figure 3.5 is an extension of an effective sunshape source model to an effective spectral sunshape model.

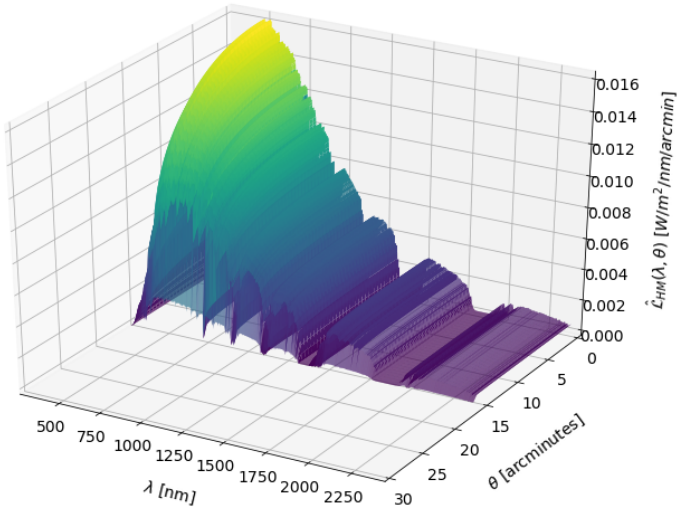

Figure 3.6: Spectral sunshape from Figure 2.9, plotted using the same axes as Figure 3.5.

3.5.2. COMPUTATIONAL ADVANTAGE

Treating heliostats as effective sources is an effective method to reduce the processing power required to adequately model a HCPV system. Conventionally, a system's geometry is defined in a setting and then globally illuminated by a specified radiance profile. Rays from the source then intersect the primary optical stage, a reflection is computed, and rays are traced further along their path. The entire procedure echoes the optical train model developed in this Chapter. On the other hand, it is also possible to define heliostats as emitting surfaces with the spectral radiance profile in Figure 3.5. The difference between these two strategies is indistinguishable for the receiver, but the effective source approach does not require computation of the first reflection.

Since illumination is globally the same, i.e. the spectral sunshape is incident on the entire heliostat field, the only difference between individual heliostats arises from their individual orientations with respect to the Sun, captured entirely by the parameter AOI. The required AOI is known at all times since the tracking problem is identified, and it is thus possible to use Equation (3.16) to determine the spectral radiance profile of heliostats as an effective source. This represents an important advantage in terms of reducing processing power, as the primary optical stage interaction step is largely avoided altogether. The size of the gains do depend on the ease of a convolution with the optical error model of choice, but they are probably a net positive in many cases.

The effective source approach features another significant computational advantage, which is that only the heliostat field is emitting rather than the entire domain. Many modelling tools work with a globally illumination profile as the input. As a result, many

rays will be generated that do not interact with a heliostat due to the open space between them to prevent shading and blocking. Even though such rays are not the most demanding, they are entirely spared by an effective source model.

4

CONCLUSION AND RECOMMENDATIONS

This work presented the first spectral radiance source representation of the Sun, defined as the spectral sunshape. Spectral radiance is the physical quantity that should be considered for HCPV system analysis, since dependence on opening half-angle θ and wavelength λ is interlinked through spectral limb darkening. To that end, the spectral sunshape $\hat{\mathscr{L}}_{HM}(\lambda,\theta)$ was constructed from the established AM1.5D spectrum in conjunction with the Hestroffer-Magnan spectral limb darkening model, as detailed in Equations (2.9)-(2.11).

State-of-the-art software packages implement a sunshape model, the workhorse in CSP, and a spectral irradiance standard, employed in PV. The spectral sunshape was compared to three prevalent sunshape models used in such software packages, which all implicitly assume decoupling of wavelength and opening half-angle dependence of solar flux. It was demonstrated that the differences are profound, even in case of the exceedingly accurate Buie sunshape model: a spectral mismatch of 4.11% was found. If one were to analyse a HCPV system using the Buie sunshape in existing modelling software, the simulated irradiance at the focal point would be redshifted. If one were to use the uniform or Gaussian sunshape instead, very significant differences are the result. To extend the validity of CSP modelling software to the realm of HCPV, it is necessary to implement a spectral sunshape source representation. Both Monte Carlo ray-tracing tools and convolution-based tools can incorporate the spectral sunshape model presented in this work.

It is implied by spectral limb darkening that the spectral irradiance at a receiver necessarily differs from an upscaled version of the incident spectrum, due to the interaction of angular exacerbation inherent in concentration (Section 1.3.3), spectral limb darkening (2.2, and the fact that the Sun is not a point source. This is a finding with significant

impact on the field of HCPV receiver design, as receiver designs documented thus far typically did assume such an upscaled spectrum. Considering the spectral response of HCPV receivers, and in particular the current-matching requirement for multi-junction stacks, it follows that existing receivers are current-limited by design. It is thus recommended to first calculate how spectral radiance is mapped throughout an optical train to a receiver, and to only then design a receiver based on the calculated receiver flux profile.

In Chapter 3, a suitable heliostat candidate for HCPV was identified based on superior specularity, spectral reflectance properties and its current status as market leader: the back-silvered glass reflector. Successive optical stages should also be based on silver to minimise the overall attenuation, and to reduce thermal flux generation at the receiver. Motivated by the relative insignificance of optical errors due to scattering, a spectral reflectance model of the heliostat linear in the angle of incidence was proposed, and combined with the spectral sunshape to estimate the spectral radiance reflected off a back-silvered glass mirror.

The final optical train modelling step was incorporating optical train errors, i.e. errors that violate perfect specularity but that do not attenuate. Several optical error sources that are comparable in magnitude were aggregated into a single overall Gaussian optical error by invoking the central limit theorem. A Gaussian optical error with a standard deviation of 7 arcminutes was assumed, and convolved with the spectral sunshape post-reflection.

The result of this exercise was the effective spectral sunshape depicted in Figure 3.5. This effective spectral sunshape can be interpreted as the spectral radiance profile reflected off of the heliostat surface under realistic operating conditions. The heliostat can equivalently be considered as an effective source with the derived spectral radiance profile. Doing so conveys a computational advantage, as it skips the calculation step where the inbound radiance interacts with the heliostat. Additionally, less processing power is necessary versus a setting with globally defined illumination as any rays that fall between heliostats are not even generated.

Unfortunately, the very final intended step of the analysis proved to be unfeasible with the tools and skills at hand: quantification of the performance loss induced by a heliostat field. The extent of this performance loss is extremely important for the future viability of HCPV, seeing as it is very unlikely that other primary optical stages such as Fresnel lenses will ever reach a price level that justifies the HCPV approach over conventional utility-scale PV. The final step is sorely missed, especially because all of the inputs required for the quantification were developed in this work. On the other hand, the quantification of the optical performance loss due to a heliostat field is a textbook recommendation for future work in this field.

All in all though, the main goal of this research has been attained: the establishment of a spectral radiance standard, as well as a framework to analyse HCPV systems. In HCPV receiver design, the assumption of an incident AM1.5D spectrum upscaled by a concentration factor C becomes progressively more invalid the higher C is. The most

valid receiver design method would entail calculating the receiver flux profile by mapping the spectral sunshape through a specified optical train. The optical train mapping should consider both attenuation and optical errors as function of wavelength for the primary stage, and as functions of both wavelength and angle for succcessive stages. All tools necessary to assess HCPV receivers in detail have been presented, and it is now possible for the HCPV industry to quantify designs and hopefully continue moving along its promising learning curve.

A

APPENDIX

A.1. DEMONSTRATION OF SOLAR POTENTIAL

The solar constant, defined as the solar flux incident on the outer atmosphere of the Earth, averages at 1.361 . The flux is incident on the Earth as seen from the Sun, i.e. on a surface area of where denotes the radius of the Earth: 6,371 km. Assuming for simplicity's sake that half of the energy is lost in the voyage from the outer atmosphere to the Earth's surface due to absorption and scattering, it follows that on average approximately in irradiation is incident on the Earth's surface. Total global annual energy production from all sources amounted to in 2015 according to the IEA (ref:Key World Energy Statistics 2017) , such that it takes less than 110 minutes for that amount of energy to arrive at the Earth's surface. In other words, the 2015 annual global energy supply arrives in the form of sunlight at Earth's surface in just 0.0209% of the total time in a year. This calculation demonstrates that dedicating just a fraction of the Earth's surface to solar energy generation would be enough to comfortably meet society's demand.

A.2. DEMONSTRATION OF INCREASED EFFICIENCY UNDER CONCENTRATION

The interesting phenomenon that extractable energy increases more than proportionally as a function of the incident irradiance is easily understood by considering a solar cell under STC. The maximum-power-point (MPP) output per unit area of a solar cell is given by

$$P_{MPP} = V_{MPP} * J_{MPP} = V_{OC} * J_{SC} * FF \tag{A.1}$$

P_{MPP} ,V_{MPP} and J_{MPP} respectively denote the power per unit area, voltage, and current density at MPP. V_{OC} is the open-circuit voltage, J_{SC} the short-circuit current density, and FF the fill factor. The total incident irradiance under STC is the integral of the AM1.5G spectrum, denoted by $P_{AM1.5G}$. Hence, the efficiency of the cell is given by

$$\eta_{STC} = \frac{P_{MPP}}{P_{AM1.5G}} = \frac{V_{OC} * J_{SC} * FF}{P_{AM1.5G}} \tag{A.2}$$

A

Note that the short-circuit current density is given by

$$J_{SC} = -e \int_0^{\lambda_G} EQE(\lambda) * \Phi_{AM1.5G}(\lambda) d\lambda \tag{A.3}$$

Where e is the elementary charge, $\lambda_G = \frac{hc}{E_G}$ is the wavelength corresponding to the band gap energy, $EQE(\lambda)$ is the External Quantum Efficiency as a function of wavelength and finally $\Phi_{AM1.5G}$ is the STC spectral photon flux.

Next, consider incident irradiance scaled by a concentration factor C, such that $\tilde{P}_C = C * P_{AM1.5G}$. Since the spectral profile is the same, the photon flux $\tilde{\Phi} = C * \Phi_{AM1.5G}(\lambda)$. In the neighbourhood of STC illumination conditions, the EQE is largely invariant for concentrated irradiance: $\widetilde{EQE}(\lambda) \approx EQE(\lambda)$. Therefore, the increased photon flux results in a proportionally increased short-circuit current density:

$$\tilde{J}_{SC} = -e \int_0^{\lambda_G} \widetilde{EQE}(\lambda) * \tilde{\Phi}(\lambda) d\lambda \approx C * J_{SC} \tag{A.4}$$

The effect of concentration on the open-circuit voltage V_{OC} is also relatively straightforward. Assuming that the short-circuit current density far exceeds the dark current density, i.e. $J_{SC} >> J_0$, V_{OC} is given by

$$V_{OC} = \frac{kT}{e} \ln(\frac{J_{SC}}{J_0}) \tag{A.5}$$

where k is Boltzmann's constant, T is the temperature. Since the dark current density by definition does not vary under different illumination conditions, it follows that

$$\tilde{V}_{OC} = \frac{kT}{e} \ln(\frac{\tilde{J}_{SC}}{J_0}) = \frac{kT}{e} \ln(\frac{J_{SC}}{J_0}) + \frac{kT}{e} \ln(C) = V_{OC} + \frac{kT}{e} \ln(C) \tag{A.6}$$

That is, the open-circuit voltage increases logarithmically as a function of the concentration ratio. Assuming an unchanged fill factor, substituting the derived concentration into Equations A.1 and A.2, it follows that

$$\tilde{\eta} = \frac{\tilde{P}_{MPP}}{C * P_{AM1.5G}} = \frac{(V_{OC} + \frac{kT}{e} \ln(C)) * C * J_{SC}}{C * V_{OC} * J_{SC}} = \eta_{STC} * (\frac{kT}{e * V_{OC}} \ln(C) + 1) \tag{A.7}$$

Equation A.7 shows that efficiency increases logarithmically as the concentration ratio increases. In Figure 1.4 the largest share of the 'other losses' are due to the V_{MPP} being lower than the band gap, and concentration essentially decreases this fundamental loss contribution. Concentration violates assumption SQ2, which is why exceeding the SQ limit is possible. The theoretical efficiency limits per junction number from **martilimit** under a single Sun and optimal concentration are tabulated in Table 1.1.

It should be noted though that the derivation assumes that the external quantum efficiency (EQE), and fill factor (FF) of the considered cell do not decrease. For the vast majority of semiconductor materials, these assumptions are valid in the neighbourhood of one Sun. As the concentration ratio increases significantly though the EQE will drop;

Table A.1: SMARTS inputs to produce reference spectra (Gueymard)

Sun's zenith angle (degrees)	48.236
Air mass	1.50
Surface slope/azimuth (degrees)	37/180
Angle of incidence: beam normal, hemispherical tilt (degrees)	0, 11.236
Field-of-view total angle: beam normal, hemispherical tilt (degrees)	5.8(DNI), N/A(GHI)
Extraterrestrial spectrum	SMARTS/Gueymard AM0
Earth-Sun distance correction	1
Model atmosphere	USSAa
Aerosol model S&F	Ruralb
Surface pressure (mb)	1013.25
Aerosol Optical Depth at 500 nm	0.084
Carbon dioxide mixing ratio	370 ppm
Pollution level	Standard
Ozone (atm-cm)	0.344
Precipitable water (cm)	1.416
Albedo	Light sandy soil, non-Lambertian

the available valence electrons will become limiting as the number of photons keeps on increasing. The FF will also drop as the concentration ratio increases to very high levels; from Equation (A.4), the current increases proportionally such that at some point Ohmic losses will play a significant role. Other phenomena might also invaldiate the assumptions of constant EQE and FF as concentration increases for particular semiconductor materials. The initial positive relationship between efficiency and concentration ratio that breaks down as concentration becomes very high results in a characteristic similar to 1.11 for the vast majority of PV cells.

A.3. SMARTS INPUTS TO PRODUCE THE REFERENCE SPECTRA PROPOSED BY GUEYMARD

BIBLIOGRAPHY

[1] Lazard Ltd, "Lazard's levelized cost of energy analysis," Lazard, Tech. Rep. September, 2015, pp. 0–15. [Online]. Available: http://www.lazard.com/.

[2] I. Renewable Energy Agency, "Renewable Power Generation Costs in 2017," *International Renewable Energy Agency*, 2018.

[3] P. R. I. F. O. R. S. E. S. ISE, "Photovoltaics Report," Tech. Rep., 2012. [Online]. Available: www.ise.fraunhofer.de.

[4] W. Shockley and H. J. Queisser, "Detailed balance limit of efficiency of p-n junction solar cells," *Journal of Applied Physics*, vol. 32, no. 3, pp. 510–519, 1961, ISSN: 00218979. DOI: 10.1063/1.1736034. [Online]. Available: https://ui.adsabs.harvard.edu/abs/1961JAP....32..510S/abstract.

[5] C. A. Gueymard, D. Myers, and K. Emery, "Proposed reference irradiance spectra for solar energy systems testing," *Solar Energy*, vol. 73, no. 6, pp. 443–467, 2002, ISSN: 0038092X. DOI: 10.1016/S0038-092X(03)00005-7. [Online]. Available: www.elsevier.com/locate/solener.

[6] A. Martí and G. L. Araújo, "Limiting efficiencies for photovoltaic energy conversion in multigap systems," *Solar Energy Materials and Solar Cells*, vol. 43, no. 2, pp. 203–222, Sep. 1996, ISSN: 09270248. DOI: 10.1016/0927-0248(96)00015-3. [Online]. Available: https://www.sciencedirect.com/science/article/pii/0927024896000153.

[7] A. H. M. Smets, K. Jäger, O. Isabella, R. A. v. Swaaij, and M. Zeman, *Solar energy : the physics and engineering of photovoltaic conversion, technologies and systems LK - https://tudelft.on.worldcat.org/oclc/944318061*. UIT Cambridge Limited, 2016, ISBN: 9781906860325 1906860327. [Online]. Available: https://research.tudelft.nl/en/publications/solar-energy-the-physics-and-engineering-of-photovoltaic-conversi.

[8] A. Richter, M. Hermle, and S. W. Glunz, "Reassessment of the limiting efficiency for crystalline silicon solar cells," *IEEE Journal of Photovoltaics*, vol. 3, no. 4, pp. 1184–1191, 2013, ISSN: 21563381. DOI: 10.1109/JPHOTOV.2013.2270351.

[9] M. Green, E. Dunlop, J. Hohl-Ebinger, M. Yoshita, N. Kopidakis, and X. Hao, "Solar cell efficiency tables (version 57)," *Progress in Photovoltaics: Research and Applications*, vol. 29, no. 1, pp. 3–15, Jan. 2021, ISSN: 1099159X. DOI: 10.1002/pip.3371. [Online]. Available: https://onlinelibrary.wiley.com/doi/10.1002/pip.3371.

[10] G. F. Brown and J. Wu, "Third generation photovoltaics," *Laser and Photonics Reviews*, vol. 3, no. 4, pp. 394–405, Jul. 2009, ISSN: 18638880. DOI: 10.1002/lpor.200810039. [Online]. Available: http://doi.wiley.com/10.1002/lpor.200810039.

[11] P. Pérez-Higueras, J. P. Ferrer-Rodríguez, F. Almonacid, and E. F. Fernández, *Efficiency and acceptance angle of High Concentrator Photovoltaic modules: Current status and indoor measurements*, 2018. DOI: 10.1016/j.rser.2018.06.011.

[12] C. Algora and I. Rey-Stolle, *Handbook of Concentrator Photovoltaic Technology*, C. Algora and I. Rey-Stolle, Eds. Chichester, West Sussex: John Wiley & Sons, Ltd, Apr. 2016, pp. 1–772, ISBN: 9781118755655. DOI: 10.1002/9781118755655. [Online]. Available: http://doi.wiley.com/10.1002/9781118755655.

[13] J. Zeitouny, E. A. Katz, A. Dollet, and A. Vossier, "Band gap engineering of multijunction solar cells: Effects of series resistances and solar concentration," *Scientific Reports*, vol. 7, no. 1, 2017, ISSN: 20452322. DOI: 10.1038/s41598-017-01854-6.

[14] R. M. France, F. Dimroth, T. J. Grassman, and R. R. King, "Metamorphic epitaxy for multijunction solar cells," *MRS Bulletin*, vol. 41, no. 3, pp. 202–209, Mar. 2016, ISSN: 08837694. DOI: 10.1557/mrs.2016.25. [Online]. Available: https://www.cambridge.org/core/terms.https://doi.org/10.1557/mrs.2016.25Downloadedfromhttps://www.cambridge.org/core.TU.

[15] A. Mojiri, R. Taylor, E. Thomsen, and G. Rosengarten, "Spectral beam splitting for efficient conversion of solar energy - A review," *Renewable and Sustainable Energy Reviews*, vol. 28, pp. 654–663, Dec. 2013, ISSN: 13640321. DOI: 10.1016/j.rser.2013.08.026. [Online]. Available: https://www.sciencedirect.com/science/article/pii/S1364032113005662.

[16] B. Mitchell, G. Peharz, G. Siefer, M. Peters, T. Gandy, J. C. Goldschmidt, J. Benick, S. W. Glunz, A. W. Bett, and F. Dimroth, "Four-junction spectral beam-splitting photovoltaic receiver with high optical efficiency," *Progress in Photovoltaics: Research and Applications*, vol. 19, no. 1, pp. 61–72, Jan. 2011, ISSN: 10627995. DOI: 10.1002/pip.988. [Online]. Available: http://doi.wiley.com/10.1002/pip.988.

[17] G. Paternoster, "Silicon Concentrator Solar Cells : Fabrication , Characterization and Development of Innovative Designs .," *undefined*, no. March, 2013.

[18] H. F. Hong, T. S. Huang, W. Y. Uen, and Y. Y. Chen, "Damp-heat induced performance degradation for Ingap/Gaas/Ge triple-junction solar cell," *Journal of Nanomaterials*, vol. 2014, 2014, ISSN: 16874129. DOI: 10.1155/2014/410717.

[19] F. Trieb, C. Schillings, M. O. '. Sullivan, T. Pregger, and C. Hoyer-Klick, "Global Potential of Concentrating Solar Power," *SolarPaces Conference Berlin*, no. September, pp. 1–11, 2009.

[20] C. A. Gueymard, "Spectral circumsolar radiation contribution to CPV," *AIP Conference Proceedings*, vol. 1277, pp. 316–319, 2010, ISSN: 0094243X. DOI: 10.1063/1.3509220. [Online]. Available: http://rredc.nrel.gov/solar/old_data/circumsolar/.

[21] R. Winston, L. Jiang, and M. Ricketts, "Nonimaging optics: a tutorial," *Advances in Optics and Photonics*, vol. 10, no. 2, p. 484, 2018, ISSN: 1943-8206. DOI: 10.1364/aop.10.000484. [Online]. Available: https://doi.org/10.1364/AOP.10.000484.

[22] H. Baig, K. C. Heasman, and T. K. Mallick, *Non-uniform illumination in concentrating solar cells*, Oct. 2012. DOI: 10.1016/j.rser.2012.06.020.

[23] R. Herrero, M. Victoria, C. Domínguez, S. Askins, I. Antón, and G. Sala, "Understanding causes and effects of non-uniform light distributions on multi-junction solar cells: Procedures for estimating efficiency losses," in *AIP Conference Proceedings*, vol. 1679, American Institute of Physics Inc., Sep. 2015, p. 050 006, ISBN: 9780735413269. DOI: 10.1063/1.4931527. [Online]. Available: http://aip.scitation.org/doi/abs/10.1063/1.4931527.

[24] K. Shanks, S. Senthilarasu, and T. K. Mallick, "Optics for concentrating photovoltaics: Trends, limits and opportunities for materials and design," *Renewable and Sustainable Energy Reviews*, vol. 60, pp. 394–407, Jul. 2016, ISSN: 18790690. DOI: 10.1016/j.rser.2016.01.089. [Online]. Available: https://www.sciencedirect.com/science/article/pii/S1364032116001192.

[25] P. H. A. Veríssimo, R. A. Campos, M. V. Guarnieri, J. P. A. Veríssimo, L. R. do Nascimento, and R. Rüther, "Area and LCOE considerations in utility-scale, single-axis tracking PV power plant topology optimization," *Solar Energy*, vol. 211, pp. 433–445, Nov. 2020, ISSN: 0038092X. DOI: 10.1016/j.solener.2020.09.070.

[26] O. Dupré, R. Vaillon, and M. A. Green, "Physics of the temperature coefficients of solar cells," *Solar Energy Materials and Solar Cells*, vol. 140, pp. 92–100, Sep. 2015, ISSN: 09270248. DOI: 10.1016/j.solmat.2015.03.025.

[27] O. Z. Sharaf and M. F. Orhan, *Concentrated photovoltaic thermal (CPVT) solar collector systems: Part I - Fundamentals, design considerations and current technologies*, Oct. 2015. DOI: 10.1016/j.rser.2015.05.036.

[28] S. P. Philipps, A. W. Bett, K. Horowitz, and S. Kurtz, "Current Status of Concentrator Photovoltaic (CPV) Technology," Fraunhofer ISE, Tech. Rep., Apr. 2015, pp. 1–25. [Online]. Available: http://www.ise.fraunhofer.de/en/publications/veroeffentlichungen-pdf-dateien-en/studien-und-konzeptpapiere/current-status-of-concentrator-photovoltaic-cpv-technology.pdf.

[29] H. Apostoleris, M. Stefancich, and M. Chiesa, *Concentrating Photovoltaics (CPV): The Path Ahead*, ser. Green Energy and Technology. Cham: Springer International Publishing, 2018, pp. 19–31, ISBN: 978-3-319-62979-7. DOI: 10.1007/978-3-319-62980-3. [Online]. Available: http://link.springer.com/10.1007/978-3-319-62980-3.

[30] M. A. Green and S. P. Bremner, "Energy conversion approaches and materials for high-efficiency photovoltaics," *Nature Materials*, vol. 16, no. 1, pp. 23–34, 2016, ISSN: 14764660. DOI: 10.1038/nmat4676. [Online]. Available: www.nature.com/naturematerials.

[31] K. A. W. Horowitz, M. Woodhouse, H. Lee, and G. P. Smestad, "A bottom-up cost analysis of a high concentration PV module," no. April, p. 100 001, 2015. DOI: 10.1063/1.4931548. [Online]. Available: http://aip.scitation.org/doi/abs/10.1063/1.4931548.

[32] J. E. Haysom, O. Jafarieh, H. Anis, K. Hinzer, and D. Wright, "Learning curve analysis of concentrated photovoltaic systems," *Progress in Photovoltaics: Research and Applications*, vol. 23, no. 11, pp. 1678–1686, Nov. 2015, ISSN: 1099159X. DOI: 10.1002/pip.2567. [Online]. Available: https://onlinelibrary.wiley.com/doi/10.1002/pip.2567.

[33] *Snapshot 2020 - IEA-PVPS*. [Online]. Available: https://iea-pvps.org/snapshot-reports/snapshot-2020/.

[34] O. Z. Sharaf and M. F. Orhann, *Concentrated photovoltaic thermal (CPVT) solar collector systems: Part II - Implemented systems, performance assessment, and future directions*, 2015. DOI: 10.1016/j.rser.2014.07.215.

[35] G. Mittelman, A. Kribus, O. Mouchtar, and A. Dayan, "Water desalination with concentrating photovoltaic/thermal (CPVT) systems," *Solar Energy*, vol. 83, no. 8, pp. 1322–1334, 2009, ISSN: 0038092X. DOI: 10.1016/j.solener.2009.04.003. [Online]. Available: http://dx.doi.org/10.1016/j.solener.2009.04.003.

[36] M. T. Islam, N. Huda, A. B. Abdullah, and R. Saidur, *A comprehensive review of state-of-the-art concentrating solar power (CSP) technologies: Current status and research trends*, Aug. 2018. DOI: 10.1016/j.rser.2018.04.097.

[37] A. Pfahl, J. Coventry, M. Röger, F. Wolfertstetter, J. F. Vásquez-Arango, F. Gross, M. Arjomandi, P. Schwarzbözl, M. Geiger, and P. Liedke, "Progress in heliostat development," *Solar Energy*, vol. 152, pp. 3–37, Aug. 2017, ISSN: 0038092X. DOI: 10.1016/j.solener.2017.03.029.

[38] C. Davila-Peralta, M. Rademacher, N. Emerson, G. Chavez-Lopez, P. Sosa, R. Cabanillas, R. Peon-Anaya, N. Flores-Montijo, N. Didato, and R. Angel, "Progress in track-mounted heliostat," in *AIP Conference Proceedings*, vol. 2303, American Institute of Physics Inc., Dec. 2020, p. 0 028 486, ISBN: 9780735440371. DOI: 10.1063/5.0028486. [Online]. Available: https://arizona.pure.elsevier.com/en/publications/progress-in-track-mounted-heliostat.

[39] M. Pharr, W. Jakob, and G. Humphreys, *Physically based rendering: From theory to implementation: Third edition*. 2016, pp. 1–1233, ISBN: 9780128006450. [Online]. Available: https://www.pbrt.org/.

[40] C. A. Gueymard, "Parameterized transmittance model for direct beam and circumsolar spectral irradiance," *Solar Energy*, vol. 71, no. 5, pp. 325–346, Oct. 2001, ISSN: 0038092X. DOI: 10.1016/S0038-092X(01)00054-8.

[41] D. Buie, A. G. Monger, and C. J. Dey, "Sunshape distributions for terrestrial solar simulations," *Solar Energy*, vol. 74, no. 2, pp. 113–122, Feb. 2003, ISSN: 0038092X. DOI: 10.1016/S0038-092X(03)00125-7.

[42] P. Blanc, B. Espinar, N. Geuder, C. Gueymard, R. Meyer, R. Pitz-Paal, B. Reinhardt, D. Renné, M. Sengupta, L. Wald, and S. Wilbert, "Direct normal irradiance related definitions and applications: The circumsolar issue," *Solar Energy*, vol. 110, pp. 561–577, 2014, ISSN: 0038092X. DOI: 10.1016/j.solener.2014.10.001.

[43] Aleš Kučera, *SOLAR PHOTOSPHERE*. [Online]. Available: https://www.astro.sk/~choc/open/apvv_0816-11/output/presentations/2014_13_hvar_colloquium/kucera_13_hvar_colloquium.pdf.

[44] F. Biggs and C. N. Vittitoe, "Helios model for the optical behavior of reflecting solar concentrators," Sandia National Laboratories (SNL), Albuquerque, NM, and Livermore, CA (United States), Tech. Rep., Mar. 1979, p. 31 806. DOI: 10.2172/6273705. [Online]. Available: http://adsabs.harvard.edu/abs/1979STIN...7931806B.

[45] D. Grether, J. Nelson, and M. Wahlig, "<title>Measurement Of Circumsolar Radiation</title>," in *Optics in Solar Energy Utilization I*, Y. Katz, Ed., vol. 0068, SPIE, Mar. 1976, pp. 41–48. DOI: 10.1117/12.978100. [Online]. Available: http://proceedings.spiedigitallibrary.org/proceeding.aspx?articleid=1225459.

[46] A. K. Pierce and C. D. Slaughter, "Solar limb darkening - I: $\lambda\lambda$(3033-7297)," *Solar Physics*, vol. 51, no. 1, pp. 25–41, Jan. 1977, ISSN: 00380938. DOI: 10.1007/BF00240442. [Online]. Available: https://ui.adsabs.harvard.edu/abs/1977SoPh...51...25P/abstract.

[47] A. K. Pierce, C. D. Slaughter, and D. Weinberger, "Solar limb darkening in the interval 7404-24 018 Å, II," *Solar Physics*, vol. 52, no. 1, pp. 179–189, Apr. 1977, ISSN: 00380938. DOI: 10.1007/BF00935800. [Online]. Available: https://ui.adsabs.harvard.edu/abs/1977SoPh...52..179P/abstract.

[48] H. Neckel and D. Labs, "Solar limb darkening 1986-1990 ($\lambda\lambda$303 to 1099 nm)," *Solar Physics*, vol. 153, no. 1-2, pp. 91–114, Aug. 1994, ISSN: 00380938. DOI: 10.1007/BF00712494. [Online]. Available: https://link.springer.com/article/10.1007/BF00712494.

[49] H. Neckel, "On the wavelength dependency of solar limb darkening (AA303 to 1099 nm)," *Solar Physics*, vol. 167, no. 1-2, pp. 9–23, 1996, ISSN: 00380938. DOI: 10.1007/BF00146325. [Online]. Available: https://link.springer.com/article/10.1007/BF00146325.

[50] D. Hestroffer and C. Magnan, "Wavelength dependency of the Solar limb darkening," Tech. Rep. 1, 1998, pp. 338–342. [Online]. Available: https://ui.adsabs.harvard.edu/abs/1998A&A...333..338H/abstract.

[51] L. Li, J. Coventry, R. Bader, J. Pye, and W. Lipiński, "Optics of solar central receiver systems: a review," *Optics Express*, vol. 24, no. 14, A985, Jul. 2016, ISSN: 1094-4087. DOI: 10.1364/oe.24.00a985. [Online]. Available: www.cspworld.org/cspworldmap..

[52] Y. Wang, D. Potter, C. A. Asselineau, C. Corsi, M. Wagner, C. Caliot, B. Piaud, M. Blanco, J. S. Kim, and J. Pye, "Verification of optical modelling of sunshape and surface slope error for concentrating solar power systems," *Solar Energy*, vol. 195, pp. 461–474, Jan. 2020, ISSN: 0038092X. DOI: 10.1016/j.solener.2019.11.035. [Online]. Available: https://doi.org/10.1016/j.solener.2019.11.035.

[53] G. A. Deschamps, "Ray Techniques in Electromagnetics.," *Proceedings of the IEEE*, vol. 60, no. 9, pp. 1022–1035, 1972, ISSN: 00189219. DOI: 10.1109/PROC.1972.8850. [Online]. Available: http://citeseerx.ist.psu.edu/viewdoc/summary?doi=10.1.1.186.1182.

[54] J. S. Gondek, G. W. Meyer, and J. G. Newman, "Wavelength dependent reflectance functions," in *Proceedings of the 21st Annual Conference on Computer Graphics and Interactive Techniques, SIGGRAPH 1994*, New York, New York, USA: Association for Computing Machinery, Inc, Jul. 1994, pp. 213–220, ISBN: 0897916670. DOI: 10.1145/192161.192202. [Online]. Available: http://portal.acm.org/citation.cfm?doid=192161.192202.

[55] P. Good, T. Cooper, M. Querci, N. Wiik, G. Ambrosetti, and A. Steinfeld, "Spectral reflectance, transmittance, and angular scattering of materials for solar concentrators," *Solar Energy Materials and Solar Cells*, vol. 144, pp. 509–522, Jan. 2016, ISSN: 09270248. DOI: 10.1016/j.solmat.2015.09.057.

[56] ——, "Spectral data of specular reflectance, narrow-angle transmittance and angle-resolved surface scattering of materials for solar concentrators," *Data in Brief*, vol. 6, pp. 184–188, Mar. 2016, ISSN: 23523409. DOI: 10.1016/j.dib.2015.11.059.

[57] F. Sutter, M. Montecchi, H. von Dahlen, A. Fernández-García, and M. Röger, "The effect of incidence angle on the reflectance of solar mirrors," *Solar Energy Materials and Solar Cells*, vol. 176, pp. 119–133, 2018, ISSN: 09270248. DOI: 10.1016/j.solmat.2017.11.029. [Online]. Available: https://doi.org/10.1016/j.solmat.2017.11.029.

[58] A. M. Bonanos, "Error analysis for concentrated solar collectors," *Journal of Renewable and Sustainable Energy*, vol. 4, no. 6, p. 063 125, Nov. 2012, ISSN: 19417012. DOI: 10.1063/1.4768546. [Online]. Available: http://aip.scitation.org/doi/10.1063/1.4768546.

[59] P. Bendt and A. Rabl, "Optical analysis of point focus parabolic radiation concentrators," *Applied Optics*, vol. 20, no. 4, p. 674, Feb. 1981, ISSN: 0003-6935. DOI: 10.1364/ao.20.000674. [Online]. Available: https://www.osapublishing.org/viewmedia.cfm?uri=ao-20-4-674&seq=0&html=true%20https://www.osapublishing.org/abstract.cfm?uri=ao-20-4-674%20https://www.osapublishing.org/ao/abstract.cfm?uri=ao-20-4-674.